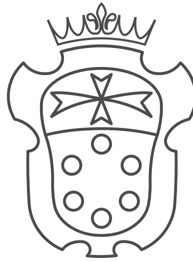

Classe di Scienze

Corso di perfezionamento in Nanoscienze

XXXIV ciclo

Electron and light confinement in laterally structured graphene devices

Settore Scientifico Disciplinare **FIS/03**

Candidato

dr. Nicola Melchioni

Relatore

Prof. Alessandro Tredicucci

Anno accademico 2022-2023

That bench may be iron, but I assure you it's quite comfortable.
There's no better place to collect your thoughts before heading below.

- Elderbug, Hollow Knight

1

- Green D20

Contents

1 Introduction **5**

2 Electron systems for coherent phenomena **11**

2.1 Graphene 11

2.1.1 Crystal lattice and band structure 11

2.1.2 Ambipolar field effect 13

2.1.3 Raman spectroscopy of graphene 16

2.1.4 Plasmon Polaritons in graphene 20

2.2 Coherent phenomena in graphene-light interaction . . . 23

2.2.1 Intersubband transitions 24

2.2.2 Breakdown of the dipole approximation 26

2.2.3 Polaritons: strong light-matter interaction . . . 28

2.3 Coherent phenomena in defected graphene transistors . 30

2.3.1 Defect-induced modifications of graphene properties 30

2.3.2 Deterministic generation of defects 31

2.3.3 Effects on transport of periodic arrays of defects 36

3 Materials and methods **43**

3.1 Device Fabrication 43

3.1.1 Electron beam lithography 43

3.1.2 Exfoliation of graphene 46

3.1.3 Preparation of the substrate 47

3.1.4 Tape technique 47

3.1.5 Chemical vapour deposition 48

3.1.6 Reactive ion etching 50

3.1.7 Raman Spectroscopy 51

3.1.8 Atomic Force Microscopy 53

3.2 Fourier Transform Infrared Spectroscopy 54
3.2.1 Multipass geometry 56
3.2.2 Microscopy techniques 59
3.3 Electrical measurements 62
3.3.1 Wire-bonding the sample 63
3.3.2 Electrical measurements on graphene FETs . . 64

4 Towards Few-Electrons Strong Coupling 69
4.1 Electrodynamic simulations 70
4.1.1 Materials 70
4.1.2 PPs launched by a metallic lattice 73
4.1.3 AGPs below a metallic nanocube 79
4.2 Experimental study of GP structure 81
4.2.1 Multipass measurements: retrieving the ISB transition 83
4.2.2 Fabrication of the metal lattice 85
4.2.3 Reflection measurements 91
4.3 Partial Conclusions 104

5 Coherent properties of a pattern of defects 107
5.1 Engineering a defective pattern 107
5.1.1 Time stability of the defects 108
5.1.2 Patterning regular array of defected lines 121
5.2 Transport across a periodic array of defected lines . . . 129
5.2.1 Dependence on length 133
5.2.2 Dependence on the current bias 135
5.2.3 Dependence on temperature 136
5.2.4 Dependence on pitch 137
5.2.5 Reproducibility 138
5.3 Partial Conclusions 140

6 Conclusions and Perspectives 143

A Fabrication Recipes 149
A.1 General procedures 149
A.2 EBL recipes 151

B Optical grade thin film electrolytes **153**
B.1 Transparency and gating efficiency 153
B.2 Experimental methods 164

Bibliography **166**

Chapter 1

Introduction

Modern electronic technologies often base their working principles on the behaviour of the so-called *electron liquid* [1]. In particular, the behaviour of electrons inside matter is at the basis of many properties of crystals ranging from metals to insulators [2], and even more exotic ones like ferromagnets, superconductors [3] and topological insulators [4].

A particular example of such electron liquid is represented by electrons in graphene [5, 6]. Graphene is a two-dimensional (2D) material in which electrons behave like massless relativistic fermions, showing a linear energy dispersion. Thanks to this, electrons in graphene have been exploited to study intriguing physical phenomena such as Berry phase and anomalous quantum Hall effect [7], fractional quantum Hall effect [8], and many others [6].

The relativistic behaviour of electrons in graphene has a strong impact on its transport properties. Indeed, Klein tunneling has been predicted [9] and observed [10, 11] across potential barriers in a graphene channel. Thanks to the reduced probability of backscattering, electrons in graphene show ballistic behaviour over long distances, up to tens of micrometers [12, 13], even in the presence of long-range disorder in the channel [14]. For these reasons, graphene is an excellent platform to study weak localization and quantum coherent interference of electrons [15].

Among the other applications, graphene can also be exploited to

study light-matter interaction. Indeed, light-matter interaction inside graphene gives rise to quasiparticles called plasmon polaritons (PPs) [16, 17], resulting from the coupling of electromagnetic waves with electronic oscillations inside the crystal. Thanks to the mixed light-matter nature of PPs, such excitations provide a confinement of the radiation in extremely subwavelength volumes. Such confinement of light leads to a huge increase in the electromagnetic field intensity, which can be exploited to study exotic regimes of the light-matter interaction such as ultra-strong coupling [18] and cavity quantum electrodynamics [19].
Another main aspect of light-matter interaction is the quantized behaviour of the electrons in matter [2]. For example, LEDs emit photons with energy corresponding to the gap between the conduction band and the valence band of the chosen semiconductor [20]. For the mid-infrared (MIR) and terahertz (THz) regions of the spectrum, it is possible to exploit the intraband transitions between quantized levels of electrons confined in quantum wells (QWs). QWs are layered crystal heterostructures in which carriers behave like a 2D electron gas (2DEG) with quantized levels in the direction orthogonal to the QW plane [21]. Transitions between such levels are called intersubband (ISB) transitions and are steadily exploited in technologies such as quantum cascade lasers [22, 23] and quantum well infrared photodetectors [24].
In addition to all the remarkable properties of pristine graphene, another unique feature is the possibility to modify its behaviour by engineering structural defects in its lattice [25]. In recent years, a lot of effort has been put in understanding defect formation in graphene with the goal of gaining control of it. Indeed, by artificially engineering defects in graphene, beneficial modifications of its thermal, mechanical, chemical and electronic properties have been achieved [26]. This enabled the design of devices with novel functionalities, with several applications, for example in chemical sensing [27], energy storage [28–30], and thermal photodetection [31]. Moreover, the engineered defects act as barriers reflecting PPs [32], and create local potential barriers for carriers. Such barriers can be employed to explore coherent phenomena, which usually require systems involving a more complex fabrication [33–35].
In such framework, the scope of this PhD thesis is to study the effects

of the confinement of light and electrons on light-matter interaction and the coherent interference of ballistic carriers in laterally structured graphene systems.

In the first part of this work, we exploit the unique properties of the electron liquid in graphene to study light-matter interaction in a mixed graphene/semiconductor QW system with metallic arrays on top. The advantage of mixed graphene/QW systems is twofold: first, the ultra-confinement of light provided by PPs [36] can be exploited to bring the QWs in the semiconductor in interaction with high intensity electromagnetic fields. Therefore, ultra-strong coupling regimes can be reached also with very few electrons involved in the process [37], thus enabling the study of exotic quantum effects such as photon-photon coupling [38] and single-photon nonlinearities [39]. Second, the properties of graphene PPs can be tuned with an external potential [17], thus adding a powerful knob to explore different interaction regimes in one device.

In the second part of this work, we investigate the properties of defects induced in graphene with electron beam irradiation (EBI) at 20 keV. Achieving control over the properties of graphene with a method as simple as a EBI would enable the design of novel devices with applications in both fundamental science and technology. In particular, we focus on the impact of a regular array of defected lines on the transport properties of a graphene channel. Such system is ideal to study the coherent interference of electrons in graphene, thanks to the long-range order induced by the regular array. Moreover, the demonstration that coherent effects are retained in defect-engineered systems unlocks the possibility to exploit the proposed method to design custom geometries with unprecedented spatial resolution. Such systems are fundamental to study collective effects in the electron liquid, thanks to the wave nature of the relativistic electrons inside graphene.

The thesis is organized as follows. In the second Chapter, we outline the background in which we set our work. We first introduce the band structure of graphene, and derive the basic properties of its electron liquid. We then introduce the Raman spectroscopy of graphene and the contribution of phonons for the study of the crystal properties. In addition, we introduce PPs and summarize their properties. Afterwards,

we describe the energy spectrum of subbands in III-V semiconductor heterostructures and the absorption rates of the electronic transitions between such subbands. After introducing the so-called *dipole approximation*, we show how the coupling of ISB transitions with PPs in graphene would lead to the breakdown of such approximation, with impact on the transition frequency and selection rules. We then explain how the strong coupling between light and matter leads to polaritons, which are excitations of mixed light-matter nature. In the last section of the chapter, we explore the role of defects in coherent electron transport in graphene. We give a brief overview of the defect engineering and how the defects modify the properties of graphene. Then, we introduce the different methods for introducing defects in the lattice, with a particular focus on electron beam irradiation. We then describe the effect on the transport properties of periodic arrays of defects modeled as potential barriers.
We continue by discussing the methods we employed in our experiments in Chapter 3. We start from the fabrication of the samples: we introduce electron beam lithography process and the thermal deposition of metals. Then, we describe the exfoliation process we used to isolate monolayer graphene flakes. We then briefly show the seeded chemical vapour deposition method, which yields the large-area monocrystalline graphene flakes we used in the optical experiments. Afterwards, we describe the Raman spectroscopy methods we used to study the doping, strain and defect density inside our graphene crystals. We then introduce the atomic force microscopy method, used to study the defected features induced by us in graphene. We discuss in detail the Fourier Transform Infrared spectroscopy methods we used to optically measure our samples, explaining the multipass method used for measuring the ISB transitions in the QWs and the microscopy technique exploited in our experiments. At the end of the chapter, we introduce the electrical measurements we performed on our graphene devices. We show the setups used in the experiments and explain the different methods.
In Chapter 4, we discuss our study of light-matter interaction in a graphene/semiconductor heterostructure. First, we introduce our simulative campaign on two different geometries we designed for coupling

graphene PPs to ISB transitions in a single shallow quantum well. Then we study the fabrication and experimental measurement of one of the two simulated structures.

We then move to the experimental realization and measurement of a graphene channel with regular defective patterns in Chapter 5. We first study the time stability of the defects induced by EBI with the methods explained in Chapter 2. Then, we investigate the achievable spatial resolution of regular arrays of defected lines patterned with EBI. We then show the transport measurements across such defected patterns and demonstrate the effects of coherent interference of electrons in our systems. We study the system by varying temperature, current bias, number of periods, and pitch of the patterned array.

In the last Chapter, we conclude by summarizing all the results of the presented work and by giving a brief outlook on further experiments on the same systems.

Chapter 2

Electron systems for coherent phenomena

2.1 Graphene

2.1.1 Crystal lattice and band structure

Graphene is a two-dimensional crystal in which carbon atoms are arranged in a honeycomb lattice formed by two triangular lattices [5], as shown in Fig. 2.1a. The atomic orbitals have sp_2 hybridization and each atom is bound to its three neighbours by σ bonds that form a strong planar structure. The remaining electron occupies a p_z orbital oriented in the out-of-plane direction. Such orbitals hybridize with the surrounding atoms to form a band of electrons delocalised over the whole crystal. The band structure of graphene was first theoretically studied by P.R. Wallace in 1947 [40]. Wallace wrote and solved the analytical form of the Hamiltonian by using the tight binding method and considering the first and second nearest neighbors. The resulting band structure, visible in Fig. 2.1b, features a valence and a conduction band that touch at six points in the momentum space. These points can be divided into two sets of three points, labelled K and K', and called Dirac points. The energy dispersion around each of the Dirac

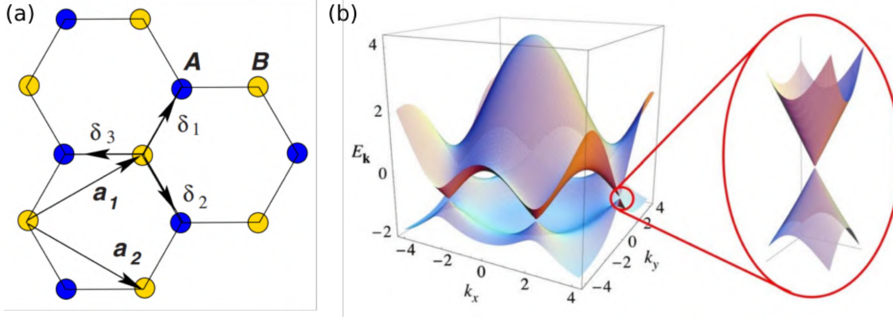

Figure 2.1 – (a) Real space schematics of the graphene honeycomb lattice. It is made up of two triangular lattices (A and B). δ_1, δ_2, δ_3 are the in-plane σ bonds and are 1.42 Å. a_1 and a_2 are the lattice unit vectors. (b) Band structure of graphene computed using the solution by Wallace. The valence and conduction bands touch at six points located at the edge of the Brillouin zone. In the inset, detail of one of the Dirac cones. The touching point is called Dirac point. Image taken from [5].

points can be approximated as

$$E_{\pm}(\mathbf{q}) = \pm \hbar v_F |\mathbf{q}|, \tag{2.1}$$

where $E_{\pm}$ is the energy above and below the Dirac point, $\hbar$ is the reduced Planck constant, $\mathbf{q}$ is the momentum computed from the K point ($\mathbf{k} = \mathbf{K} + \mathbf{q}$) and $v_F \sim 10^6$ m/s is the Fermi velocity of electrons in graphene. Eq. 2.1 shows that the energy dispersion is linear around the Dirac point ($\mathbf{q} = 0$), thus forming the Dirac cone shown in the inset of Fig. 2.1b. From this equation, it is possible to compute the density of states (DoS) around the Dirac points:

$$DoS(E) = \frac{2|E|}{\pi \hbar^2 v_F^2} \tag{2.2}$$

where E is the energy evaluated from the Dirac point energy. The density of states is vanishing for $E = 0$ and grows linearly with E. The Fermi energy for undoped graphene lies at the Dirac points, which are thus also called charge neutrality points. As a consequence, graphene has a gapless band structure with a vanishing DoS at the touching points, thus it is defined as a semimetal. By using Eq. 2.2, it is possible

to link the Fermi energy inside graphene to a finite charge carrier density n:

$$n = \int f(E)DoS(E)dE = \frac{E_F^2}{\pi\hbar^2 v_F^2} \quad \rightarrow \quad E_F = \hbar v_F \sqrt{\pi|n|} \tag{2.3}$$

where $f(E)$ is the Fermi-Dirac distribution evaluated at $T = 0$ K. Further information about the electronic properties of graphene can be found in [41].

2.1.2 Ambipolar field effect

As described in Sec. 2.1.1, graphene is a 2D material with a linear dispersion relation around the Dirac points. Therefore, the delocalised electrons inside the crystal can be modeled as a 2D gas of relativistic fermions. One of the unique properties of graphene stems from this aspect: the ambipolar field effect [42, 43]. The ambipolar field effect means that by applying an external potential between graphene and a metallic electrode, separated by a dielectric, it is possible to change the charge carrier density n in the crystal (field effect) and also its sign (ambipolar). The external potential is usually called gate potential, in analogy with the field effect transistor (FET) terminology. Since the conductivity of graphene depends on the number of free charge carriers in the conduction or valence bands [6], the resistivity ρ of graphene can then be tuned by the applied gate voltage V_G, as shown in Fig. 2.2. Indeed, by considering a graphene sheet with length L and width w contacted by a metallic electrode, it is possible to model the impact of the ambipolar field effect on the resistance R_{SD} as

$$R_{SD}(V_G) = R_C + \frac{L}{w\mu e}\frac{1}{\sqrt{n_0^2 + (C_G(V_G - V_D))^2}} \tag{2.4}$$

where R_C is the resistance of the metal-graphene interfaces, called contact resistance, μ is the mobility of electrons in the crystal, n_0 is the residual charge density, C_G is the capacity of the exploited gate, V_G is the gate voltage and V_D is the voltage at which the Fermi energy lies at the Dirac point. More complete models can be considered to take into

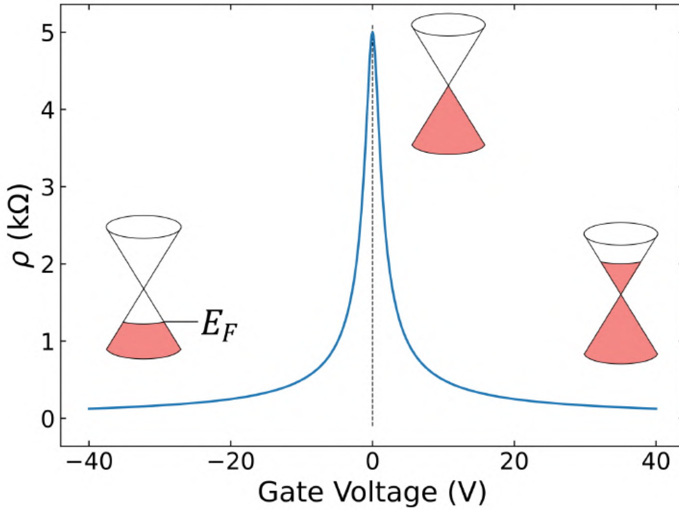

Figure 2.2 – The resistivity of graphene can be changed with an external voltage, called gate voltage. For $V_G < 0$ ($V_G > 0$), the Fermi energy lies below (above) the charge neutrality point. For $V_G = 0$ the Fermi energy lies at the charge neutrality point, thus resulting in an increased resistivity.

account detailed aspects, such as mobility asymmetry between holes and electrons, charge inhomogeneity in the channel and the effects of a non-uniform electrostatic potential [44–46].

Different gating geometries have been exploited to tune the carrier density in graphene. We will focus on three examples: back-gate (Fig. 2.3a), top gate (Fig. 2.3b) and ionic liquid gate (Fig. 2.3c). The first and simplest is the back-gate geometry [47], shown in Fig. 2.3a: a conductive substrate serves as metallic electrode (gate) and is separated from the graphene channel by a dielectric slab of thickness t. The most common example is a highly doped silicon (Si) substrate covered by $t \sim 300$ nm of thermally grown silicon oxide (SiO_2). By using a parallel plate capacitor model, the carrier density induced by this geometry inside graphene is:

$$n_G = \frac{\varepsilon_0 \varepsilon_r}{te} V_G \tag{2.5}$$

where ε_0 is the permittivity of vacuum, ε_r is the permittivity of the dielectric, e is the electron charge. Such change in charge carrier density

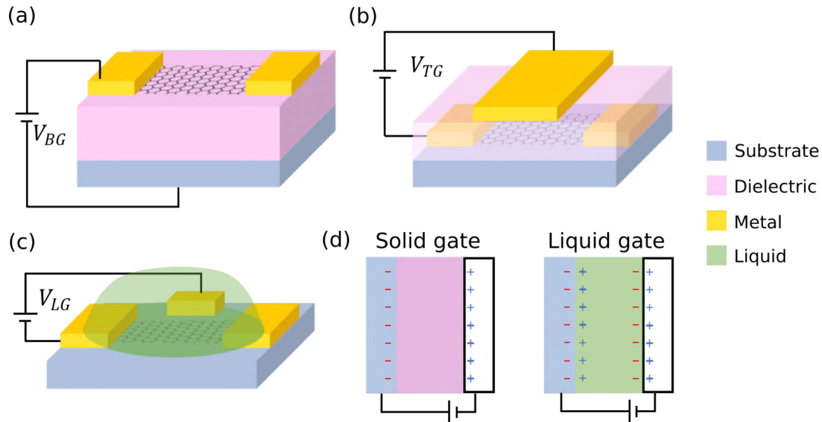

Figure 2.3 – Schematics for a graphene FET with different gating geometries. (a) Back gate geometry: the external voltage V_{BG} is applied between a conductive substrate (blue, bottom layer) and the graphene sheet. The two planes are divided by a dielectric slab (pink). (b) Top gate geometry: the external voltage V_{TG} is applied between graphene and an electrode fabricated on top of a dielectric slab above graphene. (c) Ionic liquid gate geometry: the external voltage V_{LG} is applied between graphene and an electrode immersed in a drop of ionic liquid. (d) Comparison between the electrostatic behaviour of solid gates (left) and ionic liquid gates (right). Solid gates can be modeled as parallel plate capacitors, while liquid gates have ions that rearrange forming EDLs.

is called electrostatic doping [43]. In this geometry, the capacitance $C_G = \varepsilon_0\varepsilon_r/te$ is the oxide capacitance and the induced charge density can reach values as high as 10^{13} cm^{-2}. A second geometry is the top-gate geometry (see Fig. 2.3b) [48], where graphene is covered by a dielectric slab and a metallic electrode is deposited on top of the stack. The thickness of the dielectric depends on the material used (e.g., tens of nanometres for oxides grown by atomic layer deposition, or even few nanometers for 2D insulators such as hexagonal boron nitride [49]), but is in general lower than in the back-gate geometry, and therefore C_G is usually higher. Top gates can be used in combination with back-gates in a geometry called dual-gating to induce controlled non-uniformity in the carrier density of graphene [50, 51].
A different approach with respect to electrostatic doping is offered by

electrochemical doping (see Fig. 2.3c). The change in the carrier density is induced by polarizing a liquid with free ions, called ionic liquid (IL). In the previous examples of solid gating, the applied potential is screened by charges reorienting in the material, as in the dielectric of a parallel plate capacitor (see the left part of Fig. 2.3d). Contrarily, when a potential is applied between the channel and the gate electrode immersed in the ionic liquid, the ions migrate inside the IL and arrange as charged layers at the interfaces with metals. The electrostatic potential created by these ionic layers is screened by attracting charge carriers inside the graphene channel and the electrode, thus forming the so-called electric double layers (EDL) [52] as shown in the right side of Fig. 2.3d. These EDLs can be modeled as parallel plane capacitors with inter-plane distance of a few nanometers, thus offering an enhanced gating efficiency due to their extremely high capacitance [53–55].

2.1.3 Raman spectroscopy of graphene

The crystal lattice of graphene is a combination of two triangular lattices, as discussed in Sec. 2.1.1. Such crystal lattice can be altered by strain or other kind of defects and irregularities, especially in real-world devices. So far, we studied the electronic band structure and the properties of the two-dimensional electron gas arising in this system. However, the oscillations of the atoms in the lattice (i.e., phonons) are related to the spring constant of the chemical bonds between the atoms. These bonds are influenced by the irregularities in the crystal. Phonons can therefore be studied to gain information about the crystal structure. To this end, Raman spectroscopy has proved to be a versatile tool for studying the doping, strain and defect density in graphene [56–58]. Indeed, the Raman peaks of graphene originate from the interaction of light with the in-plane transverse and longitudinal optical phonons in the crystal (iTO and iLO respectively). The impinging light is absorbed and creates a virtual electron-hole (e-h) pair. The e-h pair is scattered by phonons into a lower state and recombines via different mechanisms, emitting a photon with red shifted energy. The Raman spectrum is therefore sensitive to changes in lattice spring constant and electron-phonon (e-ph) coupling. Such parameters are strongly influenced by

doping [59], strain [60], and defective sites in the crystal [61]. These properties can thus be studied by Raman spectroscopy.

A typical spectrum of defect-free monolayer graphene collected under a 514 nm laser illumination is shown in Fig. 2.4a. Two main peaks are visible: the G peak at ~ 1580 cm^{-1} and the $2D$ peak at ~ 2700 cm^{-1}. The shape of these peaks changes when varying the number of layers of the inspected crystal. In monolayer graphene, both G and $2D$ peaks are Lorentzian. When increasing the thickness, the amplitude of the G peak gradually increases (see the upper spectrum in Fig. 2.4a) and the shape of the $2D$ peak changes from Lorentzian to a combination of more Lorentzians, as shown in Fig. 2.4b [57].

The G peak arises from the intravalley scattering of the created e-h pair with a stretching mode of the C-C in-plane σ bonds (both low-energy iTO and iLO, see Fig. 2.5a). Since the change in doping changes the lattice constant of the crystal [59], the frequency of the G peak increases when the doping inside graphene increases. Moreover, when the Fermi energy is moved from the charge neutrality point, e-h creation is increasingly inhibited by the Pauli principle [41]. Due to the lower number of decaying paths for e-h pairs, the full width at half maximum (FWHM) narrows. Moreover, the reduction of the impact of the Kohn anomaly [62], the intensity (I) of the G peak increases when increasing

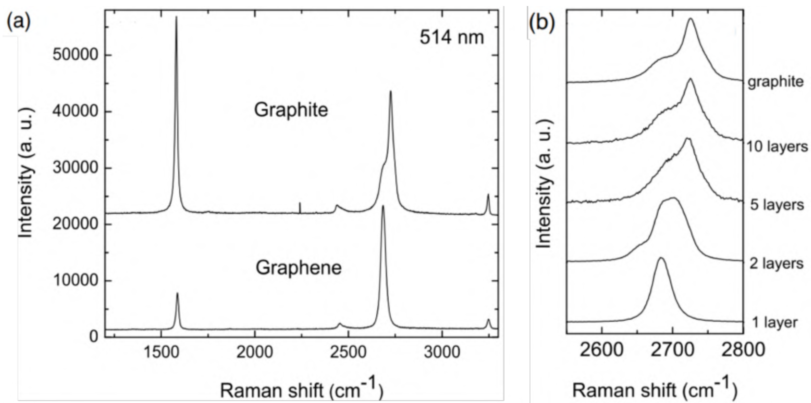

Figure 2.4 – (a) Raman spectrum of graphene (below) and graphite (above) for 514 nm illumination. (b) Evolution of the shape of the $2D$ peak with the number of layers of the crystal. Adapted from [56]

the doping of graphene. Contrarily, defects in the lattice decreases $I(G)$ as the e-ph coupling is less efficient.
The $2D$ peak is a second order Raman scattering originating from the scattering with in-plane breathing-like modes of the carbon rings (iTO, see Fig. 2.5). Its frequency increases (decreases) when the holes (electron) concentration increases [60]. The FWHM($2D$) increases with doping, strain, and in the presence of defects in the crystal, due to scattering of e-h pairs with the defected sites [63]. On the other hand, the intensity $I(2D)$ decreases when the Fermi energy is raised, since the number of possible decaying path is related to e-e coupling. Additionally, since the $2D$ peak originates from the scattering of e-h pairs between neighboring Dirac cones, the $2D$ peak is particularly sensitive to changes in the band structure induced by strain [64].
Defects in the lattice cause the presence of two additional peaks: D and D', as shown in Fig. 2.6. The D peak is visible at ~ 1340 cm^{-1} and is formed by electrons which are inelastically scattered from K to K' point by a phonon and elastically scattered back to K point by defects

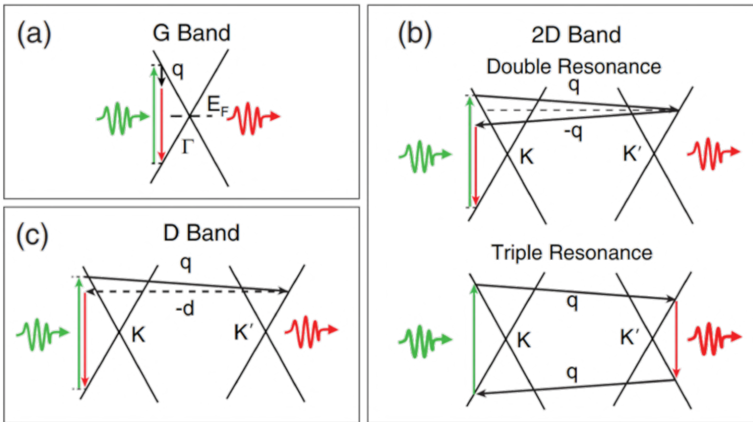

Figure 2.5 – Schematics of the scattering processes which generate the peaks in the Raman spectrum of graphene. (a) The G band arises from the intravalley scattering with low-energy iTO and iLO phonons. (b) The $2D$ band arises from two different second order processes: double resonance (top) and triple resonance (bottom). (c) The D band arises from the elastic scattering of the electrons in the virtual state with a defect (horizontal line). Taken from [59].

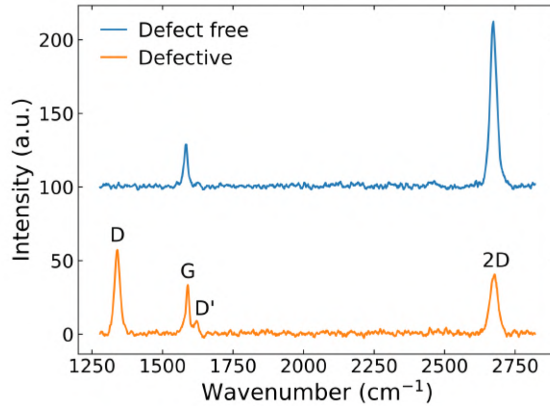

Figure 2.6 – Comparison of the typical Raman spectra for defect-free monolayer graphene (top, blue line) and the Raman spectra of defected graphene (bottom, orange line).

(see Fig. 2.5c). The D' peak is close to the G peak at ~ 1600 cm^{-1} and originates from the intravalley equivalent of the D peak formation process.

Graphene crystals have been classified into three stages based on the degree of disorder in the lattice [57]. The so-called *Stage 1* graphene goes from crystalline to nanocrystalline: defects are present but the overall crystal structure is retained. *Stage 2* graphene includes sites with low sp^3 amorphous carbon concentration, while *Stage 3* goes from low sp^3 concentration to high sp^3 concentration. When graphene is in Stage 1, it is possible to correlate the intensity $I(D)$ of the D peak, normalized with the intensity $I(G)$ of the G peak, to the density of defects in the lattice by the Tuinstra-Koenig relation [65] for graphene [61]:

$$n_D[\mathrm{cm}^{-2}] = 7.3 \times 10^9 E_L^4[\mathrm{eV}^4]\frac{I(D)}{I(G)} \tag{2.6}$$

where E_L is the Raman laser excitation energy. Moreover, the D peak originates from interaction with short-range defects, which provide large momenta to electrons scattered between valleys. Conversely, the D' peak stems from intravalley scattering, which is mediated by long-range defects which carry lower momenta [66]. Thus, while $I(D)/I(G)$ is independent on the nature of the defects [67], the ratio of the intensities

of the D and D' peaks gives information on the statistical composition of the defect population [68].

2.1.4 Plasmon Polaritons in graphene

Surface plasmons (SPs) are electromagnetic waves propagating along the boundaries between a metal and a dielectric due to the interaction of light with the free charge carriers in the conductor [69]. SPs are transverse magnetic (TM) modes that exhibit an out-of-plane component of the electric field exponentially decaying with the distance from the plane of interaction. These modes concentrate the light in subwavelength volumes, thus leading to strong enhancement of the electromagnetic fields [70]. A more complete study of SPs at metal-dielectric interfaces can be found in [69].
Graphene can sustain two-dimensional TM modes called plasmon polaritons (PPs) [17]. Considering a graphene sheet surrounded by dielectrics of permittivity ε_1 and ε_2, the computed dispersion of graphene plasmon polaritons is [71]:

$$q_{pl} \approx \varepsilon_0 \frac{\varepsilon_1 + \varepsilon_2}{2} \frac{2i\omega}{\sigma(q_{pl}, \omega)} \tag{2.7}$$

where $\hbar q_{pl}$ is the momentum of PPs, ω is the radiation frequency and $\sigma(q_{pl}, \omega)$ is the in-plane conductivity of graphene. This formula is valid if $q_{pl} \gg \omega/c$, which is fulfilled for infrared frequencies. It is possible to evaluate the dispersion relation, including different effects such as non-locality, by substituting in Eq. 2.7 the conductivity $\sigma(q_{pl}, \omega)$ computed with the desired accuracy [16, 72]. A comparison of three different models is visible in Fig. 2.7a: the first (blue dashed line) takes into account only intraband conductivity, the second (red dash-dotted line) considers the impact of interband excitations on the conductivity and the third, more complete one uses the conductivity computed with non-local random phase approximation [72]. We will consider a local, Drude-like model for graphene conductivity. This approximation, valid for $\hbar\omega < E_F$, yields the dispersion relation [16]

$$q_{pl} = \frac{2\pi}{\lambda_{pl}} = \frac{\hbar^2}{4e^2 E_F}(\varepsilon_1 + \varepsilon_2)\omega(\omega + \frac{i}{\tau}) \tag{2.8}$$

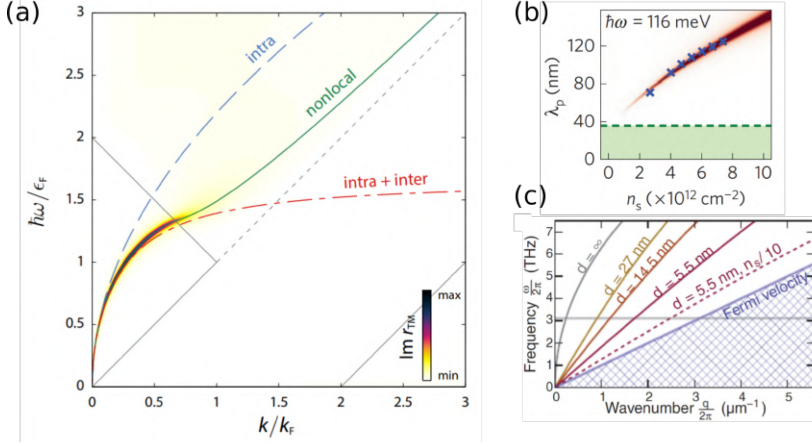

Figure 2.7 – (a) Dispersion relation for graphene PPs calculated taking into account different effects: only intraband conductivity (blue dashed line), intraband and interband transitions (red dash-dotted line) and using non local random phase approximation (green solid line). Taken from [72]. (b) The wavelength of PPs can be tuned by changing the carrier concentration in the crystal n_s. The red area is the dispersion relation simulated with the transfer matrix method, while the blue crosses are experimental points for an excitation energy of $\hbar\omega = 116$ meV. Taken from [73]. (c) Dispersion relation of plasmons in graphene placed at a distance d from a metal plate. When reducing the distance, the dispersion relation flattens towards the Fermi velocity line. Taken from [74]

where λ_{pl} is the plasmon wavelength and τ is the electron scattering time in graphene.

Plasmon polaritons confine light to volumes $\sim 10^6$ times smaller than the diffraction limit. The confinement can be evaluated by the parameter $\eta_0 = \frac{\lambda_0}{\lambda_{pl}} \sim \frac{1}{4\alpha}(\frac{\hbar\omega}{E_F})$, where λ_0 is the free space wavelength and $\alpha = e^2/\hbar c$ is the fine structure constant. Moreover, as visible from Eq. 2.8, the wavelength of plasmons in graphene can be tuned by changing the Fermi energy of the graphene sheet (see Sec. 2.1.2). The effect of the doping is shown in Fig. 2.7b, where the PPs wavelength is measured for an impinging light of energy $\hbar\omega = 116$ meV as a function of the carrier concentration in graphene. Furthermore, when graphene is placed at a distance d from a metallic plate, the dispersion relation of plasmons modifies. As shown in Fig. 2.7c, the dispersion relation approaches the Fermi velocity line in graphene as d is decreased [74].

These modified modes, called acoustic graphene plasmons (AGPs), offer an increased confinement of light and have been used to demonstrate an unprecedented confinement factor $\eta_0 \sim 5 \times 10^{10}$ [36].
Thanks to these properties, graphene PPs are an excellent platform for plasmonics [73, 75], offering both strong field confinement and low damping that approaches fundamental limits at low temperature [76]. However, since PPs carry large momentum (see Eq. 2.8), their dispersion relation always lies below the light line. Thus, far field light cannot excite plasmons in graphene without a specific coupling geometry that can fill the momentum mismatch between the two modes [77]. We will now give two examples of such geometries.
The first and most popular method is to exploit the coherence of a periodic grating, as shown in Fig. 2.8a [78–81]. When a beam of light hits a grating structure of pitch p, it reflects in a series of diffraction orders which carry extra momentum, in multiples of the quantity $\kappa = 2\pi/p$. From a lattice point of view, the periodicity of the grating folds the plasmonic dispersion relation into a first Brillouin zone of width κ, as shown in the bottom part of Fig. 2.8a. Such geometry allows far field light to couple with PPs with the following matching conditions:

$$q_{pl} = k\sin(\theta) \pm n\kappa \tag{2.9}$$

where $k = \sqrt{\varepsilon}\omega/c$ is the wavevector of the incoming light, θ is the angle of incidence and n is the (integer) diffraction order. With this method is therefore possible to excite plasmonic modes of fixed momentum. The grating structure can be a dielectric substrate, a metallic lattice or even a periodic set of graphene nanoribbons [17].
A second method for plasmon excitation is to exploit near-field optical microscopy. In this geometry, the momentum is provided by the near-field component of the light scattered by a sharp metallic tip, such as the tip of a scanning near-field optical microscopy (SNOM) setup, as shown in Fig. 2.8b [82]. The incoming light is scattered from a tip of radius a_0 into a near-field with a momentum distribution $\rho(k)$ peaked around $\xi_0 = \pi/a_0$ and can thus fill the momentum gap. In contrast with the previous method, the excitation of PPs happens locally below the tip. Therefore, this method allows to study the properties of PPs with

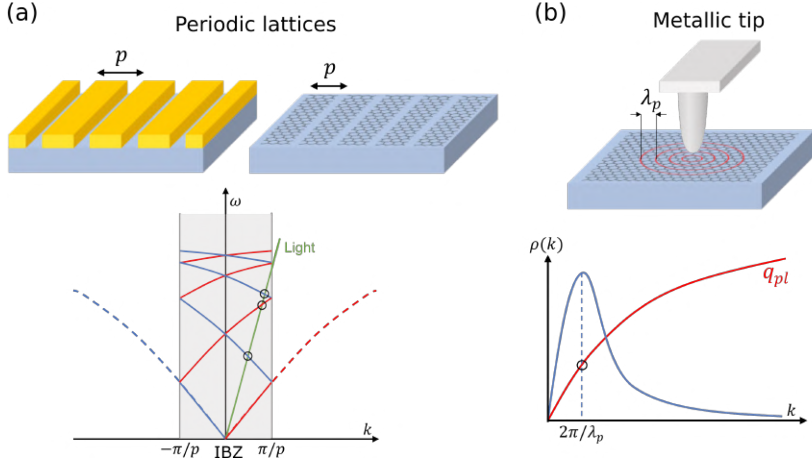

Figure 2.8 – Examples of geometries for launching plasmons in graphene. (a) Periodic lattices give a momentum to the impinging light proportional to the pitch p. The dispersion relation of plasmons is folded into the first Brillouin zone, thus creating energy-momentum matching conditions for light to excite PPs. (b) A metallic tip scatters the light, creating a near field with a given momenta distribution $\rho(k)$. The near field can excite plasmons with a wavelength λ_p proportional to the maximum of the momentum distribution.

nanometric resolution [73, 76, 83]. Even if the two examined geometries are the most exploited, different methods have been developed for launching plasmons in graphene. A more complete study on how to excite PPs can be found in [17].

2.2 Coherent phenomena in graphene-light interaction

Thanks to the peculiar optical properties, graphene has been widely considered to study the interaction between light and matter in various systems. We will now introduce the basic concepts of electronic excitation in matter.

2.2.1 Intersubband transitions

Electrons inside a crystal have limited sets of allowed energies, called bands, divided by gaps [2]. By engineering the band structure of solids [84], it is possible to confine electrons in an artificial quantum well (QW), thus creating a quasi-2D electron gas [21, 85]. The confinement in one direction leads to a further quantization of the electronic states. These quantized levels are called subbands, as they can be interpreted as a splitting of a single band (see Fig. 2.9a). Transitions between different subbands are called intersubband (ISB) transitions. The energy of each subband can be written as:

$$E_n(k) = E_n + \frac{\hbar^2 k^2}{2m^*} \tag{2.10}$$

where E_n are the quantized energy levels that depend on the shape of the well and can be computed with Schroedinger equation [21] and the second right hand term is the parabolic dispersion of the quasi-2D electron gas, as shown in Fig. 2.9b [3]. In this equation, n is the subband index, k is the in-plane momentum of the electron

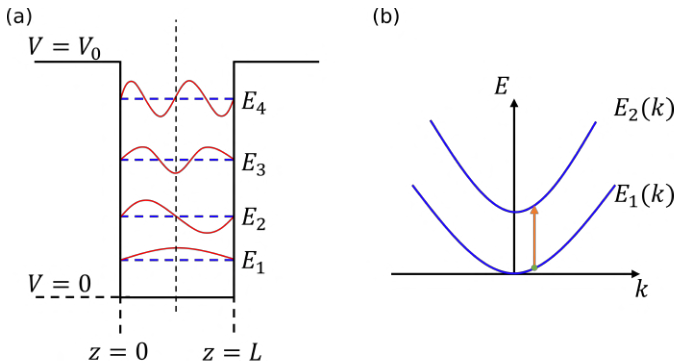

Figure 2.9 – (a) Band structure of a quantum well in the conduction band of a semiconductor heterostructure. The depth of the well is V_0 and the width is L. Four quantized energy levels E_n are visible (blue dashed horizontal lines). The wavefunctions of the states (red solid lines) have alternating parity, starting form the symmetric ground state. (b) Energy dispersion for the first two subbands, according to Eq. 2.10. The orange arrow indicates the ISB transition of an electron (green dot) from the first subband to the second subband.

and m^* is the (n-dependent) in-plane effective mass of the electron [22]. The wavefunctions of the electronic states can be written as the product between the Bloch function of the chosen band $u_\nu(\mathbf{r})$ and a slowly varying envelope function $\phi_n(\mathbf{r})$ that depends on the shape of the potential well [21]. In the simplest approximation, the envelope function is a scalar (one-band model [22]). In a complete description, it has the form of a vector with one component for each band considered for the computation [22].
To evaluate the absorption or emission rate of ISB transitions, it is possible to use Fermi's golden rule for the transition rate from an initial state i to a final state f [21]:

$$W_{if} = \frac{2\pi}{\hbar} |\langle\psi_f| H_{int} |\psi_i\rangle|^2 \delta(E_f - E_i - \hbar\omega) \tag{2.11}$$

where $\psi_i = \phi_n u_\nu$ and $\psi_f = \phi_{n'} u_{\nu'}$ are the wavefunctions of the initial and final state respectively, the δ function ensures the energy conservation during the process and H_{int} is the Hamiltonian of the interaction of the electrons with the incoming photons. Considering the electric field of a plane wave (such as the field of a free-air photon), the matrix element can be written:

$$\langle\psi_f| H_{int} |\psi_i\rangle \propto \langle\psi_f| e^{i\mathbf{q}\cdot\mathbf{r}} \mathbf{e} \cdot \mathbf{p} |\psi_i\rangle \tag{2.12}$$

where $\mathbf{q}$ and $\mathbf{e}$ are the wavevector and the polarization vector of the incoming field respectively and $\mathbf{p}$ is the momentum operator of the electron. A selection rule arises from Eq. 2.12: since ISB transitions are out-of-plane electronic excitations, they can only couple with electric fields with a component in the out-of-plane direction. Such selection rule limits the experimental setups for observing ISB transitions [21, 22]. If the wavelength of the impinging light is larger than the characteristic length of the system (i.e. the length L of the well for the case of a QW), then $\mathbf{q} \cdot \mathbf{r} \ll 1$ and it is possible to ignore the oscillating term $e^{i\mathbf{q}\cdot\mathbf{r}}$. By applying this so-called dipole approximation, the transition rate depends on the dipole matrix element between the initial and final states. It is useful to define a dimensionless parameter, called oscillator strength $f_{n,n'}$, that is proportional to the matrix element of

the transition between n and n' states:

$$f_{n,n'} = \frac{2}{m^*\hbar\omega_{n,n'}} |\langle n| p_z |n'\rangle|^2 = \frac{2m^*\omega_{n,n'}}{\hbar} |\langle n| z |n'\rangle|^2 \tag{2.13}$$

where p_z is the out-of-plane component of the momentum operator and $\omega_{n,n'} = (E_{n'} - E_n)/\hbar$ is the frequency of the transition. The last equivalence is granted by considering that the matrix elements of $\mathbf{r}$ are related to $\mathbf{p}$ by the formula $p_{n,n'} = im^*\omega_{n,n'}r_{n,n'}$. The oscillator strength is useful to compare the transition strengths in different optical systems [86].

2.2.2 Breakdown of the dipole approximation

So far, we dealt with ISB transitions excited with far-field photons. Such photons carry very little momentum, thus inducing vertical transitions (see Fig. 2.9b), for which it is possible to apply the dipole approximation. We now consider a system where a quantum well of thickness d is separated from a graphene sheet by a dielectric spacer of thickness l_s [87], as shown in Fig. 2.10a. As in the previous case, we use the Fermi golden rule to study the absorption and emission rates of ISB transitions in proximity of graphene plasmons. However, the dipole approximation does not hold in the case of PPs. Indeed, PPs carry much more momentum than a photon at the same energy (see Sec. 2.1.4), which means that $\lambda_{pl} = 2\pi/q_{pl}$ is not much larger than the characteristic lengths of the systems. Considering the electric field of PPs [17], the matrix element of the interaction Hamiltoninan for the presented system can be written as:

$$\langle\psi_i| H_{int} |\psi_f\rangle \propto \langle n| e^{-qz}\partial_z |n'\rangle \cdot \langle\mathbf{k}| e^{\pm i\mathbf{q}\cdot\rho} |\mathbf{k}'\rangle \tag{2.14}$$

where $\mathbf{q}$ is the momentum of the polariton, k is the wavevector of the in-plane electronic state and ρ is the in-plane position vector. The first term in the right hand side gives the interaction amplitude in the out-of-plane direction due to the overlap between the PP electric field and the electronic states inside the QW. The derivative comes from the momentum operator. The second term is the in-plane momentum

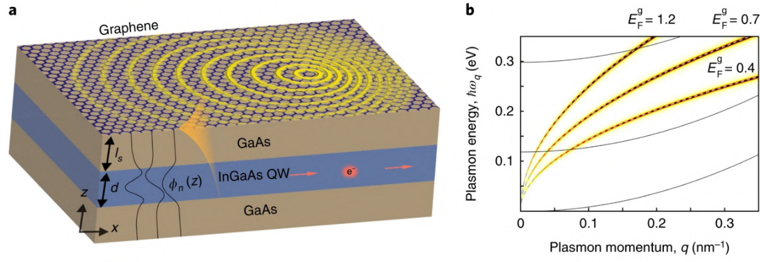

Figure 2.10 – (a) Geometry considered for studying the emission/absorption rates of ISB transitions in contact with graphene PPs. The yellow fringes are excited plasmons, whose electric field distribution is shown shaded in orange. Some of the out-of-plane profiles of the wavefunctions of the electrons $\phi_n(z)$ are shown as solid lines. (b) Dispersion relations for electrons in the QW (solid black lines) overlapped with the dispersion relations for PPs at different Fermi energies (red dashed lines). The yellow shading is the broadening due to plasmonic losses. Image taken from [87]

conservation. Since plane waves are translation operators for momentum, the second term can be rewritten as $\delta(\mathbf{k}' - \mathbf{k} \mp \mathbf{q})$, depending if the plasmon is emitted or absorbed. The delta function can be substituted by a Lorentzian to take into account plasmonic losses. The allowed frequencies for absorption or emission of PPs can be determined by substituting the dispersion relations of the electrons and the plasmons in the energy and momentum conservation laws stemming from Eq. 2.14 and the Fermi golden rule (see Fig. 2.10b). Moreover, thanks to the possibility to change the dispersion relation of plasmons with the Fermi energy inside graphene, it is possible to change the energy and momentum conservation conditions. Therefore, the emission and absorption energies of the quantum well can be tuned [87]. Moreover, due to the momentum dependence, some differences arise with respect to the dipole approximation. First, the energy transitions for absorption and emission are not equivalent: the absorption energy is blue-shifted while the emission is red-shifted with respect to the vertical transitions. This effect is stronger as the Fermi energy is lowered, because of the increased momentum of the PP at the same energy. In addition, since the matrix element does not have a specific parity as in the case of the dipole [21], the selection rule forbidding transitions between ISBs n of

the same parity is lifted. For example, transition $3 \leftarrow 1$ is allowed if mediated by PPs.
This description holds in the case of weak coupling between graphene plasmons and ISB transitions. In the following section, we introduce strong coupling between light and matter.

2.2.3 Polaritons: strong light-matter interaction

Strong light-matter interaction results from the superposition of a photonic and a matter excitation at frequency ω_0. The interaction lifts the energy degeneracy with an anticrossing behaviour, splitting the uncoupled modes into new hybrid light-matter quasiparticles, called polaritons [88], as shown in Fig 2.11. The mode separation is called Rabi frequency Ω_R, which is the frequency of the energy exchange between the modes.
Strong coupling has been first observed with atoms in a cavity [89]. More recently, strong coupling was demonstrated between intersubband transitions in a multiple quantum well structure embedded in a photonic microcavity [90]. In such systems, the interaction between light and

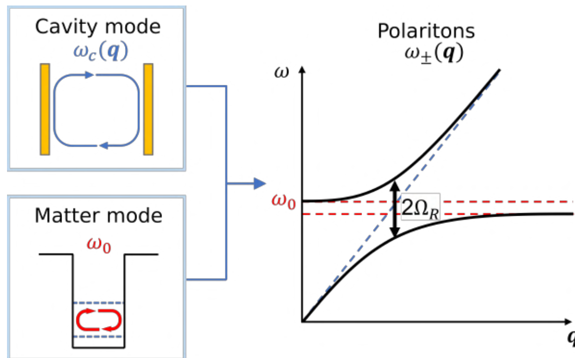

Figure 2.11 – Strong coupling happens when a matter mode at frequency ω_0 is spacially overlapped with a cavity mode with a given dispersion relation $\omega(\mathbf{q})$. The uncoupled modes show a crossing point, when the cavity mode (blue dashed line) is resonant with the matter mode (upper red dashed line). If they are overlapped, strong coupling arises, creating new modes $\omega_\pm(\mathbf{q})$ that show anticrossing behaviour around the resonant condition

matter can be described with the Hopfield model [91]. In this model, both electromagnetic field and material excitations are considered as boson fields with harmonic excitation spectra [92]. This is possible because the number of involved electrons is so high that electronic excitations can be described as collective material polarization. By solving the coupled light-matter Hamiltonian, it is shown that the new polaritonic states are linear mixing of the two excitations, with a maximum mixing corresponding to the point of minimal splitting [93]. In this description, the minimum mode separation can be written as [94]:

$$2\Omega_R = \sqrt{\frac{f_\alpha^0 f_\alpha^w e^2 (\Delta N_\alpha / S)}{\varepsilon \varepsilon_0 m^* L_{eff}^\alpha}} \tag{2.15}$$

where f_α^0 is the oscillator strength of the intersubband transition $\alpha \equiv [n, n']$, f_α^w is the modal overlap factor between the intersubband transition and the cavity field, ΔN_α is the difference in population between the initial and final subbands, S is the area of the system and L_{eff}^α is the effective length of the transition states [95]. The Rabi frequency quantifies the strength of the light matter interaction through the coupling constant $g = \Omega_R/\omega_0$. It is therefore possible to change the strength of the interaction by tuning the different factors in Eq. 2.12. In particular, the interaction is stronger for large numbers of electrons involved in the transition and for cavity fields that are confined and spatially overlap with the ISB transition. In the first experiments in solid state systems, the Rabi frequency reached a small fraction of ω_0 [90]. In the last decades, different systems were studied to maximize g, even reaching ultra strong coupling regimes where Ω_R is a significant fraction of the transition energy [18, 96, 97]. When the number of electrons is reduced towards unity, thus reaching the few-electron regime, the system cannot be described by collective excitations as in the Hopfield model, but rather as a collection of two-level systems coupled through interparticle interactions (Jaynes-Cummings model, [37, 98]). In this regime, strong quantum nonlinear effects take place, such as single-photon nonlinearities [39] and photon-photon interactions [38].

2.3 Coherent phenomena in defected graphene transistors

In Sec. 2.1, we introduced a few of the outstanding mechanical, physical, and chemical properties of graphene in its pristine form. The presence of defects in the lattice is usually undesired, as it lowers the electronic mobility and broadens the phonon dispersion relation [99]. However, in this section we will explain how it is possible to deterministically induce defects in the graphene sheet to tailor its chemical, thermal, electronic, and mechanical properties and realize devices with novel functionalities [25]. We first introduce different methods for the generation of defects in the lattice, with a particular focus on the irradiation with high energy particles. We then give a brief overview of the impact of the defects on the properties of graphene. Then, we discuss the transport properties of defect-engineered graphene by considering the generated defects as local potential barriers for electrons. We conclude this section with examples of coherent potential superlattices in graphene.

2.3.1 Defect-induced modifications of graphene properties

The presence of defects in the lattice impacts on many properties of graphene [99]. As a first example, the presence of dangling bonds in the defective sites enhances the surface chemical reactivity of graphene [100–103]. Indeed, simulations confirmed that hydroxyl, carboxyl, and other groups can interact with the defects [104]. The reactivity is also enhanced when atoms are rearranged without leaving any dangling bond, thanks to the recombination of the out-of-plane atomic orbitals [105]. Such enhanced chemical reactivity can be exploited to achieve deterministic surface functionalization [106] with applications in sensing, energy storage and energy harvesting [27–30, 107]. Structural defects in the lattice also have impact on the thermal conductivity of the crystal. The weakened carbon bonds locally soften the phononic excitations, thus reducing the thermal transport [108] and affecting the thermoelectricity at room temperature [109]. Indeed, by tailoring the thermal

transport, it is possible to also modify of the Seebeck coefficient of graphene, with impact on the design of photothermal detectors and spin caloritronics [110].
Besides chemical reactivity and phonon softening, the defects strongly impact the electronic properties of graphene [111]. Indeed, the latter stem from the periodic overlap of the orbitals, which determines the band structure (see Sec. 2.1.1 and [2, 3]). The absence or displacement of an atom breaks the periodicity of the crystal, thus modifying the orbital overlap and eventually the band structure [112]. The first intuitive effect is the reduction of the overall conductivity of the channel [113, 114], which can also transform graphene from semimetal to insulator in extreme cases [115]. The presence of defects can also open a local bandgap or bring the electrons into strong localization regime [100]. In addition, the electronic properties of graphene are modified as a consequence of the enhanced surface reactivity. Indeed, defected graphene exposed to air can attract adsorbates which induce doping, with macroscopic effects such as the reduction of the ambipolar effect, or the pinning of the Fermi energy in the channel [101, 116]. Moreover, disordered sites induce the localization of charges even in the absence of adsorbed molecules. In fact, when the periodicity of the crystal is broken, the orbitals of the displaced atoms do not hybridize into the band structure, but rather create localized modification of the density of states [117], as shown in Fig. 2.12a. Such sites can scatter the electron wave [115] and can therefore be treated as scattering centers or potential barriers for transport. In addition, the deterministic generation of defects in graphene can also be employed in studying light-matter interaction. Indeed, artificially induced lines of defects have been demonstrated to act as reflective boundaries for plasmon [32, 118], as shown in Fig. 2.12b.

2.3.2 Deterministic generation of defects

To take advantage of the modified properties of graphene, it is necessary to gain control on the generation of defects in the lattice. To this end, different methods have been studied to engineer defects in 2D materials [26]. Among the others, three principal methods to deliver the neces-

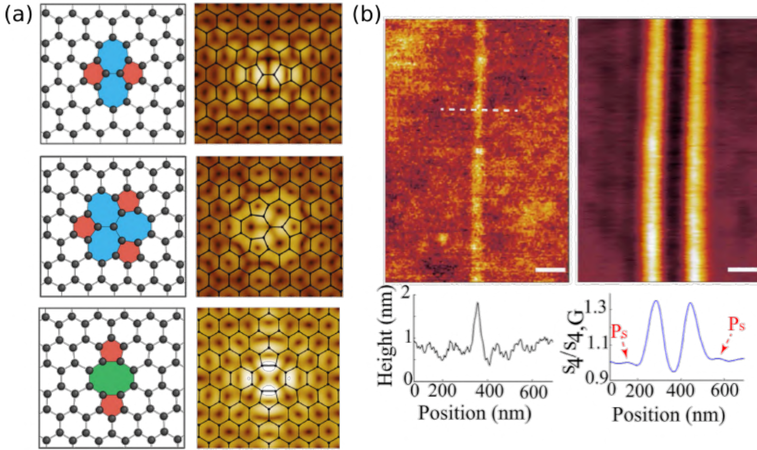

Figure 2.12 – (a) Graphical depiction (left) and simulated STM image (right) for three different structural defects in graphene: Stone-Thrower-Wales (upper), triple pentagon-triple heptagon (middle) and pentagon-octagon-pentagon (lower). The increased intensity in the proximity of the defected site reflects the modified DOS. Taken from [119]. (b) AFM measurement (left) and near-field measurement at $\lambda = 10.6\ \mu$m (right) of a graphene flake with a defected line generated with ion irradiation. Taken from [32].

sary energy to the lattice can be identified: plasma treatment [120], chemical treatment, and particle irradiation. The first two can be used to induce doping and/or implant substitutional atoms and adatoms in the lattice. However, the generation happens at random positions in the crystal and with little control on the yield. On the other hand, particle irradiation exploits the collisions between the impinging ions/electrons and the crystal atoms to induce doping and structural modifications in the lattice [111, 121–123]. In our experiment, we generate defects by electron irradiation, so we now focus on discussing this latter method. The simplest model to describe the interaction of a high-energy particle and an atom is to consider it as an elastic scattering between a relativistic particle (the incoming electron/ion) and a zero velocity heavy particle (the carbon atom), as depicted in Fig. 2.13 [124]. The collisions that transfer the maximum energy from the electron to the carbon atom are the one happening for $\vartheta = 0$, i.e., centered collisions. During

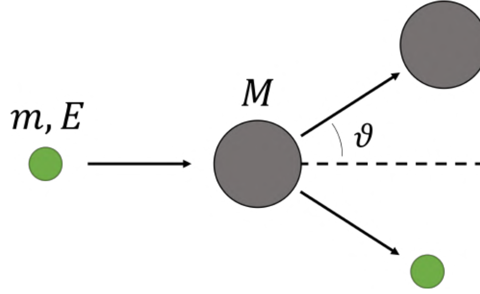

Figure 2.13 – Schematics of the scattering process of an incoming particle of mass m and energy E against a target atom of mass M. The transferred energy depends on the scattering angle ϑ. We only consider central collision, for which $\vartheta = 0$.

such scattering event, the energy transferred is [124]:

$$E_{max} = \frac{2ME(E + 2mc^2)}{(m + M)^2c^2 + 2ME} \tag{2.16}$$

where M is the mass of the carbon atom, m and E are the mass and the energy of the particle respectively, and c is the speed of light in vacuum. With this formula, it is possible to compute the necessary energy for an incoming particle to remove an atom from the lattice with an elastic collision. Such knock-on events happen when the transferred energy is equal to or larger than the binding energy of the atoms in the crystal, which is 18-20 eV for the carbon atoms in graphene [99].

Irradiation of particles with a large mass, such as ions, allows for larger energy transfer in more localized spots, thus yielding structural modification with high spatial resolution down to single vacancies. For example, irradiation with Ar^+ at 30 keV has been shown to induce localized vacancies in carbon nanotubes [127] and graphite [111, 125], as shown in Fig. 2.14a. Moreover, by selecting the ionic species it is possible to introduce impurities, thus modifying the local chemistry of the system [128].

Differently, the knock-on energy computed for electrons is 86 keV [26, 128], since they have a much lower mass than ions. Indeed, scanning tunneling microscopy (STM) experiments on suspended graphene [126] confirmed that electrons with energy larger than 86 keV can generate

knock-on damage (see Fig. 2.14b and c). For energy lower than that threshold, the damage on suspended graphene was negligible, indicating that the energy transferred by low-energy electrons is not sufficient for triggering knock-on events in suspended graphene. Nevertheless, structural defects are expected to form in graphene supported by a substrate (for example SiO_2), even if the knock-on threshold of carbon atoms is much higher than the energy transferred by a single collision of a low-energy electron. Therefore, we must take into account different energy transfer mechanism than the simple scattering of particles. For example, the impact resistance of graphene is reduced when the lattice contains already some defected sites, and electrons with energy as low as 5 keV are expected to induce disruptions from such sites [130]. All real graphene samples present a certain amount of defects, for example contaminants, thus allowing structural damage in suspended graphene also with low-energy irradiation, as shown in Fig. 2.15a. Moreover,

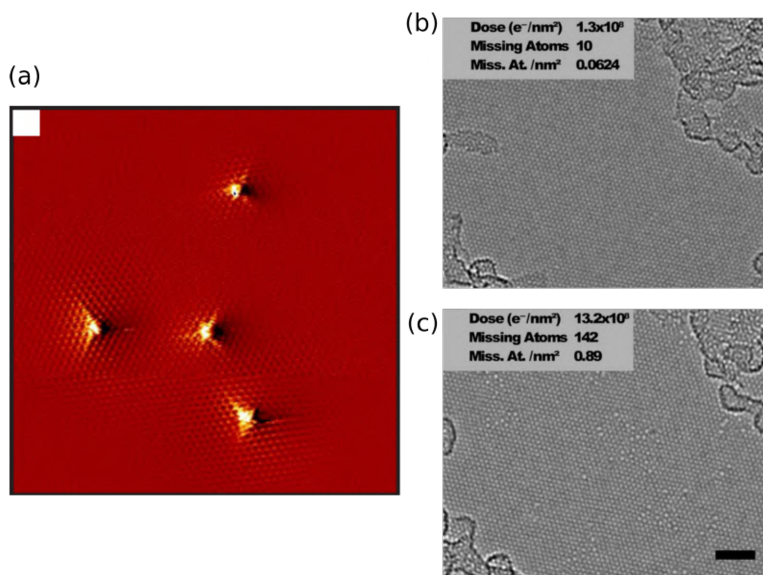

Figure 2.14 – (a) 17x17 nm^2 STM image, measured at 6 K of a graphite surface after irradiation with Ar^+ ions. Taken from [125]. (b, c) Evolution of graphene under TEM observation with electrons at 100 keV. For low doses, the crystal structure shows very few defects (b). When increasing the dose, the impinging electrons cause knock-on damage on the structure. The scalebar is 2 nm. Taken from [126].

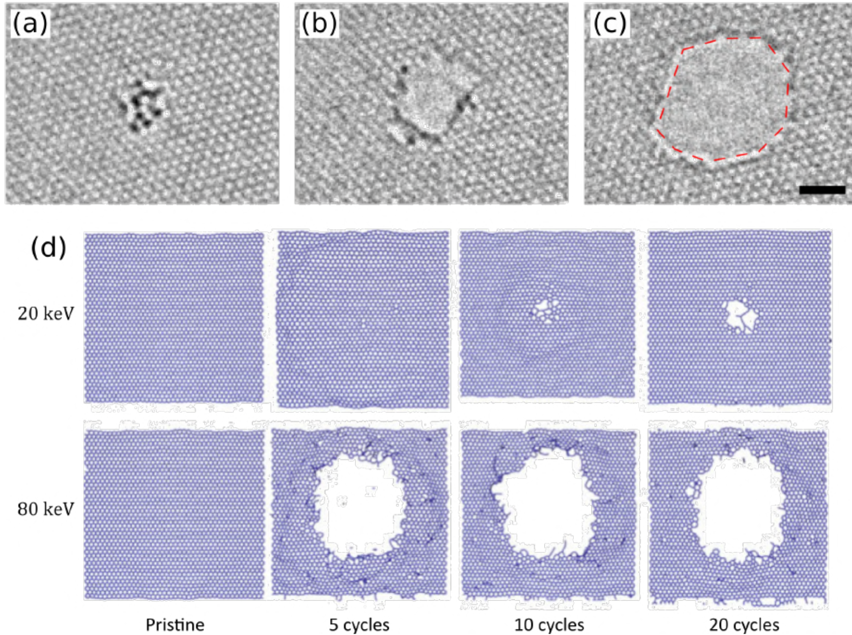

Figure 2.15 – (a-c) Creation of holes in suspended graphene can happen also for low-energy electrons, thanks to the defects already present in the lattice. Indeed, the holes nucleate at contamination sites (a), then start growing as long as the contaminants are still bound to the edges. Eventually, the contaminants are removed and the growth stops, leaving a clean hole in the graphene crystal. Taken from [126]. (b) Molecular dynamics simulations of graphene supported by SiO_2. Defected sites are expected to form also for low-energy irradiation, as an effect of the presence of the substrate. Taken from [129].

lattice disruption is expected due to the accumulation of charged puddles on the surface or within the subsurface [131]. Such puddles create electrostatic fields which can reach instant values sufficiently strong to induce severe damage to the graphene lattice [131, 132]. Molecular dynamics simulations show that, thanks to such effects, defects in graphene supported by SiO_2 are induced by the irradiation of electrons with an energy of 20 keV, also when the starting crystal is not damaged (see Fig. 2.15b). Alternatively, beam-induced chemical etching can be a viable mechanism for the creation of defects. The chemical species which might be responsible for such effects can be reactive oxygen-based compounds coming from the substrate [133] or from organic residues

trapped between graphene and substrate [134]. The energy transferred by the irradiation can catalyze chemical reactions, which locally break graphene with a process similar to the chemical etching induced by oxygen ions (see Sec. 3.1.6). Thanks to these effects, low-energy electrons can be employed for locally engineer defects in graphene with nanometric precision. Furthermore, low-energy electron beam can be conveniently coupled to a pattern generator in a Scanning Electron Microscope (SEM) [25, 26, 100, 135]. The pattern generator allows the scanning of the beam on regions of the crystal selected with nanometric precision. Thus, it is possible to generate defects following complex geometries, thus enabling the creation of pre-determined defective structures with chosen impact on the graphene channel, for examples regular arrays of defected lines.

2.3.3 Effects on transport of periodic arrays of defects

As discussed above, defects impact the transport properties by scattering electrons and, in some configurations, by inducing strong localization. In this framework, further effects can be unlocked if the defected features are periodically repeated, thanks to coherent effects arising from the engineered long-range order. For example, the repetition of lines have been studied to enhance the control of the valley degree of freedom in valleytronics [136], and the generation of superlattices in the crystal can also enable the fine tuning of the graphene band structure [137].
To understand the effect on transport of the repetition of defective lines, we consider the defects as potential barriers in the otherwise quasi-ballistic propagation of the electrons inside graphene. Before studying an ordered structure of potentials, we first focus on the transmission of a single barrier in graphene.
In Sec 2.1.1, we described how low-energy excitations in graphene do not behave like massive electrons with a parabolic dispersion relation, but rather show a linear dispersion and thus behave like massless Dirac fermions. Such linear dispersion can be interpreted as the result of the crossing of two bands, each coming from one of the two sublattices of

graphene [6, 42], as depicted in Fig. 2.16a. This yields an additional degree of freedom for graphene low-energy excitations, called pseudospin. Thanks to the pseudospin, the electrons scattering on a potential barrier in graphene can experience Klein tunneling [9].
Klein tunneling is a particular quantum electrodynamical effect in which the reflectance of a wide barrier is zero for perpendicular incidence, and arises from the fact that excitations at negative and positive energies are described by two components of the same spinor wavevector [138]. If we consider a barrier of height V_0 and thickness D (as shown in Fig. 2.16b), the transmission T for an incoming electron of momentum $\mathbf{k} = (k_x, k_y)$ and energy E is [9]

$$T = \frac{\cos^2 \phi}{1 - \cos^2(q_x D) \sin^2 \phi} \tag{2.17}$$

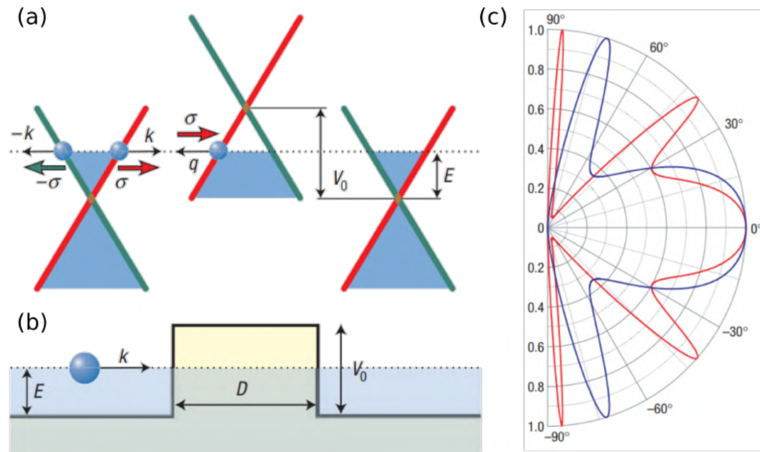

Figure 2.16 – (a) Low-energy excitation spectrum in graphene. The two original bands forming the Dirac cone are highlighted with red and green. The pseudospin is parallel to the momentum for energies $E > 0$ and antiparallel for $E < 0$. (b) Potential profile of a barrier of width D and height V_0. The blue shaded area represent the occupied states. The Fermi energy (dotted line) is in the conduction band outside the barrier, and in the valence band when inside. (c) Transmission probability T as a function of the incident angle ϑ, computed with Eq. 2.17 for a barrier of width $D = 100$ nm and height 200 meV (red curve) and 285 meV (blue curve). Taken from [9].

where ϕ is the in-plane angle of incidence against the barrier and $q_x = \sqrt{\frac{(E-V_0)^2}{\hbar^2 v_f^2} - k_y^2}$ is the x component of the propagation vector of the electron inside the barrier. Fig. 2.16c shows the transmission computed with Eq. 2.17 for electrons of energy E impinging on a barrier of thickness $D = 100$ nm and height $V_0 = 200$ meV (red curve) and $V_0 = 285$ meV (blue curve). From the curves, it is possible to notice two main general facts: first, for angles $\phi \neq 0$, the equation describes resonances every $q_x D = \pi N$, with N integer, which can be seen as resonances of a Fabri-Pérot cavity, which arise from the quantum interference of the ballistic electrons between the two barriers. Moreover, $T(\phi = 0) = 1$, indipendently from the barrier parameters. This effect can be explained by considering the conservation of the pseudospin: since the potential barrier cannot change the pseudospin, then a right-moving electron can be scattered into a right-moving electronic ($E > 0$) state or into a left-moving hole ($E < 0$) state (i.e., it is not possible for particles to be scattered on differently colored branches in Fig. 2.16a). This effect has a strong impact on the transport properties of graphene, also when no potential barrier is applied. Such effect is indeed the reason why electrons in graphene show long ballistic transport lengths [12], with reported observations up to tens of micrometers [13]. Such long ballistic transport is due to the reduced backscattering efficiency of impurities and point defects, and is preserved also in the presence of long range disorder, for example induced by the substrate [14]. In effect, the pseudospin can be changed only by local potentials with length-scales of the the order of the lattice constant (intervalley scattering, [9]), which can influence the two sublattices independently. Point defects induced locally in the lattice are in principle capable of such intervalley scattering [114]. Nevertheless, charged defects screen the short-range potential with a long-range Coulomb potential arising from their charge, thus suppressing intervalley scattering [139]. Indeed, effects of Klein tunneling have been observed also in defected graphene [140] and disruption of such effects have been predicted to happen only if foreign atoms are chemically bonded to the crystal surface [141]. Such effects explain why graphene show large ballistic lengths and justify the partial analogy between defected lines and potential barriers.

Generally, in experimental conditions, a situation similar to the one shown in Fig. 2.16b can be achieved by the use of local top gates. By applying a potential to the top gate, a $n-p$ junction and a $p-n$ junction can form in series [142], thus creating potential barriers of chosen width. The transport properties of a single $n-p$ junction are determined by the probability of an electron in the conduction band approaching the potential barrier to emerge in the valence band after the barrier conserving its momentum and pseudospin properties [143]. For a single step-like barrier, such probability $w(\phi)$ can be computed by taking the limit $D \to 0$ in Eq. 2.17, which is $w_{step} = \cos^2\phi$. Conversely, if the barrier raises linearly with a length scale d (such is the potential increase induced by local gates [144]), a classically forbidden zone arises for $\phi > 0$. To be transmitted, the incoming electron must therefore tunnel through this forbidden zone [143, 144], and the resulting transmission probability becomes (for $k_F d \gg 1$)

$$w(\phi) = e^{-\pi(k_F d)\sin^2\phi} \tag{2.18}$$

For $\phi = 0$, the conservation of the pseudospin (and thus the Klein tunneling) is granted, as $w(0) = 1$ regardless of the value of d. However, the transmission for finite angles is hindered by the tunnel barrier, and gate-induced heterojunctions selectively transmit only quasiparticles approaching at low angles. With such considerations, effects of the perfect transmission have been studied also in diffusive systems [145], where the heterojunction was treated as a series of diffusive channels with ballistic interfaces between them. Klein tunneling has also been observed in double-gated graphene [146] thanks to the quantum interference between ballistic heterojunctions [10]. Moreover, the effect of coherent transport and Fabri-Pérot resonances have been observed in conduction measurements in superconductor-graphene heterostructures [148] as oscillations in the channel conductivity [147], as shown in Fig. 2.17. All these coherence effects are preserved even in disordered system, as long as the mean free path of the electron is larger than the interdistance between the junctions [149].
When the single barrier is repeated to form a superlattice, Klein and standard tunneling strongly impact the transport properties of the

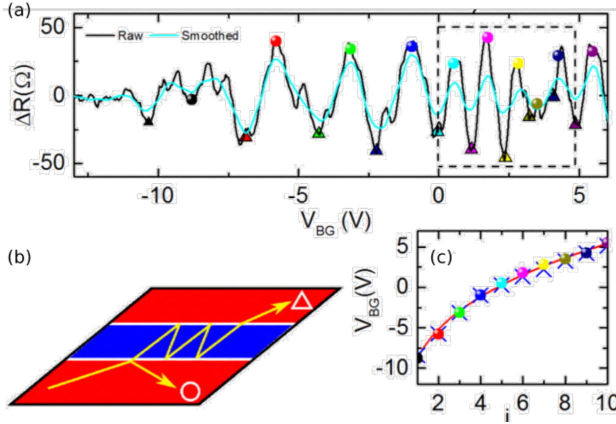

Figure 2.17 – (a) Resistance oscillations measured in graphene where a line of charges was deposited perpendicular to the channel as a function of the backgate voltage V_{BG}. (b) Schematics of the induced Fabri Pérot cavity, highlighting the origin of the deeps (when the electrons are transmitted, triangles) and the peaks (when the electrons are reflected back, circles) in resistance. (c) Voltage position of the peaks in (a) as a function of the peak number. Taken from [147]

channel. Fig 2.18 shows the simulated transmission T of electrons propagating along x through ten repetitions of a barrier of height $V_0 = 50$ meV and width $D = 50$ meV. The separation between the barriers is $d = 100$ nm. The transmission is 1 for $k_y = 0$, regardless of the value of k_x (i.e., normal incidence), as an effect of the Klein tunneling [11]. For finite values of k_y, minibands form as a result of the quantum interference between the Fabri-Pérot modes inside the barriers, thus allowing transport through the potential superlattice. The presence of the minibands result in an oscillatory behaviour of the conductance of graphene as a function of the injection energy [11, 150, 151]. Such oscillatory behaviour is expected to persist even when the barriers are randomly spaced [152]. Fig. 2.18b shows the simulated dependency on injection energy E of the conductance (normalized on the conductance quantum $G_0 = 2e^2/h$) of a graphene nanoribbon with unevenly spaced potential barriers. The barriers have height $V_0 = 0.3$ eV and width $d = 40$ nm, while the spacing is randomly chosen with a uniform probability distribution between 150 nm and 250 nm. The conservation of the oscillatory behaviour is explained by considering the single propagating

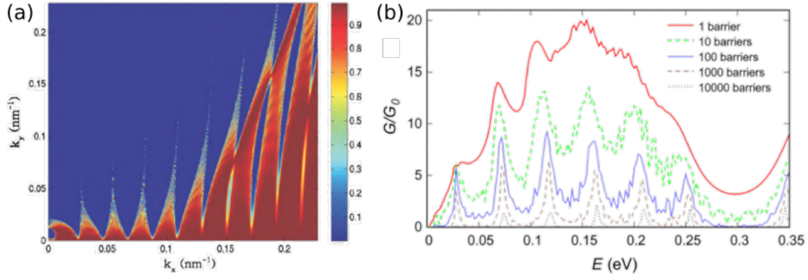

Figure 2.18 – (a) Simulated transmission T of electrons through ten repetitions of a barrier of height $V_0 = 50$ meV, width $D = 50$ meV, and separation between barriers $d = 100$ nm. Taken from [11]. (b) Normalized conductance G/G_0 of a graphene ribbon with unevenly spaced potential barriers as a function of the injection energy E. The barriers have height $V_0 = 0.3$ eV and width $d = 40$ nm. The spacing between the barriers is randomly chosen with a uniform probability distribution between 150 nm and 250 nm. Taken from [152].

modes of electrons. When the barriers are orthogonal to the ribbon edges, they do not intermix different electronic modes and therefore the main behavior is governed by the properties of the single barrier. Indeed, the effect of a potential superlattice has been observed to induce conductance oscillations in a graphene nanoribbon [33].

Chapter 3

Materials and methods

In this chapter, we summarize the fabrication and measurement procedures exploited throughout this work. First, we begin with general information on electron beam lithography (EBL), which is used for most of the samples. Then, we describe the isolation of graphene through mechanical exfoliation from bulk graphite. Afterwards, we introduce Fourier transform infrared spectroscopy (FTIR) technique in three different geometries: standard far-field, microscopy and attenuated total reflection (ATR). Last, we show the setups we exploited for transport measurement both in air and vacuum. A detailed list of all the recipes can be found in Appendix A. All the samples were fabricated in the ISO 6 cleanroom facility at NEST laboratories. The optical, electronic and spectroscopic measurements were performed partially at NEST and partially in the laboratories at Dipartimento di Fisica "E. Fermi" of the University of Pisa.

3.1 Device Fabrication

3.1.1 Electron beam lithography

Electron beam lithography (EBL) is a fabrication procedure for creating structures with nanometric details and is commonly employed in both research and industry. It consists in a focused beam of electrons, which is scanned on pre-selected areas of samples covered with an

electron-sensitive polymeric film called resist. This way, EBL allows the generation of masks for selectively depositing metals and/or etching custom structures. For our work, we employed an Ultra Plus scanning electron microscope (SEM) from ZEISS coupled to a pattern generator from Raith GmbH with nanometric resolution. The EBL chamber is equipped with an interferometric stage that allows nanometric alignment precision. Computer-aided designs (CADs) of the patterns to expose were drawn on Elphy, a proprietary software from Raith GmbH. A schematic depiction of the typical EBL procedure is shown in Fig. 3.1. The chosen substrate is first diced into roughly 5x5 mm^2 squares from the whole wafer with a diamond tip. Each substrate is then cleaned with the standard cleaning procedure for removing debris from the cleaving (Fig. 3.1a). A thin film of PMMA 950k (AR-P 679.04 from AllResist) is spin coated on top of the substrate and then soft baked to remove the solvent and make the film uniform (Fig. 3.1b). The coated sample is exposed to the electron beam following pre-drawn CADs. Electrons impinging on the chip break the polymeric chains in the resist, which therefore becomes more soluble than the unexposed part (Fig. 3.1c). The exposed part of the polymer film can then be selectively removed

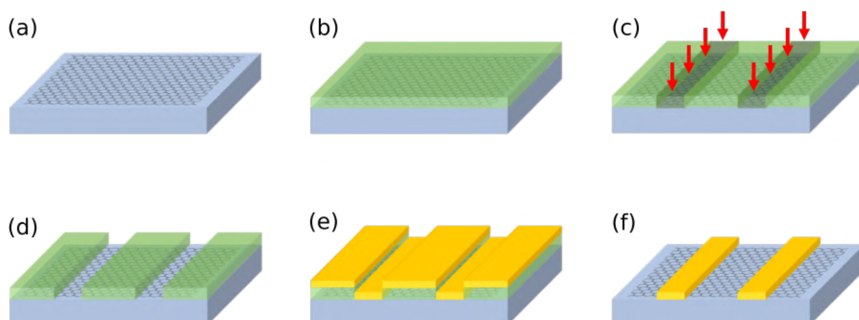

Figure 3.1 – Schematics of the standard EBL procedure. First, the substrate is cleaned with the standard cleaning procedure (a). Then, e-beam resist is spin coated on top of the sample (b) and is exposed following one of the recipes for EBL (c). The exposed resist is removed in a suitable developing solution, thus leaving holes and creating a mask (d). Metal is then deposited via thermal evaporation in high vacuum (e). Finally, the polymer mask is removed with acetone (lift-off procedure), leaving metal only on the unmasked part of the sample (f).

by using a suitable chemical solution called developer (in our case, AR 600-56 from AllResist). During the development, the continuous polymeric film becomes a mask with holes where the resist was exposed (Fig. 3.1d).

The achievable resolution of the EBL technique is largely influenced by the energy of the electrons in the beam. Larger energies allow for a smaller beam waist, thus increasing the spatial resolution. However, too large energies may damage the target, especially if graphene is present (see also Sec. 2.3.2). To fabricate the devices for optical experiments, we chose a trade-off energy of 20 keV that allowed the patterning of large arrays of tens of micrometers composed by elements with characteristic lengths of hundreds of nanometres while preventing damages to the sample. To optimize the obtained patterns, we tested different CAD geometries and different exposure times. Such procedure will be discussed in Sec. 4.2.2 and the parameters employed are reported in Appendix A.

The masked device is then put in a thermal evaporator for the deposition of metallic films. We employed a system by Sistec capable of reaching high vacuum ($< 10^{-5}$ mbar). Depending on the device, we evaporated Cr, Au and/or Ti. We controlled the thickness of the deposited metal with nanometric precision by means of a piezoelectric crystal positioned on the sample carousel. During this process, a thin metallic film deposits uniformly on the sample (Fig. 3.1e).

After the deposition of the metallic film, the sample is put in acetone, which dissolves the polymer resist. Such lift-off step removes the metallic film from the unexposed part of the sample, thus leaving only the desired pattern adhering on the substrate (Fig. 3.1f). After the whole process, the sample is cleaned with the deep cleaning procedure (See Appendix A) and the sample is ready for either measurements, if the EBL was the last fabrication step, or successive fabrication steps, for example the exfoliation of graphene.

3.1.2 Exfoliation of graphene

Different techniques have been developed to isolate 2D crystals [154, 155]. For this work, we use a refined version of the method firstly presented by Novoselov and Geim [156, 157] in 2004. This method is known as mechanical exfoliation: a high-quality bulk crystal of the desired material is thinned using adhesive tape by repeatedly cleaving it with the adhesive part of the tape. This process is repeated between 2 and 10 times, depending on the desired flake thickness and the material to be exfoliated. A graphic explanation of the process is shown in Figure 3.2.

Via the mechanical exfoliation it is possible to obtain monocrystalline flakes with clean, sharp, almost defect-free surfaces. As a drawback, this method does not offer good control on the obtained samples: it is not possible to decide in advance the shape and size of the flakes, which vary greatly with each exfoliation. In the following sections, we introduce all the steps to isolate high-quality graphene flakes by using this technique.

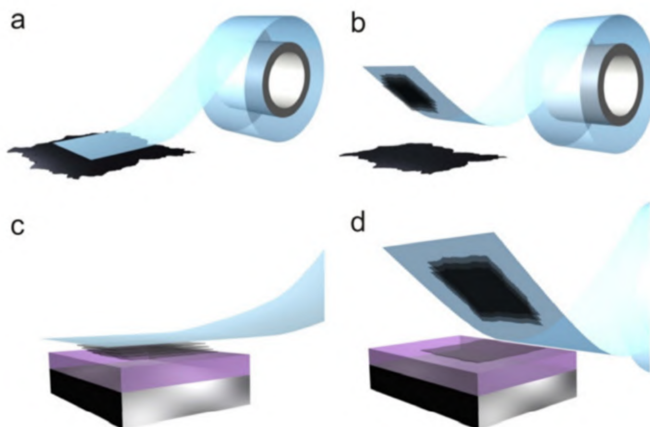

Figure 3.2 – Mechanical exfoliation of 2D crystals: (a) tape is brought into contact with a bulk crystal and some layers of it stick to the tape (b). After some repetition of this process, the tape is then pressed on the chosen substrate (c); peeling off the tape, thin flakes remain on the substrate thanks to Van der Waals attractive force (d). Picture taken from [153].

3.1.3 Preparation of the substrate

The substrate chosen for the exfoliation is a doped Si wafer with ~ 300 nm of thermally grown SiO_2 on top. This particular substrate allows to have good optical contrast for monolayer graphene thanks to optical interference [158, 159]. To facilitate retrieving the flakes and to allow a precise alignment of the CADs for successive steps, a grid of markers is fabricated on top of the substrate before the deposition of the flakes by means of EBL (Recipe 2 in Tab A.1). After the lithography, the substrate chips are cleaned by oxygen plasma at 100 W to remove organic residues on the surface and to promote the adhesion of graphene.

3.1.4 Tape technique

We peel off high-quality graphite crystals purchased from NGS Naturgraphit with silicon-free wafer processing tape from SPS International. After some steps of exfoliation, we press the tape on a SiO_2 chip with markers. Afterwards, we peel off the tape from the substrate, thus leaving some crystals on it. It is important to peel off in a slow, controlled motion and not to bend the tape much not to crack the crystals. This technique yields high-quality flakes with varying shapes and thickness. The average lateral dimension is several micrometers, even if much bigger crystals up to 1 mm are reported [160]. Once the tape is removed, the chips are searched with an optical microscope and the retrieved flakes are listed in a database according to their coordinates on the marker grid. Two examples of exfoliated graphene crystals are shown in Fig. 3.3a and b. Monolayer crystals are recognizable by their contrast with respect of the substrate. We employed an optical microscope by Nikon with a red filter to enhance the contrast of the monolayer flake (see Fig. 3.3a and b). With the chosen substrate and the red filter, the optical contrast measured in the red channel for a monolayer flake is $\sim 87\%$ of the signal measured on SiO_2. The optical identification of the monolayer flakes is usually precise with this method but more information on the thickness and quality of the crystal can be determined by Raman spectroscopy (see Sec. 2.1.3).

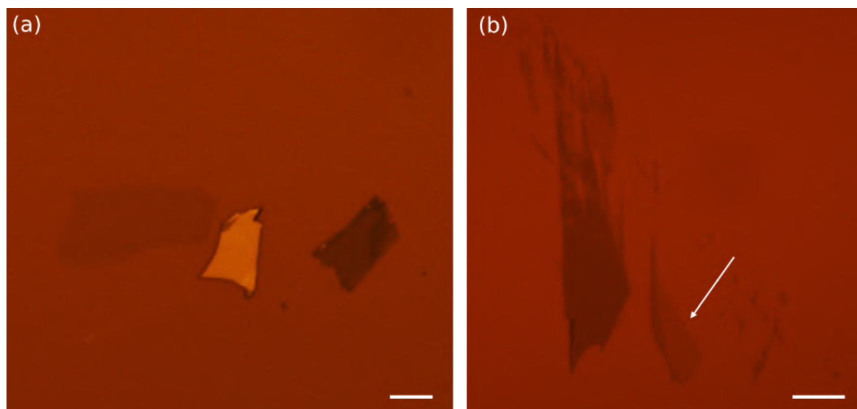

Figure 3.3 – (a) An example of large isolated monolayer flake (the grey shape on the left) with much thicker flakes (yellow and dark grey). The scalebar is 10 μm. (b) For few-layer crystals, different shades are related to the thickness. Monolayer graphene (pointed by the white arrow) is the faintest. The thicker the crystal, the darker the shade. The scalebar is 20 μm.

3.1.5 Chemical vapour deposition

The mechanical exfoliation method shown in the previous section has a very low scalability, and it is not convenient if a number of large-area flakes are required. For our experiments on light-matter interaction, we need several flakes with areas of hundreds of μm^2 (see Sec. 3.2.2). To achieve such yield, another technique can be used for the isolation of graphene: artificial synthesis via chemical vapour deposition (CVD) [161]. The process of CVD is performed in a heated chamber called reactor. Hydrocarbon precursor gases are injected in the reactor and decompose in carbon radicals because of the temperature. The carbon radicals then deposits on a metal substrate (in our case, copper) present in the reactor, and combines in the form of graphene. The CVD enables the growth of graphene covering very large areas. However, the reaction starts at different nucleation sites with random orientation of the crystal lattice. Thus, graphene grown via CVD contains a lot of grain boundaries [162] and has in general a lower crystal quality with respect to the mechanically exfoliated one.
To solve this issue, it is possible to fix the nucleation sites by depositing

chromium seeds on the copper substrate before the growth (seeded CVD [163]). By generating a regular pattern of seeds, it is possible to cover large areas with an array of monocrystalline high-quality flakes with lateral dimensions of hundreds of micrometers.
Once grown, the graphene is transferred from the copper foil to the target substrate via the semi-dry transfer method (see Supporting Information of [163]). The copper foil is covered with a thin film of PMMA and framed with Kapton tape to support the structure. The membrane with graphene is then detached from the copper substrate using electrochemical delamination: the Cu/Gr/PMMA stack is put in a solution of NaOH and a voltage is applied between the substrate and a copper counter electrode. The bubbles created by the electrochemical reaction mechanically detach the Gr/PMMA membrane from the copper substrate. The membrane is then removed from the solution, rinsed with deionized water and dried in ambient conditions.
The obtained membrane, supported by the Kapton frame, is then mounted in a micromechanical manipulator for the deterministic deposition of graphene on the target substrate. The deposition is performed by slowly bringing in contact the membrane with the substrate, which is then heated to promote the adhesion of graphene. At the end of the procedure, the PMMA film is removed from the structure by soaking the sample in acetone. Fig. 3.4 shows an example of the regular array

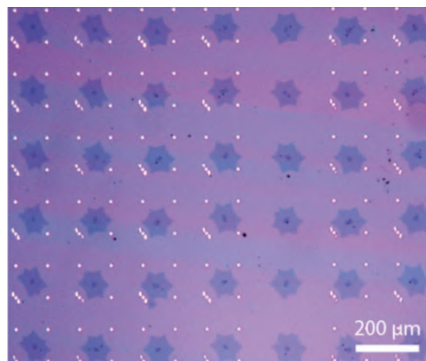

Figure 3.4 – Regular array of monocrystalline graphene flakes obtained with the method of seeded CVD growth and transferred on a Si/SiO_2 substrate via the semi-dry transfer method. Taken from [163].

of monocrystalline flakes deposited on a Si/SiO_2 substrate with this method.
For our experiments, we employ graphene grown with the seeded CVD method and transferred on the samples by Dr. Vaidotas Mišeikis from IIT, in the group of Dr. Camilla Coletti at NEST.

3.1.6 Reactive ion etching

The flakes isolated with the mechanical exfoliation come in random shapes and dimensions, and the edges of the CVD-grown flakes are usually not sharp. If specific geometries are required, for example a graphene channel with predetermined thickness, it is possible to cut the flake with reactive ion etching (RIE) [164, 165]. In a RIE chamber, a selected mixture of gases is ionized in vacuum with radio-frequency electromagnetic waves. The ions are delivered vertically on the wafer thanks to the DC voltage generated between the chamber and the electrically isolated plate where the wafer is placed on. Upon collision, the ions chemically react with the surface atoms. Depending on the chosen gas mixture, different atoms can be selectively removed thanks to the chemical interaction with the ions. RIE is strongly anisotropic thanks to the vertical trajectory of the colliding ions.
A schematic depiction for the steps for cutting graphene channels with RIE is shown in Fig. 3.5a-c. First, a negative mask that cover the parts of the flake that must be preserved is created with lithography (see Sec. 3.1.1). Once developed, the masked sample is put in the RIE chamber to etch graphene with oxygen/nitrogen plasma for 50 s (see Appendix A). Since this gas mixture attacks carbonaceous materials and SiO_2, we chose such process time because it is enough to eliminate monolayer parts without strongly deforming the polymeric mask. Because of this choice, however, only a few graphene layers can be removed. Thus, we preferentially selected well-isolated monolayer flakes like the one shown in Fig. 3.5d, which yield an easier fabrication with lower risk of electrical short-circuiting due to undesired thick graphene residues. After RIE, the sample is put in acetone and cleaned with the standard procedure. An example of flake before and after the RIE step is shown in Fig. 3.5d.

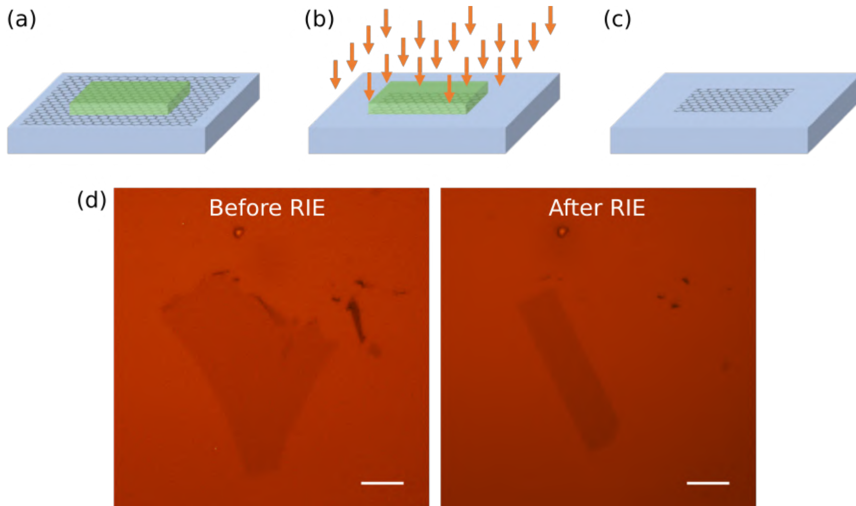

Figure 3.5 – A polymeric mask is fabricated on the sample via EBL (a). The sample is then placed in the RIE chamber. Here, ions approach vertically the sample and chemically react with atoms at its surface, removing them (b). After the process, the mask is removed with acetone, thus leaving the shaped flake (c). (d) Example of flake before and after the RIE process. The shape of the exfoliated flake is not regular, with wrinkled borders (left). RIE allows to cut regular shapes thanks to the lithographic masks and the anisotropic etching (right). The scalebar is 10 μm

3.1.7 Raman Spectroscopy

In Sec. 2.1.3, we discussed how Raman spectroscopy is a powerful tool for studying the crystal properties of graphene. Indeed, Raman spectroscopy relies on the inelastic scattering of photons impinging on a molecule or crystal lattice. In the sample, different energy levels are available, according to the vibrational modes of the system (see Fig. 3.6). When monochromatic light impinges on the sample at a fixed energy, larger than the vibrational energies, it creates excitations to virtual energy states, as shown in Fig. 3.6. Three different decaying paths are then possible: one elastic process and two inelastic processes. Rayleigh scattering (B in Fig. 3.6) is the elastic scattering of the incoming photon and is usually the main decay path. Stokes Raman scattering (C in Fig. 3.6) is a process in which the incoming photon loses energy by

the inelastic scattering with phonons in the material, while anti-Stokes Raman scattering (D in Fig. 3.6) is the opposite process, in which the incoming photon gains energy from the inelastic scattering with the phonons in the system. By studying the spectrum of back-scattered light, it is possible to gain information on the vibrational states of the crystal, i.e., on its phononic structure and the interaction of the latter with the electron gas.

For our experiment, we employed an InVia Raman microscope by

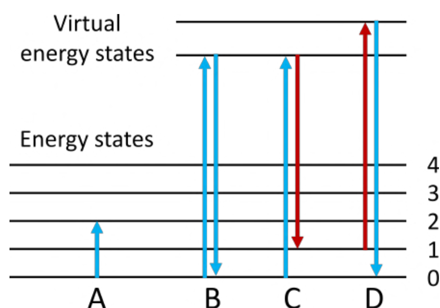

Figure 3.6 – Energy-level diagram showing different processes involving light: infrared absorption (A), Rayleigh scattering (B), Stokes Raman scattering (C) and Anti-Stokes Raman scattering (D).

Renishaw, equipped with a green laser at 532 nm. We used a 100x objective with a numerical aperture NA = 0.85, which yields a lateral resolution < 1 μm. When studying the crystals in which we induced defects via EBI, the laser power was set at 118 μW to avoid any heating of the lattice coming from the light. Indeed, the increased thermal energy of the crystal could partially heal the defects. We collected point measurements to quickly check the presence of graphene. We used longer line scans or map scans with a step of 500 nm to study the properties of selected areas of our samples. As a first advantage, mapping allowed us to reconstruct the spatial distribution of the induced defects. Moreover, mapping improved the significance of the data. Indeed, low-power measurements usually show a low signal-to-noise ratio. However, thanks to the maps, we could average a large number of positions and use the averages and standard deviations as data points and statistical errors respectively. The data collection was performed by Dr. Federica Bianco from CNR-NANO at NEST. To analyze the large amount of

data collected from the mapping, we custom-made a Python library for automatically fitting the spectra and manipulating the fit parameters.

3.1.8 Atomic Force Microscopy

Atomic force microscopy (AFM) is a technique to reconstruct images of the surface of samples with nanometric spatial resolution, often employed to study 2D materials [166]. The schematics of AFM is shown in Fig. 3.7: the sample to analyse is placed on a piezoelectric stage. The local probe is a cantilever with a nanometric tip. The nanometric tip is put in close contact with the sample and is thus deflected by the short-range interaction force. Such deflection is measured by a laser beam, which is reflected by the tip onto a position-sensitive photodiode detector. When moving the stage, the interaction between the sample and the tip changes, thus modifying the force and consequently the deflection. By using the measured deflection, it is possible to reconstruct the local topography of the analysed sample with nanometric resolution. AFM can be used in two different modes: contact mode and tapping mode. During contact mode, the cantilever is kept in contact with the sample and the feedback of the photodiode ensures that the deflection is constant over the measurement (i.e., the force between the sample and the tip is constant). Contact mode can be used to reconstruct the topography of hard samples and can be used for measuring the mechanical properties of the substrate, such as the Young modulus. Conversely, when in tapping mode, the cantilever is oscillated near its resonance frequency by a piezoelectric actuator. The feedback of the photodiode keeps the oscillation amplitude constant during the scan. Thanks to the oscillation, the tip contacts the sample only at one end of the oscillation, thus minimizing the interactions. With tapping mode, it is possible to both reconstruct the topography of the samples and to collect measurements of the phase of the measured oscillation with respect to the actuator oscillation. Phase measurements can be used to gain information on the local adhesion and elasticity of the sample.
In our experiments, we employ a Dimension ICON-PT AFM from Bruker. The samples are measured in tapping mode, and maps are acquired in high-resolution mode (1024x1024 pixels) with a scanning

velocity of 500 nm/min. The resulting resolution is ~ 2 nm/px. The data collection was performed by Dr. Filippo Fabbri from CNR-NANO at NEST, while the acquired data where analyzed both with Gwyddion software and with a custom software.

3.2 Fourier Transform Infrared Spectroscopy

Fourier Transform Infrared (FTIR) spectroscopy is used to study the absorption spectrum of a sample by measuring the transmission or reflection of a broadband source of light [168]. An FTIR spectrometer is basically a Michelson interferometer, as shown in Fig. 3.8. The light emitted from a broadband source of light impinges on a beam splitter, which divides it into two beams. One is deflected towards a fixed mirror, and the other towards a mirror that can move back and forth. Light reflected by the mirrors recombines at the beam splitter with a particular interference pattern, depending on the difference in the optical path of the two branches. Such beam is focused and interacts with the sample. Afterwards, light is collected by a detector which measures its intensity. By changing the difference in the optical paths with the movable mirror, it is possible to reconstruct an interferogram,

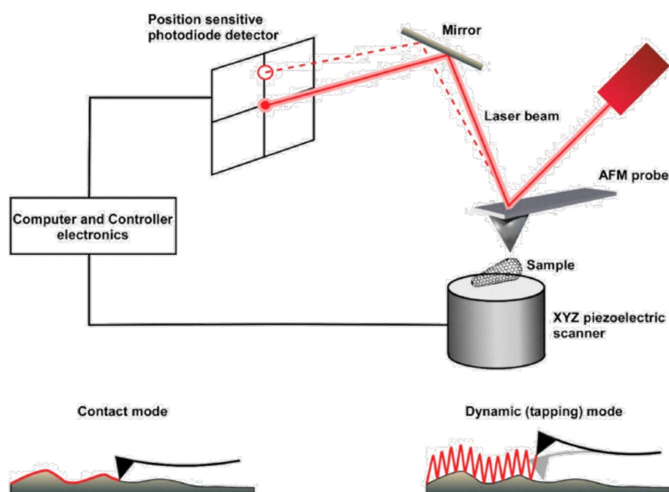

Figure 3.7 – Schematics of the functioning of an AFM. Taken from [167]

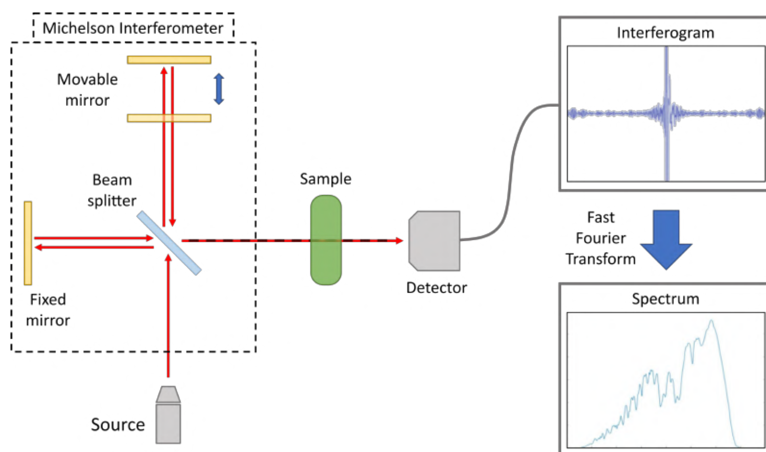

Figure 3.8 – Schematics of a FTIR setup. The source injects broadband light into a Michelson interferometer with a movable mirror. The beam recombines at the interferometer output and is sent in the sample chamber. Afterwards, the signal intensity is collected by a detector as a function of the mirror position, thus generating an interferogram. The interferogram is then fast Fourier transformed to reconstruct the absorption spectrum

which is a plot of the intensity at the detector as a function of the mirror position. By applying a fast Fourier transform (FFT) algorithm to such interferogram, it is possible to reconstruct the transmission or reflection spectrum of the sample under examination. With respect to standard spectroscopy [169], FTIR shows three main advantages: first, the full spectrum reaches the detector simultaneously in FTIR spectroscopy, while in the standard case only one frequency at a time is collected by the detector, thus reducing the time needed for a single collection. Second, since the optical path of FTIR spectrometers is much simpler and there is no monochromator, the collected power is greater than in the standard case. Finally, the frequency resolution is determined by the movement of the mirror instead of the quality of the grating and the slit of the monochromator as in the standard case. Thanks to these three advantages, FTIR is capable of fast measurements with large signal-to-noise ratio and resolution. In our experiments we employed two different FTIR spectrometers: a Magna-IR 860 spectrometer by Nicolet and a FT/IR-6800 by Jasco. With the first one, we performed low and

room temperature measurements inside a cryostat. The instrument is equipped with a mercury cadmium telluride (MCT) detector cooled with liquid nitrogen, which therefore offers high sensitivity and signal-to-noise ratios thanks to its low working temperature. Instead, the FTIR by Jasco is equipped with a deuterated triglycine sulfate (DTGS) detector and its sample chamber can be pumped to vacuum, so we employed it for reducing air absorption.

3.2.1 Multipass geometry

FTIR can be efficiently used to measure ISB transitions in quantum wells. Since such transitions can only be excited by out-of-plane electric fields (see Sec. 2.2.1), they must be measured by using a specific geometry, called multipass. For this measurement, the sample is prepared as shown in Fig. 3.9a: the surface close to the QW is covered with a thin Au film, in order to maximise the overlap of light with the QWs. The lateral facets are then manually lapped at $\vartheta = 45°$ with multiple steps of sanding. Since the FTIR beam enters and exits the sample from these facets, they are polished with diamond paste to minimise the roughness, which causes the scattering of light at the sample-air interfaces. Incoming light is linearly polarized with either transverse electric (TE) or transverse magnetic (TM) polarizations. TE polarization has an electric field in the y direction (see Fig. 3.9b), while in TM polarization the electric field lies in the $x-z$ plane. Thanks to the tilted facets, the electric field in the TM polarization has an out-of-plane component $E_{\perp} = E_0 \sin(\vartheta)$ which can excite the ISB transition (see Sec. 2.2.1). On the contrary, TE polarization cannot couple with ISB transitions, since it does not have a component of the electric field perpendicular to the QW plane. Moreover, when light is injected into a sample of length L and thickness h, it is confined in the sample thanks to the metal coating and total internal reflection at the uncovered surface. Therefore, for injection perpendicular to the lapped facet in the case under examination, the beam is reflected every $l = h/\tan(\vartheta) = h$. Consequently, it performs a number of passages $N = L/l$ through the QW active area in the structure, from which the name of this technique. Due to the multiple passages, if the absorbance of the single transition

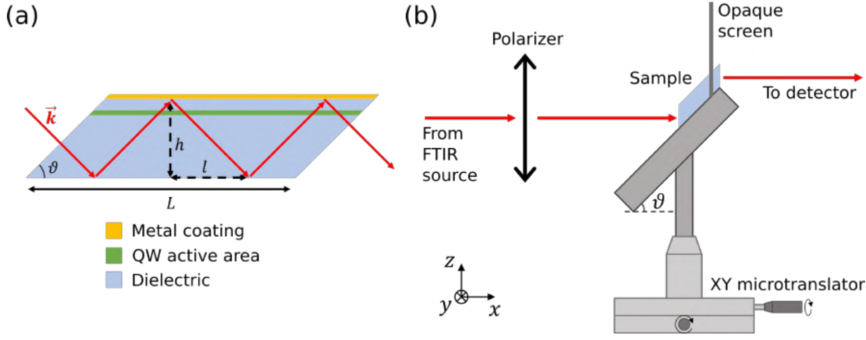

Figure 3.9 – (a) Geometry of the sample for multipass experiments. The lateral facets are lapped to an angle $\vartheta = 45°$. Polarized light injected into the sample of length L is internally reflected L/l times before exiting from the other facet. The surface close to the quantum wells (green slab) is covered with an Au film. (b) Schematics of the sample mount for a multipass transmission experiment. The sample is mounted on a stage tilted at an angle $\vartheta = 45°$ so that the lapped facets are perpendicular to the incoming ray. After multiple internal reflections, the light comes out of the sample and is collected at the detector. An opaque screen is mounted to minimize the detection of spurious light. The position of the stage can be manipulated on the $x - y$ plane with two micro-translators.

is α_0, the absorption signal measured in the multipass geometry is $A \propto N\alpha_0$.

In our setup, the prepared sample is mounted on a stage tilted at $\vartheta = 45°$ so that the lapped facets are perpendicular to the incoming light, as shown in Fig. 3.9b. The metallic surface is placed upwards, while the uncovered surface is in contact with the stage. An opaque screen is placed around the sample, leaving the facets exposed, so that only the light that passes through the sample is transmitted to the detector. The detected signal is maximised by moving the sample in the $x - y$ plane with two micro-translators. The polarization of the incoming light is controlled by a polarizer placed in the chamber before the sample. Thanks to this setup, it is possible to take independent measurements of the transmission in the two polarizations. Given an impinging intensity of the light $I^{in}_{TM,TE}$ for the TM and TE polarizations

respectively, it is possible to write the detected intensity $I^{out}_{TM,TE}$ as

$$I^{out}_{TM} = \eta_s I^{in}_{TM} 10^{-(\alpha_{bg}\lambda + N\alpha_0)} \quad (3.1)$$

$$I^{out}_{TE} = \eta_s I^{in}_{TE} 10^{-\alpha_{bg}\lambda} \quad (3.2)$$

where $0 < \eta_s < 1$ is a geometrical factor taking into account that only a fraction of the light from the FTIR source actually is injected in the structure, α_{bg} is the background absorbance per unit length coming, for example, from free-carriers or dielectric losses, and $\lambda = Nh/\sin(\vartheta)$ is the total distance travelled by the light beam inside the structure (see Fig. 3.9a). We use a uniformly polarized light, then $I^{in}_{TM} \sim I^{in}_{TE}$. Since only TM polarization can excite the ISB transitions, it is possible to reconstruct the absorption of the sample by extracting the logarithm of the ratio of the two equations. The resulting equation is

$$N\alpha_0 = -\log_{10}\left(\frac{I^{out}_{TM}}{I^{out}_{TE}}\right) \quad (3.3)$$

Thanks to the ratio, this method conveniently eliminates the dependency of the result on η_s, on the intensity of the impinging light, and on the background absorbance, effectively isolating the contribution of the QW.

Thanks to the enhanced absorption and the contrast provided by selecting the polarizations, multipass geometry is particularly suitable to precisely measure ISB transitions in samples with low absorbance, such as the single quantum wells we employ in our experiments.

We measured our samples both at room temperature and at 80 K. For the room-temperature measurements, we employed a custom sample mount equipped with two micrometric screws for precise alignment in the $x - y$ plane (sketched in Fig. 3.9b). We measured in vacuum and normalized each measurement to the transmission of the bare polarizer to mitigate the effect of the possible non-uniformity in the polarization of the FTIR source.

For the low-temperature measurements, we used a liquid nitrogen cryostat with a custom coldfinger tip which allowed the 45° angle mount. The presence of the cryostat introduces a few issues. First, since

the cryostat is larger than the Jasco sample chamber, we could not measure the ISB transition keeping the whole optical path in vacuum. Moreover, the presence of the cryostat ZnSe windows in the optical path and the more difficult alignment of the sample lowered the signal-to-noise ratio. We could partially mitigate this effect by increasing the number of accumulations per measurement.

3.2.2 Microscopy techniques

Far-field FTIR is suitable for measuring the reflection or transmission spectra of large samples, i.e., with active surfaces of the order of the millimeter. However, it is possible to couple the FTIR spectrometer to an infrared microscope for analyzing samples with micrometric lateral resolution. In this technique, called micro Fourier infrared spectroscopy (μFTIR), the light is focused on the sample through a Cassegrain objective, as shown in Fig. 3.10a. The Cassegrain objective is an optical component composed by two curved mirrors: the primary mirror (A

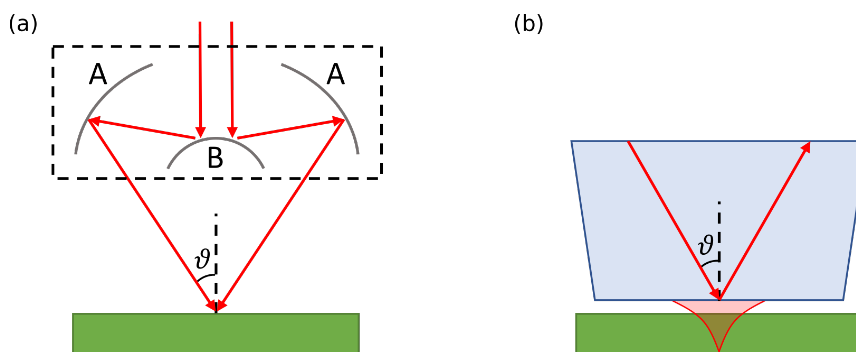

Figure 3.10 – (a) Schematics for the micro FTIR. The light is focused on the sample plane by a Cassegrain objective (enclosed in the black dashed square). It is a reflection focusing lens made up of a primary (A) and a secondary (B) mirrors. The light impinges on the sample at an angle $\vartheta \sim 30°$. (b) Schematics for the ATR-FTIR. Light is injected in a Ge crystal (blue trapezoid shape) with a sufficient angle ϑ to cause total internal reflection at its surface. At the reflection point, an evanescent field leaks out of the crystal (red shading). The reflected light retain information on the absorption spectrum of the sample that interacted with such evanescent field.

in Fig. 3.10a) is a circular concave mirror with a hole in the center that allow the passage of the beam. The secondary mirror (B) is a convex mirror with a smaller radius. The sample is put on a horizontal stage below the objective and the light is focused on the sample surface. Because of the particular shape of the optics, the light impinges with at an angle ϑ and no light comes for $\vartheta \sim 0°$ due to the shadow of the secondary mirror. This can have impact on the measurement on samples with dispersive features, i.e., features whose energy-momentum dispersion is not flat (for example, the angle-dependent reflection of the gratings, discussed in Sec. 2.1.4).
For our experiments, we employ a FT/IR 6600 coupled to a IRT 5200 microscope, by Jasco. The light is focused by a 16x Cassegrain at an angle $\vartheta \sim 35°$ on the sample and is collected by a MCT detector. In our experiment, the angle of incidence has a limited impact. Indeed, the momentum of graphene plasmons is much larger than the momentum of a free-space photon at the same energy. Thus, the angle-dependent contribution to the right-hand term of Eq. 2.9 is much smaller than the non-dispersive momentum given by the grating. On the other hand, surface plasmons excited on the grating have much smaller momentum and are therefore affected by the angle, as discussed in Sec. 4.2.3. The employed microscope is equipped with a motorized stage with piezoelectic crystals that allow automated movement with micrometric precision. Moreover, a CCD camera is coupled to the same optical path as the IR beam. Thanks to this and to the motorized stage, the measurements can be performed on areas chosen via software with micrometric lateral resolution. Thanks to the focalization of the objective, the micro FTIR can collect signal from areas with size as small as $\sim 20 \times 20$ μm. However, using the instrument at its resolution limit lowers the achievable S/N ratio thus hindering the measurement, especially if the expected signal has relatively low contrast, as in the presented case (see Sec. 4.1.2). To tackle this issue, we chose to analyze larger areas of at least 20×40 μm. Even so, a relevant signal measured on so small areas could only be obtained for very long accumulation times of ~ 9 hours. While improving the S/N, such long accumulation time causes the measurement to be more affected by environmental agents, such as

changes in air composition (for example, changes in the density of CO_2 or other organic compounds due to the presence of people in the room) or vibration that might occur. To reduce such effects, we chose to perform long accumulation measurements only during weekends or overnight.
Another issue of having such a small measurement area is presented during the alignment of the aperture on the sample. . To select the area to be measured, the sample is initially searched below the microscope with visible light. The wanted measurement area is then selected using such optical image. However, this process is hindered by possible small misalignment of the optical paths for visible and IR light in the microscope, which could cause a shift between the chosen measurement area and the actually measured area. We tested this by performing linescans along two perpendicular sides of a gold square fabricated on an IR-transparent GaAs substrate. We measured an error of ~ 10 μm in the x direction of the microscope stage, and a much lower error of < 1 μm in the y direction. We corrected this misalignment by modifying the position of the aperture accordingly before the measurement.
Another microscopy technique can be used in the micro-FTIR setup: attenuated total reflectance (ATR) [170]. In ATR-FTIR, light coming from the microscope is injected into a crystal with a large index of refraction n_c with an angle ϑ, as shown in Fig. 3.10b. If the crystal is brought into contact with a sample material with smaller index n_s, light impinging at the interface can undergo total internal reflection if the incident angle is larger than $\vartheta_{crit} = \arcsin(n_s/n_c)$. When the beam is totally reflected, an evanescent field propagates outside the crystal into the smaller index sample. The penetration depth depends of the wavelength λ of the impinging light and can be written as [170]

$$d_{p0} = \frac{\lambda}{2\pi\sqrt{n_c^2 \sin\vartheta - n_s^2}} \tag{3.4}$$

The penetration depth depends on the wavelength both by the explicit numerator, and by an implicit dependency of the index of refraction $n_s = n_s(\lambda)$. Thanks to the interaction of the evanescent field with the sample, the reflected beam carries information on its absorption

spectrum. For small absorption, the reflectivity is approximated as [171]:

$$R \sim e^{-\alpha d_e} \approx 1 - \alpha d_e \tag{3.5}$$

where α is the absorption coefficient of the sample and d_e is an effective thickness, i.e. the thickness of a film of the same material that would give the same absorption for transmittance at normal incidence [172]. The effective thickness d_e depends on the penetration depth d_{p0} [171]. Thus, absorption coefficients computed with Eq. 3.5 already contain the corrections to aberrations of the measured spectrum due to the wavelength dependency of d_{p0}.
ATR-FTIR measurements are very sensitive and can readily analyze the absorption of optically thick samples for which transmission experiments are impossible. Thanks to this, ATR-FTIR has become increasingly popular for chemical and composition analysis. Furthermore, since the evanescent field has a momenta distribution much wider than far-field light (as in the case of the near-field of a metallic tip, see Sec. 2.1.4), ATR geometry can be used to excite surface polaritons such as graphene plasmons [173].

3.3 Electrical measurements

Electrical measurements in semiconductors include a wide range of setups used to explore various properties of the electron gas inside the sample under examination [84]. In our work, we employ electrical measurements for exploring the electronic properties of several graphene-based devices in a FET geometry (see Sec. 2.1). We apply a potential between two electrodes on the graphene sheet (called source S and drain D, following the FET teminology) and we use back gate potentials to modify the carrier density in the channel. In this section, we describe the main details of the setups and methods we employed in our experiments. First, we describe how the electrical contact between the instrumentation and the samples is established. We then describe the different setups employed for measuring, with attention on what information we can extract from each measurement. At the end of the section, we list the instruments used in the experiments.

3.3.1 Wire-bonding the sample

To enable the measurements, it is necessary to electrically connect the fabricated samples to the instrumentation. To this end, the devices are put in suitable chip carriers which contact the micrometre-scale electrodes on the samples to macroscopic pads which can then be connected to the instrumentation. For our work, we employ two different types of carriers. The first is a commercial dual-in line (DIL) package with 24 pins, shown in Fig. 3.11a and used for measurements using a breakout box. The second type is a homemade carrier made with a copper bar as a conductive substrate on which we glue ceramic pads, shown in Fig. 3.11b. For both carrier types, the sample chip is put in electrical contact with the conductive substrate of the carrier by means of a silver conductive paste from RS Pro. To provide electrical contact between the sample and the carrier, the metallic contacts lithographed on the sample surface are wire bonded to the carrier pads with the wedge bonding method [174]. A schematics is shown in Fig. 3.12. An aluminum wire is threaded in a wedge tip. It is then pressed on a pad of the chip carrier and bonded to the metal with ultrasonic pressure. Likewise, a second bond is made on a contact on the sample. After the bonding, a clamp rips the wire, thus leaving the bonded wire on the sample. In our experiments, we need to build up a potential difference between the conductive substrate and the electrodes fabricated on top of the sample surface (a.e., for an efficient back gating). Thus, we need

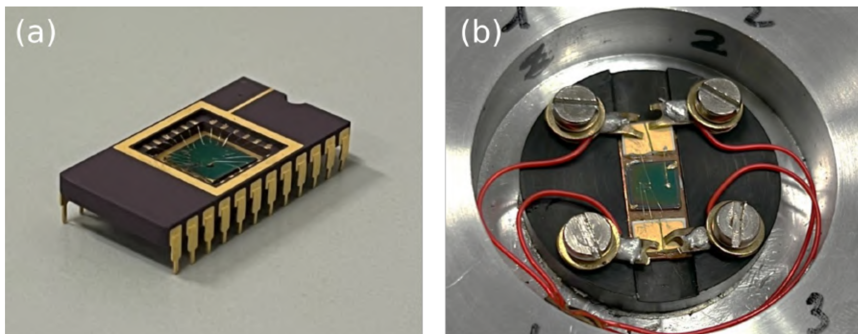

Figure 3.11 – (a) Commercial 24 pin DIL package. (b) Homemade chip carrier made of copper with ceramic pads, already mounted in a setup.

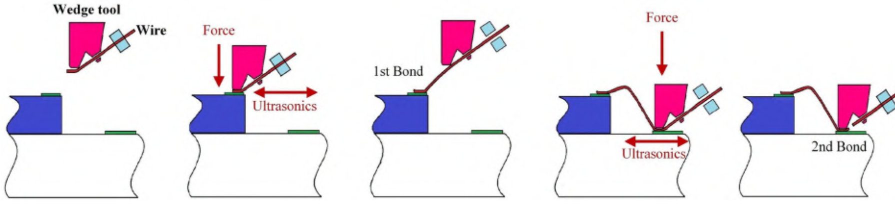

Figure 3.12 – Schematics for the wedge bonding exploiting ultrasonics. Taken from [174]

a bonding procedure that does not mechanically damage the sample, creating conductive channels in the dielectric which can hinder the buildup of the potential. Thanks to the ultrasounds, the tip pressure can be soft enough not to break the insulating dielectric, thus preserving the gating capability of the chosen substrate. Once bonded, the devices are ready to be measured in the chosen setup.

3.3.2 Electrical measurements on graphene FETs

In our work, we performed different types of electrical measurements. Here, we briefly discuss the main features of the measurements we performed on graphene FETs (gFETs). More detail on the specific measurements will be given during the discussion.

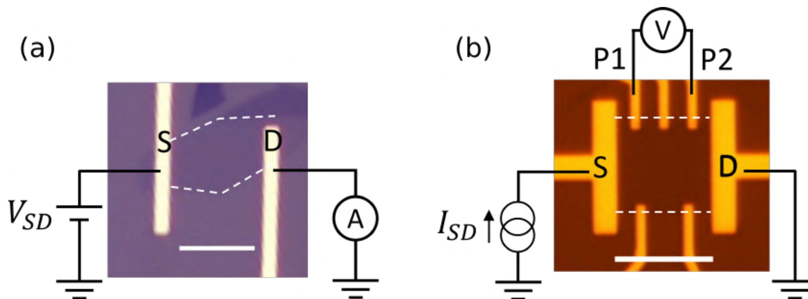

Figure 3.13 – (a) Schematics of the 2W measurement on a gFET. (b) Schematics of the 4W measurement on a gFET.

Two-wire (2W) measurement A potential difference V_{SD} is applied between the source and drain electrodes, as shown in Fig. 3.13a. S is connected to the high end of a voltage source, D is connected to

a grounded current monitor which measures the current I_{meas}. This measurement is straightforward as it is performed in series with the device and only requires two contacts. However, it is affected by the series resistance of S and D metallic contacts:

$$I_{meas} = \frac{V_{SD}}{R_S + R_{ch} + R_D} \tag{3.6}$$

where I_{meas} is the measured current, R_S, R_{ch} and R_D are the resistances of source, channel and drain respectively. In this kind of measurement, the tilt of the conduction band (i.e., the potential along the channel) is fixed by the external potential, while the flux of electrons in the channel (i.e., the current) is adjusted according to the resistance.

Four-wire (4W) measurement Two additional electrodes are necessary for this type of measurement, called probes (P1 and P2) and placed at the lateral edges of the channel, as shown in Fig. 3.13b. A current generator feeds a constant current I_{SD} to the sample from S to D, creating a voltage difference along the channel. This voltage difference is measured by connecting a multimeter between P1 and P2. Since this type of measurement is done in parallel to the channel, it is independent from contact resistances, as the flowing current is regulated externally:

$$V_{meas} = R_{ch} I_{SD} \tag{3.7}$$

where V_{meas} is the measured voltage and R_{ch} is the resistance that the current experiences between P1 and P2, regardless of the influence of the contacts. During our measurements, we vary the resistance of the sample with the gate. To ensure a stable current feed, independent from the measured resistance, we employ a voltage generators with a resistance $R_{sour} >> R_{ch}$ in series as a current generator. In this type of measurement, the flux of electrons in the channel (i.e., the current) is fixed by the external generator, and the resistance of the channel determines how much the band is tilted (i.e., how much is the potential drop along the channel). Therefore, 4W measurements probe the energy necessary to move the fixed flux of electrons in the channel.
Both measurements can be performed with continuous signals (DC) or

Model	Company	Usage	Feed
SR830 Lock-In	Stanford Research Systems	Source/Measuring	AC
SR570	Stanford Research Systems	Current amplifier	AC
2614B Source Meter	Keithley	Source/Measuring	DC
DAQ6510	Keithley	Measuring	DC
GS200	Yokogawa	Source	DC
DLPCA 200	Femto	Current amplifier	DC
DLPVA	Femto	Voltage amplifier	DC

Table 3.1 – List of instruments used in our experiments

with a slowly alternating signal (AC) to employ the lock-in technique. In the first method, the sample is fed with direct signals (either voltage or current) and there is no active noise suppression. Conversely, the lock-in technique is employed to reduce the noise in the measurements. The working principles are the following: the sample is fed with an AC bias at 17 Hz. We chose such a low frequency both to minimize the impact of frequency-dependent components in the sample (i.e., to measure in conditions as close as possible to DC) and not to pick up noise from the 50 Hz power line. The signal coming out of the sample is collected in phase with the AC reference of the instrument. Every resulting signal which is not oscillating at the frequency of the bias is suppressed, thus yielding a higher signal-to-noise (S/N) ratio with respect to the DC measurement.

We employ different instruments for the transport measurement, summarized in Tab. 3.1. All the instruments can be used for both 2W and 4W measurements. We performed measurements in air by placing the chip carrier in a homemade breakout box with 24 BNC connectors, shown in Fig. 3.14a. Each pin can be connected either to the ground or to the BNC thanks to individual switches. Samples involving the ionic liquid are sensitive to the surrounding environment. Thus, to minimize the interaction of the sample under examination with the atmosphere, we measured in high vacuum ($< 10^{-5}$ mbar) in a homemade chamber connected to the breakout box, shown in Fig. 3.14b. Moreover, we designed a vacuum chamber with a zinc selenide (ZnSe) window, capable of reaching a vacuum $< 10^{-3}$ mbar, shown in Fig. 3.14c. The

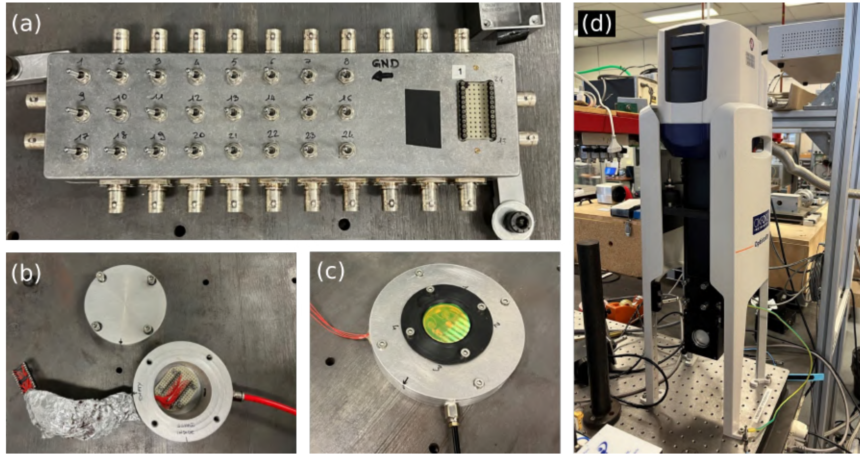

Figure 3.14 – (a) Homemade breakout box with 24 BNC connectors. On the right, the connection for the DIL package. (b) Homemade vacuum chamber with electrical connections for the DIL package. The chamber can be connected to the breakout box shown in (a). (c) Homemade vacuum chamber equipped with a ZnSe window to allow micro FTIR measurements. (d) The OptiStat Dry cryostat employed for low-temperature measurements.

chamber has four electrical contacts to ensure electrical connection to samples in vacuum and it was used to gate samples with ionic liquids while performing optical measurements with the microscope of the FTIR. Finally, we performed low-temperature measurements to study the transport properties of defect-engineered graphene FETs. To this end, we employed an OptiStat Dry cryostat by Oxford Instruments, shown in Fig. 3.14d. The system is cooled with a closed loop compressor capable of reaching a temperature < 3 K. The cryostat is also equipped with a Mercury iTC controller by Oxford Instruments which allows to set temperatures between 3 K and 300 K with an error of ~ 0.1 K. The electrical connection is granted by a PCIB wired to a breakout box with 24 BNC connectors, analogous to the one employed for in-air measurements.

Chapter 4

Towards Few-Electrons Strong Coupling

As discussed above, light-matter interactions in the few-electrons regime lead to strong quantum nonlinear effects, such as single-photon nonlinearities and photon-photon interactions. In general, reaching strong coupling is challenging because of the required small interaction volumes. Among the possible solutions, an outstanding approach is to exploit the enhanced light confinement offered by graphene PPs. Indeed, using graphene PPs as cavity modes yields a great increase in the energy density, and consequently in the coupling between the cavity and electronic modes. Another advantage of using PPs is the possibility to explore different regimes of coupling on the same device by exploiting the tunabiliy of the dispersion relation of plasmons. In this chapter, we investigate two possible structures to couple graphene plasmons coherently launched by a metallic grating with intersubband transitions in a shallow semiconductor single quantum well. First, we study the geometry by means of numerical simulations. We analyze the behaviour of the system as a function of different parameters such as QW and graphene doping, lattice pitch and graphene mobility. Then, we present the fabrication and experimental study of a similar structure.

4.1 Electrodynamic simulations

During our work, we used two different softwares for the electromagnetic simulations: the Radio-Frequency module of COMSOL Multiphysics, which exploits the Finite Element Methods (FEM), and the Periodically Patterned Multi Layer (PPML) script [175], which exploits the rigorous coupled wave analysis (RCWA) based on the scattering matrix algorithm. We used COMSOL for simulating 3D structures. However, the lateral characteristic lengths of the chosen structures (few μms) are much larger than the out-of-plane ones, with nanometric quantum wells and even monolayer graphene. Thus, the mesh required for the FEM in such structures has a large number of nodes, resulting in a large time consumption of the simulations. Conversely, PPML exploits the scattering matrix method to analyze a layered structure and does not need a mesh, thus yielding a much shorter simulation time. Since the structure we simulated are periodic, in both methods we design the unit cell and apply periodic boundary conditions to the edges of the cell. By comparing the results obtained by simulating the same geometry with the two methods, we concluded that the results are in very good agreement. Therefore, during the discussion we do not focus on the specifics of the simulation method.

4.1.1 Materials

The electromagnetic properties of the materials employed in the simulations are described by means of their dielectric permittivity. For non-active materials (air, QW barriers and dielectrics), we chose to employ a constant dielectric permittivity, as no resonant feature is present in the spectral range of interest.

Indium Arsenide (InAs) QW The optical response of QWs in the IR is dominated by the intersubband transitions. Thus, it is possible to write the dielectric function of an InAs QW with thickness L_{QW} and 2D carrier density n_{QW} by decoupling the in-plane (Drude-like) and

out-of-plane (resonant) response:

$$\varepsilon_{xy}^{QW}(\omega) = \varepsilon_{InAs}\left[1 - \frac{\omega_P^2}{\omega(\omega + i\gamma_{\|})}\right]$$
$$\varepsilon_{z}^{QW}(\omega) = \varepsilon_{InAs}\left[1 - f_0\frac{\omega_P^2}{\omega_{12}^2 - \omega^2 - 2i\omega\gamma_{12}}\right]^{-1}$$

where $\varepsilon_{InAs} = 11.8$ is InAs dielectric constant [176], $\omega_P = \sqrt{\frac{e^2 n_{QW}}{\varepsilon m^* L_{eff}}}$ is the plasma frequency of the 2D electron gas, $m^*/m_e = 0.0023$ being the effective mass of the electrons in the crystal in units of the free-electron mass [177], $\gamma_{\|} = 1/\tau_{\|} \sim 1$ THz, τ being the in-plane relaxation time [178], ω_{12} is the frequency of the ISB transition, and $\gamma_{12} \sim \omega_{12}/7$ is the ISB transition broadening, as can be estimated by linewidth measurements.

Graphene The dielectric function of graphene can be written as [6]:

$$\varepsilon_{gr} = 1 + \frac{i\sigma(\mathbf{q}, \omega)}{\varepsilon_0 \omega h}$$

where σ is graphene conductivity and $h = 0.34$ nm is the graphene thickness. We employ a local conductivity, computed with the Kubo formula in the random phase approximation (RPA) [179], which can be written as the sum of two components, accounting for intraband and interband contributions, respectively

$$\sigma_{gra}(\omega) = \sigma_{intra} + \sigma_{inter}$$
$$\sigma_{intra}(\omega) = 2i \cdot \frac{e^2 k_B T}{\pi\hbar^2(\omega + i\tau^{-1})} \ln\left[2\cosh\left(\frac{E_F}{2k_B T}\right)\right]$$
$$\sigma_{inter}(\omega) = \frac{e^2}{4\pi}\left\{\frac{1}{2} + \frac{1}{\pi}\arctan\left[\frac{\hbar(\omega + i\tau^{-1}) - 2E_F}{2k_B T}\right] - \right.$$
$$\left. - \frac{i}{2\pi}\ln\left[\frac{(\hbar(\omega + i\tau^{-1}) + 2E_F)^2}{(\hbar(\omega + i\tau^{-1}) - 2E_F)^2 + (2k_B T)^2}\right]\right\}$$

where k_B is the Boltzmann constant and T is the temperature of the system. The mobility μ of electrons in graphene is included in such

description through the term $\tau = \mu E_F / e v_F^2$, which is the relaxation time of electrons and takes into account dissipation. Due to the 2D nature of graphene, it would require a mesh with subnanometric nodes to be effectively described. However, we can mimic the presence of graphene by applying surface current boundary conditions to the geometrical surface the graphene lays onto [180]. In the simulation, a current flows on that surface following the formula $\mathbf{J_{gr}} = \sigma_{gra}(\omega)\mathbf{E_{in}}(\omega)$, where $\mathbf{E_{in}}(\omega)$ is the electric field impinging on the plane. Contrarily, the full 3D model can be employed in the PPML, as no mesh is required, and the thickness is just another parameter in the computation.

Hexagonal boron nitride (hBN) hBN is an hyperbolic material [181], meaning that it has in-plane and out-of-plane dielectric functions with opposite signs in two regions of the spectrum, called *reststrahlen bands*. We employ hBN as a dielectric spacer. Since it is a hyperbolic material, the out-of-plane and in-plane components of the dielectric function must be distinguished. Following [181], the two components can be written as:

$$\varepsilon_{hBN}^a = \varepsilon_\infty^a \left(1 + \frac{(\omega_{LO}^a)^2 - (\omega_{TO}^a)^2}{(\omega_{TO}^a)^2 - \omega^2 - i\omega\gamma^a}\right)$$

where $a = \{xy, z\}$ indicates the chosen direction (in-plane and out-of-plane, respectively), ω_{LO} and ω_{TO} are the frequencies of the longitudinal and transverse optical phonons in the chosen direction, ε_∞ is the high-frequency dielectric permittivity, and γ is the damping constant. Since no free-charge is present in hBN, it cannot be simulated as a current boundary condition as in the case of graphene. Thus, the presence of thin layers of hBN impose a finer mesh to observe local variations in the simulations.

Gold We employ a Drude-like model for the permittivity of gold:

$$\varepsilon_{Au} = 1 - \frac{\omega_P^2}{\omega(\omega - i\gamma_{Au})}$$

where $\omega_P = \sqrt{\frac{e^2 n_{Au}}{\varepsilon_0 m_e}} \approx 2180$ THz is the bulk plasma frequency and $\gamma_{Au} = 1/\tau_{Au} \approx 6.5$ THz, τ being the intraband relaxation time [182].

4.1.2 PPs launched by a metallic lattice

The first geometry we discuss is a platform to couple graphene PPs to ISB transitions in a single shallow quantum well (SQW). We will refer to this geometry as GP structure. A graphical depiction and the schematics for the simulations are shown in Fig. 4.1. The SQW is composed of an undoped InAs substrate, 6 nm of AlSb, 15 nm of n-doped InAs and a cap layer of 6 nm of AlSb. The ISB resonant frequency for such geometry is $\omega_0 = 28$ THz. Graphene is placed directly on top of this structure. The gold lattice is in contact with graphene and is made of ridges of thickness $t = 50$ nm and width w repeated with a pitch p. We define the filling fraction as $ff = w/p$, i.e. the fraction of layer filled with gold. We illuminate the structure with plane waves in the TM mode (**H** in-plane), impinging on the sample at an angle ϑ.

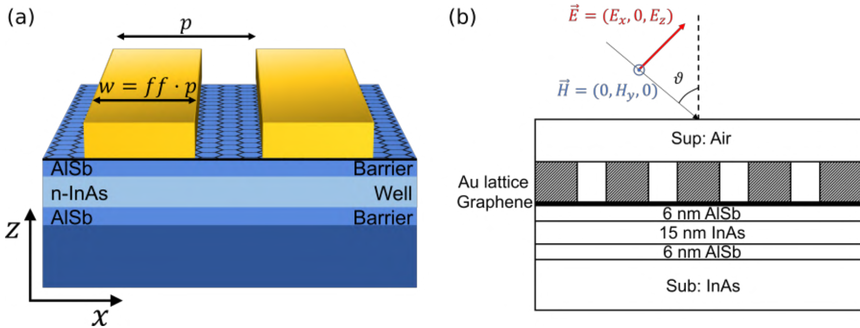

Figure 4.1 – (a) Three-dimensional schematics of the presented structure to couple PPs to ISB transitions in a single quantum well. The lattice has a pitch p and each ridge has a width w. (b) Geometrical schematics of the GP structure used in the simulations.

We first studied the dependency on the pitch of the plasmonic resonance in graphene without the influence of the quantum well. To this end, we set $n_{QW} = 0$ cm^{-2} to remove the ISB absorption. Fig. 4.2a shows the simulated reflectance of the GP structure for different values of p with fixed $ff = 0.7$. The Fermi energy of graphene is $E_F = 500$

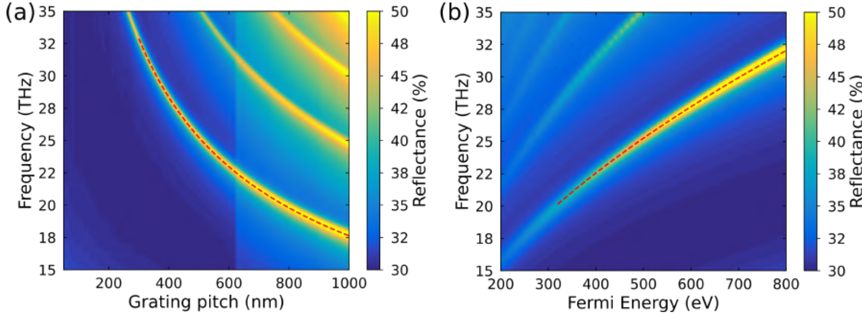

Figure 4.2 – (a) Reflectance of the GP structure with $E_F = 500$ meV and $ff = 0.7$ as a function of the grating pitch p. The dispersion of the plasmonic mode is visible as a peak in reflectance. Modes higher than the main are also visible. The red dashed line represents the result of a fit of the maxima of the curve with Eq. 4.1. The extracted parameters are $a = 632\ \mathrm{THz} \cdot \mathrm{nm}^{-\mathrm{b}}$ and $b \approx 0.51$. (b) Reflectance of the GP structure with pitch $p = 500$ nm and filling fraction $ff = 0.7$ as a function of E_F in graphene when the doping of the QW is $n_{QW} = 0\ \mathrm{cm}^{-2}$. The dispersion of the plasmonic mode is visible as a peak in reflectance. Higher order modes are also visible.

meV. The reflectance peaks are the optical response of plasmons in graphene. The lowest resonance is the main mode, but higher modes are also visible. The plasmonic resonance varies with the pitch ideally as $\omega_p \propto \sqrt{1/p}$. Indeed, the array gives a momentum in multiples of $\kappa = 2\pi/p$ to the incoming light, resulting in $\omega_p \propto \sqrt{\kappa}$ (see Eq. 2.8). To test the dependency, we extracted the maxima of the main mode as a function of the pitch and fitted the resulting curve with the function

$$\omega_{max}(x) = a \cdot x^b \tag{4.1}$$

In this case, $x \equiv p$. The resulting curve is shown in Fig 4.2a as a red dashed line superimposed to the main mode. The obtained parameters are $a = 632\ \mathrm{THz} \cdot \mathrm{nm}^{-\mathrm{b}}$ and $b = -0.51$. As a final remark, we note that metal gratings can sustain surface plasmons polaritons (SPPs) which are not related to the presence of graphene [69]. However, the momentum of SPPs is much smaller than the one of PPs [183]. Thus, the optical collective excitation of the grating has much higher frequencies and does not impact the system in the selected frequency range. Indeed,

the wavelength of the SPP launched by a lattice of pitch p sitting on a dielectric with index of refraction n is $\lambda_{SPP} \propto p \cdot n_{sub}$ [69]. By using $n_{sub} \sim 3.5$ and $p = 500$ nm, the obtained SPP wavelength is $\lambda_{SPP} \sim 1.85$ μm $\simeq 160$ THz, distant from the region of interest.
Another important parameter of the simulation is the Fermi energy inside graphene. Fig. 4.2b shows the reflectance of the GP structure with pitch $p = 500$ nm and $ff = 0.7$ and no ISB resonance ($n_{QW} = 0$ cm^{-2}). As in the previous case, the dispersion is visible as a peak in the signal. With the selected pitch value, the dispersion relation of PPs in graphene can be effectively tuned from 18 THz to 32 THz, thus crossing the QW frequency. As discussed in Sec. 2.1.4, the plasmonic dispersion relation is $\omega_p \propto \sqrt{E_F}$. We used the same Eq. 4.1 ($x \equiv E_F$ this time) to fit the maxima of the curve (red dashed line in Fig 4.2b) and obtained $a = 35.9$ THz $\cdot$ eV$^{-\text{b}}$ and $b = 0.50$. The change in the observed dispersion relation with the Fermi energy is a clear signature that the metallic lattice can launch graphene PPs in the chosen geometry.
To study the interaction of graphene PPs with ISB transitions in the

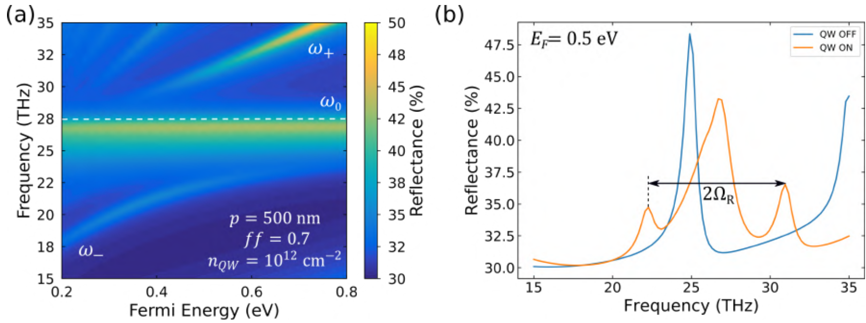

Figure 4.3 – (a) Reflectance of the same GP structure when $n_{QW} = 10^{12}$ cm^{-2}. The plasmonic mode strongly interacts with the QW resonance at frequency $\omega_0 = 28$ THz and divides into lower (ω_-) and upper (ω_+) polariton branches. The uncoupled resonance at frequency ω_0 is still visible due to the interaction of the ridges with the QW. (b) Comparison of two reflectance curves extracted from Fig 4.2b and from (a) for $E_F = 0.5$ eV. When the QW is OFF (blue line), the reflectance shows one sharp peak associated to the PP excitation. When the QW is ON (orange line), three peaks are visible: the upper and lower polariton branches and one peak at ω_0. The distance between the two polaritonic branches (black double-headed arrow) is $2\Omega_R \sim 10$ THz.

QW, we now turn on the ISB absorption by putting $n_{QW} = 10^{12}$ cm^{-2}. Fig. 4.3a shows the simulated reflectance of the GP structure for $p = 500$ nm and $ff = 0.7$. The first noticeable feature is the modification of the plasmonic dispersion relation: in fact, it divides into a lower (ω_-) and an upper (ω_+) polaritonic branch around the QW resonance ω_0. The so-called *avoided crossing* is a signature of the strong coupling regime that establishes between graphene PPs and the ISB resonance. The coupling can be tuned by changing E_F, and the minimum distance between the two branches is $2\Omega_r = 10$ THz. Such a Rabi frequency results in a coupling constant of $g \sim 0.18$. The uncoupled ISB resonance is still visible at frequency ω_0. We attribute this to the excitation of ISB transitions by modes supported by the metal ridges, and possibly to residual coupling to higher order plasmonic modes.

To more deeply understand the interaction, we study the electric field distribution in the GP structure when strongly coupled. To this end, we computed the modulus of the out-of-plane component of the electric field $|E_z|(x, z)$ in the structure for $E_F = 0.5$ eV at three different frequencies, as shown in Fig. 4.4a-c. In the lower polariton branch ($\omega_- = 23$ THz, Fig. 4.4a) and in the upper polariton branch ($\omega_+ = 31$ THz, Fig. 4.4b), the electric field is oscillating in the x direction between the ridges and propagates in both graphene ($Z_{gr} = 200$ nm) and the QW ($Z_{QW} = 179 - 194$ nm), thus confirming that the observed mode is a PP-ISB mixed mode. Since the electric field is mostly between the ridges with some propagation below the ridge in the QW, the effective length involved in the resonances coupling can be roughly estimated with the interdistance between the ridges: $L \sim [p \cdot (1 - ff)] = 150 \times 10^{-8}$ cm. By considering the chosen density of charge carriers in the QW and a 2D structure of orthogonal stripes, we obtain that the number of electrons involved in the strong coupling is $N_{GP} \sim n_{QW} \cdot L^2 \approx 2.25 \times 10^2$.
Conversely, the electric field at $\omega_0 = 28$ THz (Fig. 4.4c) is mostly confined in the QW, below the edge of the ridge. This confirms that the residual uncoupled mode is excited by the metallic lattice. In fact, light scattered from the sharp features of the metallic grating has an out-of-plane near-field component which cannot be completely screened by the electrons in graphene. Therefore, E_z leaks in the QW and excites

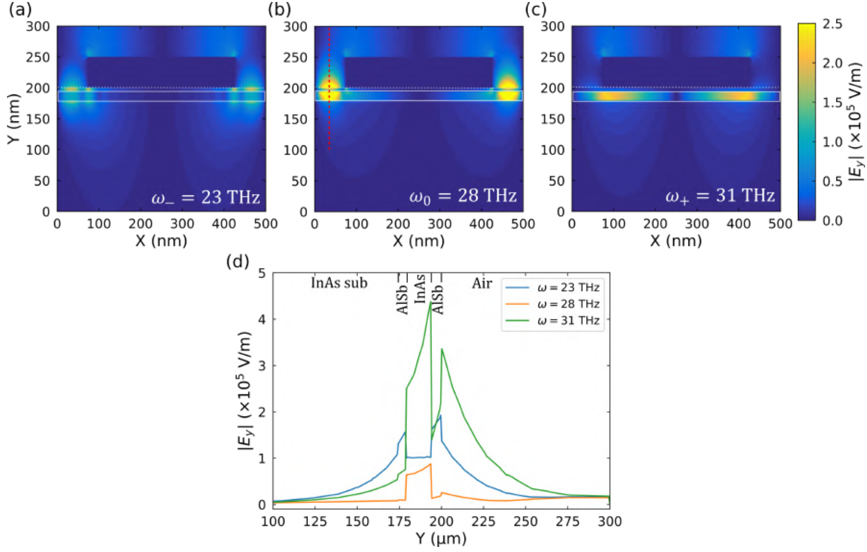

Figure 4.4 – (a-c) Modulus of the z-component of the electric field of the GP structure with $p = 500$ nm, $ff = 0.7$ and $E_F = 0.5$ eV for three different excitation frequencies: lower polariton branch $\omega_- = 23$ THz (a), upper polariton branch $\omega_+ = 31$ THz (b) and uncoupled excitation $\omega_0 = 28$ THz (c). The graphene plane is indicated with a white dashed line and the QW active area is enclosed in a white solid rectangle. (d) Lines extracted from (a), (b) and (c) for $x = 50$ nm (red vertical dashed line in (b)). The different layers of the structure are reported on the upper horizontal axis.

the ISB transition. Fig. 4.4d shows the comparison of the profiles of $|E_z|$ along the z axis for $x = 50$ nm for the three chosen frequencies. Polaritons in the lower branch (blue line) have fields confined in the semiconductor around the QW, with a maximum at Z_{gr}. Polaritons in the upper branch (green line) confine the energy mostly in the QW active layer, with also a strong component leaking in air. Finally, the uncoupled mode shows a strong confinement of light in the QW layer, with much lower intensity with respect to the other two excitations.

The presented structure can sustain mixed modes coupling polaritons to the intersubband excitation inside a QW. However, the relative contrast of the polaritonic excitation is around 5% (see Fig. 4.3b). To further enhance the contrast, it is possible to insert a metallic layer below the InAs substrate, as shown in Fig. 4.5a. The resulting

structure is the same GP structure embedded in a metal-insulator-metal (MIM) cavity. The reflectance of this structure depends on the distance between the lattice and the metallic substrate (i.e., the cavity thickness t_{cav}), as shown in Fig 4.5b. When the cavity is much thinner than the wavelength of light in the semiconductor ($t_{cav} \ll \lambda_0/n_{sub}$, where λ_0 is the wavelength of light in vacuum and n_{sub} is the substrate refractive index), very little energy can accumulate in the cavity, dramatically reducing the contrast of the modes.

When the thickness is increased, also the energy inside the cavity increases, until it reaches the condition of nearly perfect absorption for $t_{cav} \sim 0.7$ μm. This condition happens when the thickness of the cavity is

$$t_{cav}^{cc} = \frac{\lambda_0}{4n} \tag{4.2}$$

If we consider a frequency of $\lambda_0 \sim 10$ μm (corresponding to $\omega = 30$ THz) and a refractive index of the substrate $n_{sub} \sim 3.4$, we obtain $t_{cav}^{cc} \sim 0.73$ μm.

Thus, we presented a structure in which graphene plasmons excited by a metal lattice strongly couple with electronic transitions in an InAs QW. The coupling strength can be varied in the same device by tuning E_F in graphene. The coupling constant can reach a value as high as $g \sim 0.18$ for $E_F = 500$ meV.

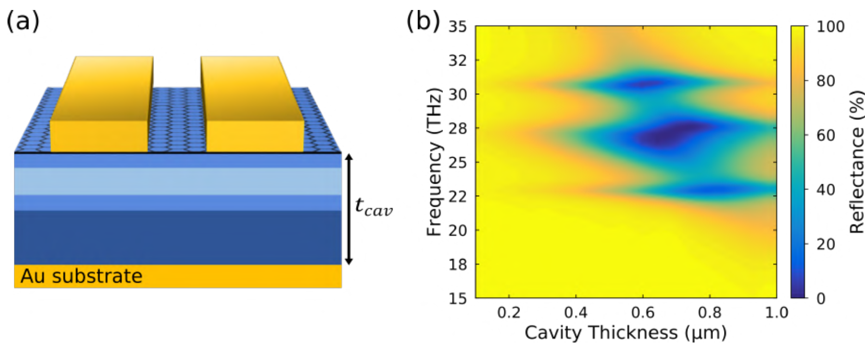

Figure 4.5 – (a) Schematics of the GP structure embedded in a metal cavity of thickness t_{cav}. (b) Simulated reflectance for the structure depicted in (a) as a function of the cavity thickness t_{cav}.

4.1.3 AGPs below a metallic nanocube

As discussed in Sec. 2.1.4, when graphene is placed close to a metal, the plasmonic mode flattens towards the Fermi velocity line, resulting in an increased confinement of light. Consequently, we designed a second structure, referred to as AGP structure, in which the enhanced confinement is exploited to reach the strong coupling regime with a reduced number of electrons in the QW. A graphical depiction of the AGP structure is shown in Fig. 4.6a. In this geometry, a hBN dielectric spacer of thickness $t_{hBN} = 2$ nm is placed on top of a single QW with an ISB transition at $\omega_0 = 30$ THz. AGPs are excited in graphene by nanocubes of side length $l = 30$ nm. The structure is illuminated with plane waves in the TM mode as in the previous case. Since AGPs are metal-graphene cavity modes, we simulated structures with pitch $p = 1$ μm so that each nanocube can be treated as an independent cavity.

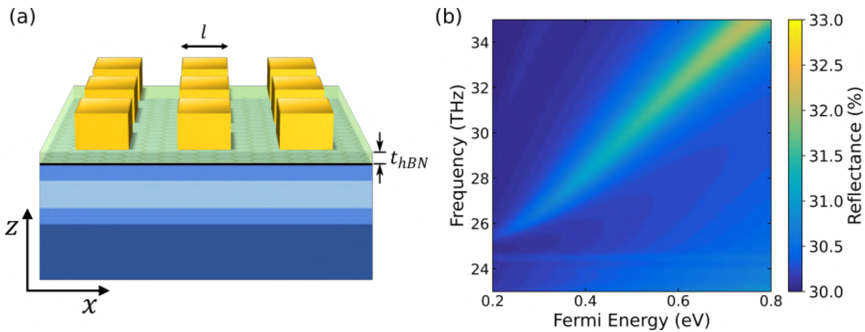

Figure 4.6 – (a) Three-dimensional schematics of the presented AGP structure. A dielectric spacer of thickness $t_{hBN} = 2$ nm is placed on top of the same substrate as in the GP structure. The AGPs are excited below nanocubes of side length $l = 30$ nm. (b) Simulated reflectance for the AGP structure with $n_{QW} = 0$ cm^{-2}. The plasmonic dispersion relation is shown as a peak in reflectance. The horizontal line at $\omega_{hBN} \sim 24.5$ THz is the upper limit of the first reststrahlen band of hBN [181].

To study the AGP excitations in this structure, we first turn off the QW absorption by putting $n_{QW} = 0$ cm^{-2}. Fig. 4.6b shows the reflectance of the simulated structure for different values of the Fermi energy inside graphene. The dispersion relation of AGPs is visible as a peak in

reflectance. As expected, the dispersion is flatter with respect to the dispersion of PPs. The deformation visible in the lower part (around $\omega \sim 26$ THz) is due to the coupling of PPS with the phonons in hBN [73]. The line visible at $\omega_{hBN} \sim 24.5$ THz is in fact due to the optical phonon in the crystal which absorbs light and influences the system (see Sec. 4.1.1). The contrast of the plasmonic branches is lower with respect to the GP structure. Two concurring causes can be addressed to explain this lowered contrast: first, the metal is farther from graphene, and the intensity of the electromagnetic field effectively influencing graphene is lower. Second, the active area is much smaller than the simulated cell because of the chosen values of l and p.

When the QW absorption is increased by putting $n_{QW} = 10^{12}$ cm^{-2}, the interaction with the ISB transition produces two separate polaritonic branches $\omega_{\pm}$ (see Fig. 4.7a), showing strong coupling behaviour as in the case of the GP structure. The minimum distance between the two modes is $2\Omega_R = 6.3$ THz (see Fig. 4.7b), resulting in a coupling constant $g \sim 0.11$. Differently from the GP structure, in this geometry the uncoupled mode at frequency ω_0 is not excited by the metal edges thanks to the increased distance between the metal and the QW active area.

It is worth noting that in the AGP structure the electric field is confined below the nanocube [36], as shown in Fig. 4.8a, in an area $A_{AGP} \sim l^2 = 9 \times 10^{-12}$ cm^2. Considering the chosen density of charge carriers in the QW, the computed number of electrons involved in the

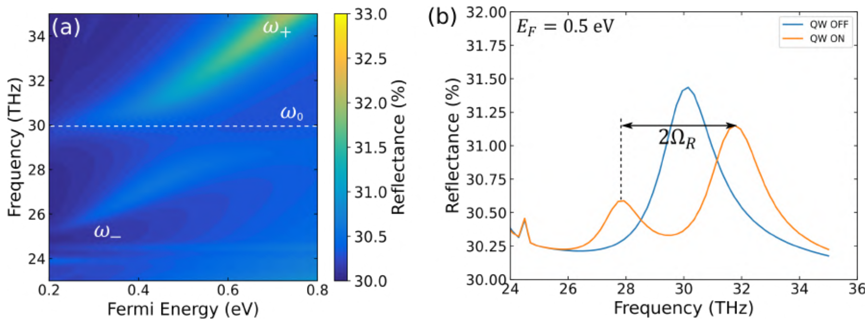

Figure 4.7 – (a) Simulated reflectance for the AGP structure with $n_{QW} = 10^{12}$ cm^{-2}.

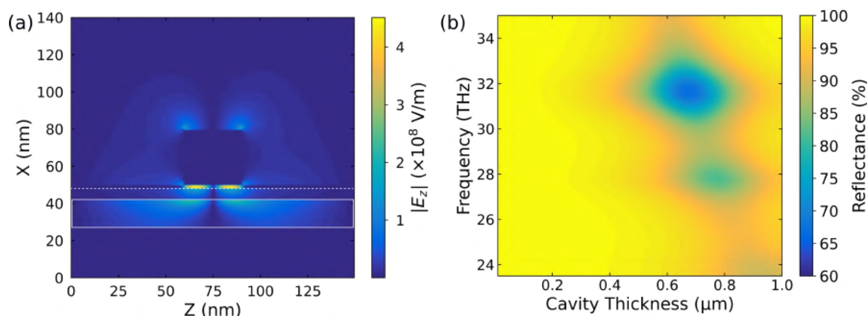

Figure 4.8 – (a) Absolute value of the out-of-plane component of the electric field $|E_z|(x, z)$ for $\omega = 31$ THz and $E_F = 0.5$ eV. The graphene plane is indicated with a white dashed line, the QW active area is enclosed in a white solid rectangle. (b) Simulated reflectance for the AGP structure with a metallic substrate as a function of the cavity thickness.

coupling for the AGP structure is $N_{AGP} \approx 10$. Such a remarkably low N_{AGP} demonstrates that the AGP structure is capable of reaching the strong coupling regime involving only few electrons of the QW. As a consequence, the presented structure is a suitable platform for studying the effects of the breakdown of the Hopfield model in the description of light-matter interactions.

As for the GP structure, by adding a metallic substrate in the AGP structure it is possible to create a metal-insulator-metal cavity that increases the absorbance of the system. Fig 4.8 shows the simulated reflectance of the AGP structure with a metallic substrate as a function of the thickness of the cavity. The contrast of the peaks is increased from $< 1\%$ for the geometry without metal (see Fig. 4.7b) up to $\sim 40\%$ for $t_{cav} \sim 0.7$ μm.

4.2 Experimental study of GP structure

Based on the achieved results of the simulations, we realize the GP structure for experimental investigations. We employed as substrate a InAs/AlSb heterostructure grown via molecular beam epitaxy (MBE) in the group of Alexei Baranov and Roland Teissier at Université de Montpellier. The growth sheet of the heterostructure is reported in Tab.

4.1. We will refer to this heterostructure as SQW-A. We chose a single

Material	Thickness (nm)	Doping (cm^{-3})
$In_{0.77}Al_{0.23}As$	3	–
AlSb	3	–
InAs	15	6.6×10^{17}(Si)
AlSb	5	–
InAs⋆	2	–
AlSb⋆	2	–
InAs(buffer)	100	$\sim 10^{16}$
InAs	Substrate	2×10^{16}

Table 4.1 – Growth sheet of the SQW from top (first line) to bottom (last line). The lines marked with ⋆ are repeated 50 times to create a 200 nm-thick layer. If the doping is heterogeneous, the donor material is indicated.

SQW made of InAs with AlSb barriers because the alignment of the bands creates quantum wells with height $V_0 = 1.3$ eV [184] that can be built close to the crystal surface (i.e., shallow QW). Moreover, the 3 nm $In_{0.77}Al_{0.23}As$ cap layer placed on top of the structure matches the Fermi level pinning at the surface with the Fermi level in the bulk of the crystal [185]. An unmatched Fermi pinning results in the creation of a charge layer at the surface of the crystal, which could hinder the QW optical properties and must therefore be avoided. Thanks to the chosen materials and the cap layer, the active layer of the QW is placed only 6 nm away from the surface, to allow for an efficient coupling with the electric field of the PPs. The QW is 15 nm thick and doped with Si donors with a density $n = 6.6 \times 10^{17}$ cm^{-3}, corresponding to a sheet density of $n_{QW} \sim 10^{12}$ cm^{-2} inside the QW. Below the QW, a repetition of 2 nm thick undoped InAs/AlSb layers is grown to decouple the lattices of the InAs substrate and the SQW. This is necessary because the lattice mismatch between InAs and AlSb [186] would otherwise introduce lattice deformations in the heterostructure. The resonant frequency of such structure was computed by solving the Schroedinger-Poisson equations with a custom software and is expected to be $\nu_{12} = 28.3$ THz, corresponding to a wavenumber of ~ 940 cm^{-1}. A second heterostructure was grown, called SQW-B. The difference

with SQW-A is the thickness of the active area of the QW, which is 10.1 nm for SQW-B. The Si doping is 10^{18} cm^{-3}, which yield a sheet doping of $n_{QW} \sim 10^{12}$ cm^{-2}, equivalent to SQW-A. The resonant frequency of SQW-B is expected to be $\nu_{12}^{B} = 45.7$ THz $\equiv 1524$ cm^{-1}. We use this substrate as a non-resonant reference.
To fabricate the GP structure, we employ high-quality graphene crystal grown by seeded CVD by the group of Camilla Coletti (see Sec. 3.1.5). The graphene was transferred on the heterostructure with the contamination-free semi-dry transfer method, which preserves the high quality of the crystal.

4.2.1 Multipass measurements: retrieving the ISB transition

Before starting the fabrication of the GP structure, we performed a preliminar study of the ISB transition in the QW with multipass measurements. For such measurements, we employed a chip of SQW-A without graphene on top. The chip was ~ 1 mm thick and ~ 6 mm long, resulting in a number $N = 6$ passages of the light in the SQW (see Sec. 3.2.1). As described in Sec. 3.2.1, we collect the transmission values $I_{TM,TE}$ for both TM and TE polarization in vacuum at room temperature ($T = 300$ K), and reconstruct the absorbance of the QW as $A = -\log(I_{TM}/I_{TE})$. The resulting curve is shown in Fig 4.9a. The spectrum shows two peaks, one with a position $\kappa_{12}^{m} = 960$ cm^{-1}, corresponding to a frequency of $\nu_{12}^{m} \sim 28.8$ THz, and a second with position $\kappa_{23}^{m} = 1183$ cm^{-1}$\equiv 35.5$ THz. The presence of the second peak is due to the excitation of the ISB transition between level 2 and level 3 of the QW. Indeed, the $2 \rightarrow 3$ transition frequency computed with the Schroedinger-Poisson equations is $\nu_{23} = 36$ THz $\equiv 1200$ cm^{-1}. The non-flat baseline observed for low frequencies is due to the Drude-like free-carrier absorption.
We fitted the two peaks with Lorentzian curves to gain information on the transitions. The results are shown in Fig. 4.9a, superimposed on the data for both the $1 \rightarrow 2$ (orange curve) and $2 \rightarrow 3$ (green curve) transitions. The fitting parameters are reported in Tab. 4.2. The

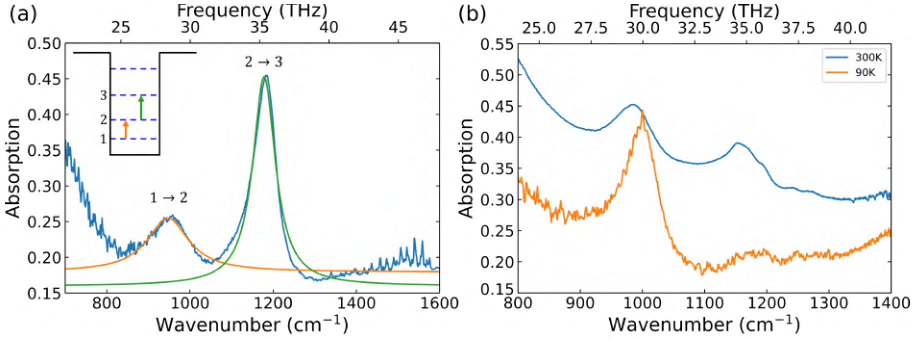

Figure 4.9 – (a) Absorption of SQW-A computed from the multipass measurements. Lorentzian fits of the two peaks are superimposed to the data. In the inset, a schematics of the excited ISB transitions inside the measured QW. (b) Absorption of SQW-A computed by measuring the same sample as in (a) in a cryostat at two different temperatures: 300 K (blue curve) and 90 K (orange curve).

central frequencies estimated with the fit are slightly red-shifted with respect to the original data, mostly due to the non-constant baseline. However, with the numbers extracted from the fit, it is possible to estimate the quality factor $Q_x = \kappa_x/\Delta\kappa_x$ for the transitions, which are $Q_{12} = 7.9$ and $Q_{23} = 17.8$ for the $1 \to 2$ and $2 \to 3$ transitions respectively. To understand why such a spectrum is observed at room

Transition	Offset	I	κ (cm^{-1})	$\Delta\kappa$ (cm^{-1})	Q
$1 \to 2$	0.18	0.08	947(960)	120	7.9
$2 \to 3$	0.16	0.29	1178(1183)	66	17.8

Table 4.2 – Parameters computed by fitting the peaks in Fig. 4.9 with a Lorentzian with a constant offset. The position of the local maxima measured on the peak is reported in parentheses close to the fit value.

temperature, we need to consider the Fermi energy inside the crystal. Indeed, the second transition is visible due to the high doping inside the QW. For the presented case, ($m^* = 0.023 m_e$, $n_{QW} = 10^{12}$ cm^{-2}), the computed Fermi energy is $E_F - E_1 = 25$ THz above the bottom of the first subband [187]. Considering that the thermal energy at 300 K is $k_B T \sim 6$ THz, then also the second subband is thermally populated and the electrons can get excited to the third subband by

absorbing photons. The observed intensity is higher because the dipole is larger for $2 \rightarrow 3$ transitions than for $1 \rightarrow 2$ transitions. In addition, the electrons at the bottom of the first subband cannot absorb light because the upper state is already occupied in the second subband. This effect also impacts the linewidth of the transitions: the electrons in the first subband can only absorb if their upper state is free, i.e. for momenta k away from 0. The observed transition is therefore more affected by the non-parabolicity of the subbands [187], which results in a broadening of the measured linewidth. Conversely, the second subband is only thermally populated at its bottom, and the ISB transition is less affected by the non-parabolicity of the bands for high k.
To confirm these findings, we performed the same measurement by putting a second sample in a cryostat cooled with liquid nitrogen. Fig. 4.9b show the comparison between two absorption spectra computed from measurements at room temperature ($T = 300$ K, blue line) and at $T = 90$ K (orange line). The spectra collected at 300 K is slightly different from the one shown in Fig. 4.9a, possibly because the sample is not the same or because of the presence of the cryostat (see Sec. 3.2.1). As expected, the $2 \rightarrow 3$ ISB transition is quenched at low temperature, as a result of the diminished thermal population in the second subband ($k_B T \sim 2$ THz for $T = 90$ K). Contrarily, the $1 \rightarrow 2$ ISB transition has a more intense absorption, and a reduced linewidth, with a quality factor at 90 K of $Q_{12}(90\text{ K}) \sim 18$. In addition, the transition is blue shifted to $\kappa_{12}^m(90\text{ K}) \sim 980\text{ cm}^{-1}$ as an effect of the diminished impact of the non-parabolicity.
In this section, we demonstrated the resonant absorption at the chosen frequency of $\nu_{12}^m = 960\text{ cm}^{-1}$, coming from the ISB transition in a single SQW by multipass measurements. We now focus on the optimization of the lithographic process for building a metallic array with the features studied in our simulations.

4.2.2 Fabrication of the metal lattice

To successfully measure the coupling between ISB transition in the QW and graphene PPs, the metal lattice must be placed on top of the structure in an area of at least 150 μm^2 to enable micro-FTIR

measurements with high enough S/N (see Sec. 3.2.2)
We now show the fabrication process of the lattice by means of EBL with electrons at 20 keV of energy. We chose such irradiation energy because it grants high achievable spatial resolution with low exposure time, which is useful to preserve the graphene lattice from damages induced by the e-beam (see Sec. 2.3.2).
As explained in Sec. 3.1.1, there are two critical steps in the EBL process: the actual exposition of the polymer-coated sample under the electron beam and the lift-off of the metal-coated masked structure. To optimize the first step, it is necessary to choose the correct irradiation dose to create a sharp mask with features of $\sim$ 150 nm. When exposing densely packed patterns like in the presented case, the possible impact of the so-called *proximity effect* [188] must be taken into account. The proximity effect is the non-uniform distribution of the dose effectively delivered during a uniform exposure of finely detailed structures. This non-uniformity is due to the electrons backscattered by the substrate, which create secondary electrons (SE) with energy sufficient to affect the resist. Because of this, closely-packed elements (i.e., the central elements in the pattern) receive a dose effectively higher than the isolated ones (i.e., the lateral elements of the pattern). The higher effective dose results in an overexposure of the resist, with detrimental effects on the quality of the patterns. To counter this issue in our structures, we chose to draw CADs with slightly lower filling fractions than the desired one (in our case, 0.7 from the simulations). This method has the additional advantage that a slight overexposure yields a higher resulting filling fraction, thus closer to the desired value. We first tested the fabrication on the same Si/SiO_2 substrate used for graphene exfoliation (see Sec. 3.1.3). We used such substrate to perform preliminary checks and isolate possible fabrication issues on a widely available commercial substrate before using the actual heterostructure. We used EBL recipe 2 (see Tab. A.1 in Appendix A) and lithographed 5 copies of the same CAD: a 20×50 μm^2 array with pitch 500 nm and $ff = 0.6$. Each copy was lithographed with increasing delivered electron dose D, from 190 $\mu C/cm^2$ to 230 $\mu C/cm^2$ (dose array). After the lithography, 5 nm of titanium and 40 nm of gold were deposited via thermal evaporation

on the sample. We left the sample in acetone overnight, to help the solvent seep in the fine details of the polymeric mask, and then finished the liftoff procedure with the standard cleaning procedure. We then observed the the final structure at the SEM to analyze the resulting dimensions of the metal lattice. The best result, shown in Fig. 4.10a, was obtained for $D = 200\ \mu\text{C/cm}^2$. The array has a measured pitch $p = 504.3$ nm, as shown in Fig. 4.10b. The distance between the ridges is $d \sim 177$ nm, resulting in a filling fraction $ff = 0.66$. The ridges have uniform dimensions over all the structure and form a regular lattice with sharp edges, as desired.

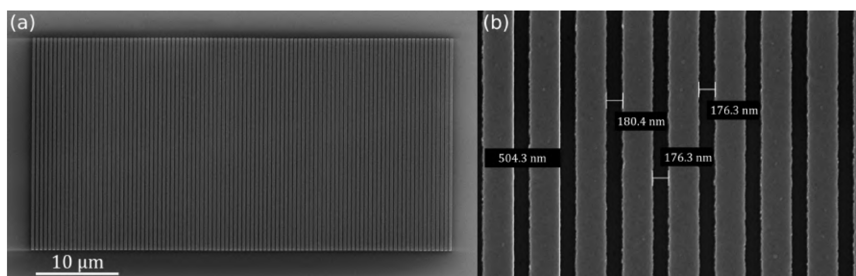

Figure 4.10 – (a) SEM image of the pattern fabricated on SiO_2 with recipe 2 in Tab. A.1 with a dose $D = 200\ \mu\text{C/cm}^2$. (b) Detail of (a). The obtained pitch is shown, along with different measurements of the spacing between the single ridges.

After testing the feasibility of the fabrication on Si/SiO_2, we move to the fabrication on the final substrate, the InAs/AlSb SQW. As discussed above, the substrate strongly impacts the result because of the proximity effect. The intensity and number of backscattered electrons, and hence the intensity of the proximity effect, depend on the properties of the substrate. For example, if the substrate is strongly insulating, the impinging charge accumulates at the irradiated spot because it cannot flow towards the grounded stage of the instrument (charging effect, [189, 190]). The accumulated charge creates a local increase of the electric field, which can backscatter the electrons more efficiently, resulting in a strong proximity effect and in distorted patterns. A similar effect is expected if a charged layer is already present in the irradiated structure, as in the case of the single SQW we are presenting. Indeed, the charged layer can backscatter electrons, with detrimental effects

on the patterned structures. For this reason, we performed a new dose array lithography with lower doses, ranging from $D = 170\ \mu\text{C/cm}^2$ to $D = 210\ \mu\text{C/cm}^2$. The evaporation and lift-off procedures are the same as described above. The same dose used for the optimized structure on Si/SiO_2 ($D = 200\ \mu\text{C/cm}^2$) yields an overexposed pattern, as shown in Fig. 4.11a. The proximity effect is clearly visible: the lateral part of the ridges show less distortion, with an interdistance between the ridges of ~ 175 nm comparable to the one achieved in Fig. 4.10. Moving towards the central region of the pattern, the width of the single ridge increases, and the interdistance becomes ~ 120 nm. Moreover, the lateral edges of the details in the patterned polymeric mask are not sharp vertical walls, but rather smeared slopes that do not provide a net division between the metal deposited on the structure and the metal deposited on the mask.

When a lower dose is used, the pattern is less distorted. Fig. 4.11b shows the fabrication result for a nominal dose of $D = 180\ \mu\text{C/cm}^2$. The impact of the proximity effect is reduced, and the resulting ridges have constant width and interdistance. However, residual metal between the ridges is still present. Indeed, even if the overexposure problem is solved and the patterning is successful, the lift-off procedure remains critical. This can be explained considering that some pulling force is needed to remove the interstitial metallic wires. If the force needed is

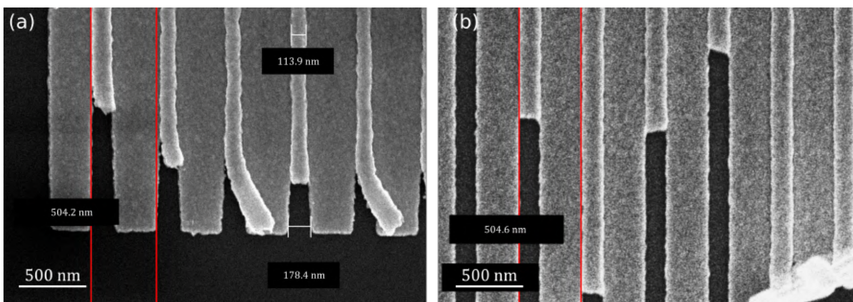

Figure 4.11 – (a) SEM image of a detail of the pattern fabricated on InAs/AlSb with dose $D = 200\ \mu\text{C/cm}^2$. The obtained pitch is shown, along with different measurements of the spacing between the single ridges. (b) SEM image of a detail of the pattern fabricated on InAs/AlSb with dose $D = 200\ \mu\text{C/cm}^2$. The obtained pitch is shown.

larger than the mechanical resistance of the single metal wire, the thin connections with the continuous film tears apart, thus removing the pulling force. Therefore, the interstitial metal is not removed from the structure.
To solve this problem, we modified the CAD by drawing squares instead of ridges, thus creating a 2D square lattice with pitch $p = 500$ nm and filling fraction $ff = 0.65$. From an optical point of view, the properties of a 2D square grating are very similar to the one of a 1D ridge grating. From the fabrication point of view instead, the interstitial metal of patterned squares forms a net, which has a larger tear resistance with respect to an array of wires, as in the case of the ridges. We performed a dose array with 5 dose steps from $D = 175\ \mu\text{C/cm}^2$ to $D = 195\ \mu\text{C/cm}^2$. The metal deposition and lift-off are the same as in the case of the ridges. Fig 4.12a and b show the results of the optimized structure for $D = 180\ \mu\text{C/cm}^2$. The obtained pitch is $p = 502$ nm, and

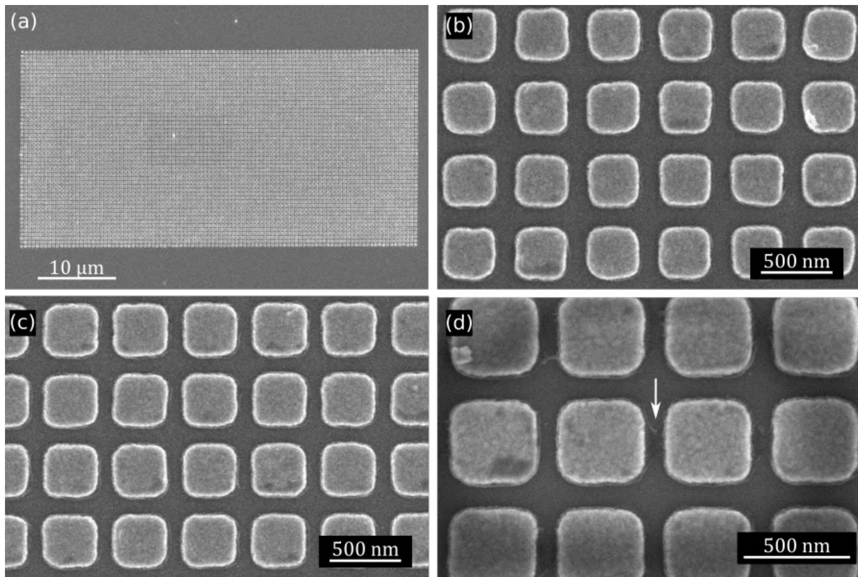

Figure 4.12 – (a) SEM image of the pattern of squares fabricated on InAs/AlSb with $D = 180\ \mu\text{C/cm}^2$. (b) Detail of (a), showing the successful fabrication. (c) Detail of the pattern on InAs/AlSb with $D = 185\ \mu\text{C/cm}^2$. (d) Detail of the pattern on InAs/AlSb with $D = 190\ \mu\text{C/cm}^2$. Interconnected adhesivant metal is visible between the ridges, as highlighted by the white arrow.

the interdistance between the squares is $\sim$ 146 nm, resulting in a filling fraction of $ff \sim 0.71$. Interestingly, we observed that it is possible to slightly modify the filling fraction while preserving the quality of the pattern by using different doses. Fig. 4.12c shows the pattern obtained for a dose of $D = 185$ μC/cm^2. The interdistance between the squares is $\sim$ 120 nm, which yields a filling fraction $ff \sim 0.75$. Fig. 4.12d shows the pattern obtained for $D = 190$ μC/cm^2, which has interdistance $\sim$ 109 nm ($ff \sim 0.8$). Some metal connecting the squares is visible. We therefore never used doses larger than $D = 185$ μC/cm^2 for fabricating the final GP structure on the SQW.
With the same recipe, we fabricated lattices with pitch $p = 370$ nm and $ff = 0.8$. We chose such geometrical factors for two different reasons: first, we wanted to measure two different pitches to study the pitch dependence of the fabricated system; second, the first PP resonance of such lattice is closer to 35.5 THz (see Fig. 4.2a). In fact, strong coupling occurs also between PPs and ISB 2$\rightarrow$ 3, and the interaction is possibly stronger due to the increased dipole.
Finally, we fabricated the arrays on the SQW substrates with graphene on top by using the recipe we optimized. To do so, we fabricated markers on the substrate by using recipe 1 from Tab. A.1. To perform an aligned lithography, we took optical images of the sample and used the markers as landmarks to superimpose the optical image with the final CAD. For a successful process, graphene boundaries must be clearly distinguishable in the picture. However, graphene on SQW substrates is not visible with optical microscopy because it cannot benefit from the Bragg reflections that increase the contrast as for the standard Si/SiO_2 substrates (see Sec. 3.1.3). To solve this issue, we used the optical contrast provided by the resist film spin coated on the sample before the EBL. This film is $\sim$ 270 nm thick and has a dielectric constant $\sim$ 3.9, very similar to SiO_2 [191, 192], thus resulting in a similarly increased contrast. To reconstruct an image of the final sample, we overlaid the image of the sample with PMMA on top with the image of the fabricated lattices without PMMA, as shown in Fig. 4.13a.

4.2.3 Reflection measurements

Once optimized the procedure, we fabricated several copies of the array on three different samples: a test device D0 on SQW-A, to study the optical response of the lattice without graphene, and two samples with graphene, one on SQW-A (device DA) and the other on SQW-B (device DB). We fabricated lattices both on the flakes and on the substrate. Moreover, we fabricated copies of the array on DA and DB with pitch $p = 370$ nm, both on graphene flakes and on the bare substrate. An example of the array fabricated on DA is visible in Fig. 4.13a, and Tab. 4.3 summarizes the different kinds of fabricated devices, along with the corresponding names used in the discussion.

We measured the fabricated sample with the micro FTIR method described in Sec. 3.2.2. A schematic of the measurement setup is reported in Fig. 4.13b. First, we studied the optical properties of the metal array by measuring its reflection spectrum on the substrate without graphene (TS5). The reflection spectra measured on TS5 and on the bare D0 substrate are shown in Fig. 4.13c, both normalized to the reflection of a mirror reference R_{Au}. In both spectra, a step-like dip in reflection is

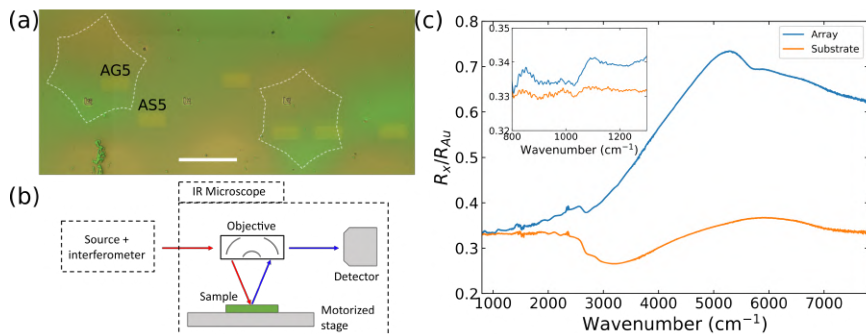

Figure 4.13 – (a) Optical image of a DA chip. The markers and the metal lattices are visible. Graphene is highlighted by white dashed lines. Different copies of the metal array were fabricated both on graphene (AG5) and on substrate (AS5). The scalebar is 100 μm. (b) Schematics of the measurement setup of the micro FTIR. (c) Reflection spectra of the lattice without graphene (blue line) and of the bare substrate (orange line). The SPP resonance is clearly visible around 5000 cm^{-1}. In the inset, a zoom of the spectra in the region of interest.

Name	Substrate	Graphene	Pitch (nm)
TS5	D0	No	500
AG5	DA	Yes	500
AS5	DA	No	500
AG3	DA	Yes	370
AS3	DA	No	370
BG5	DB	Yes	500
BS5	DB	No	500
BG3	DB	Yes	370
BS3	DB	No	370

Table 4.3 – Summary of the different lattices fabricated for the experiment.

visible for $\kappa \sim 2700$ cm^{-1}. Such dip is the onset of the interband (IB) absorption of the InAs substrate. Indeed, the bandgap of bulk InAs at room temperature is $E_g \sim 350$ meV [193], corresponding to $\kappa_g \sim 2825$ cm^{-1}. The contrast of the dip is smaller in the measurement collected on TS5 because the presence of the metal increases the reflection. Thus, the light interacts less with the substrate, diminishing the observed absorption.
The reflection of TS5 shows a wide peak with center around 5300 cm^{-1}. As discussed in Sec. 4.1.2, this peak in reflection is a signature of the SPP excited by the metallic array. The width of the peak is caused by the angle of incidence of the light on the grating. Indeed, the excitation frequency of SPPs changes with the angle (i.e., the dispersion relation of SPPs is not flat, see Sec. 2.1.4), and in our system the light impinges with a distribution of angles centered around $\sim 30°$, thus causing an effective broadening of the observed peak. In the same range of frequencies, the spectrum collected on the bare substrate shows a wide oscillation, possibly due to thin film effects in the layered heterostructure [194].
In the region of interest for the strong coupling ($800 - 1300$ cm^{-1}, see the inset in Fig. 4.13b), the spectra of the array show an increase of the reflected signal for $\kappa \sim 1050$ cm^{-1}. This increase can hardly be linked to the presence of the ISB transition. Indeed, the spectra were collected

as preliminary tests with a low number of accumulations (500), and the faint ISB absorption might be lower than noise in the spectrum measured on TS5.

After the initial study on the test sample, we measured the lattices on DA with 2000 accumulations and a resolution of 4 cm^{-1}. The reflection spectra measured on all types of lattices on DA are shown in Fig. 4.14a-b for two different copies of the same lattice geometry. As expected, the SPP resonance peak is blue shifted for shorter pitches. The wavelength of SPPs is proportional to p, thus a shorter pitch yields a shorter wavelength (i.e., larger energy). In addition, the peaks measured on AG5 and AG3 show a red-shifted energy with respect to the same peaks in AS5 and AS3. This effect can be explained by the presence of graphene below the metal, which changes the effective index of refraction of the

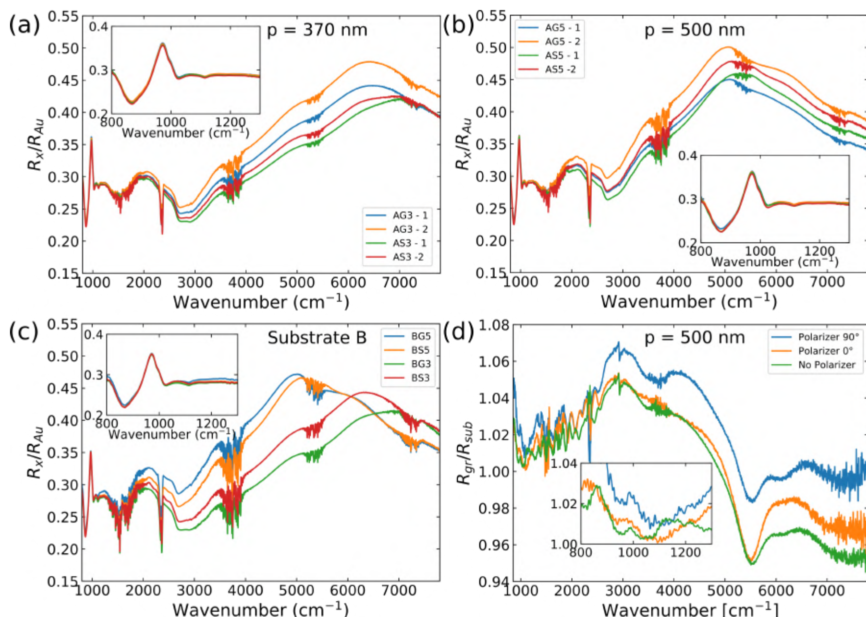

Figure 4.14 – (a-c) Reflection measured on different arrays on DA with $p = 500$ nm (a), on DA with $p = 500$ nm (b), and on DB with $p = 500$ nm and $p = 370$ nm, normalized to the reflection of a gold patch. In the insets, a zoom of the measured reflection in the region of interest for the strong coupling. (d) Ratio of the reflection measured on AG5 to the reflection measured on AS5 for different polarizations of the incoming light. In the inset, a zoom in the region of interest.

metal-dielectric interface, thus influencing the resonance frequency. In the region of interest shown in the insets of Fig. 4.14a-b, an oscillation of the signal is visible. The deep of the oscillation is centered at $\kappa = 870$ cm^{-1}, while the peak is centered at $\kappa = 960$ cm^{-1}. Such feature is present in all the measurements, both taken on graphene and on the substrate. Therefore, it cannot be attributed to graphene PPs, but possibly to the ISB transition excited by the grating. As a general remark, in all the measurements shown in Fig. 4.14a-b, we observed very little difference in the reflection measured on analogous copies of the same lattice. The small differences observed can be attributed to the slightly different filling fraction of the arrays due to variations in the exposition (see Sec. 4.2.2), which explains the slight frequency variations of the SPP around 5000 cm^{-1}, or to possible misalignment of the microscope aperture with the lattice (see Sec. 3.2.2), as in the case of the lower contrast of the signal measured on AG5-1 (blue line in Fig. 4.14b). For this reason, from now on we will only consider one copy of each geometry.
To draw better conclusions on the previous observations, we measured copies of the same lattice geometries fabricated on the non-resonant substrate DB. The resulting spectra, shown in Fig. 4.14c, present similar features as the ones measured on DA. The SPP peaks are pitch-dependent and red-shifted by the presence of graphene. Interestingly, the signal collected in the region of interest (shown in the inset) features the same oscillations as the spectra collected on DA. Thus, such signal cannot be attributed to the QW absorption, whose influence is again hidden below the noise in the measurement.
To try and isolate the effect of graphene in our sample, we normalized the measurement taken on AG5 to the one taken on AS5. The resulting spectrum (green line in Fig. 4.14d) shows a deep close to 5500 cm^{-1}that can be related to the frequency shift of the SPP peaks due to the presence of graphene described before. In the region of interest, however, features similar to the one observed in Fig. 4.14a-c are present, which cannot be clearly linked to the presence of the ISB transition.
We finally tested the in-plane polarization dependence of the reflection. The obtained spectra, shown in Fig. 4.14d, do not feature any appre-

ciable difference from the reflection measured with unpolarized light. This is expected because of the two-dimensional symmetry of the metal array, which present the same periodicity in both x and y directions.

Since no signal coming from the ISB transition could be detected in the measurements taken with 2000 accumulations, we increased the number of repetition to 25000 (see discussion on the issues related to this method in Sec. 3.2.2). First, we measured the lattices on the resonant substrate DA. The collected spectra, normalized to the reflection of the gold patch, are shown in Fig. 4.15a. The considerations made above for the SPP peaks are confirmed by these measurements. On the other hand, in the region of interest shown in the inset of Fig. 4.15a, both AG and AS spectra show a dip with a central frequency of $\kappa_d = 941$ cm^{-1}, with a FWHM ~ 100 cm^{-1}. We attribute this dip to the $1 \rightarrow 2$ ISB transition in the QW. The center of the dip is red-shifted with respect to the position measured in the multipass geometry (see Sec. 4.2.1). A possible explanation for the observed red shift is the Wood's anomaly observed in the high-frequency shoulder of the dip as a maximum above the baseline, centered at $\kappa \sim 1000$ cm^{-1}. Wood's anomalies are due to the presence of a metallic grating, on which a mode with large tangential momentum can be excited. Indeed, modifications of the lineshape and the measured resonance frequency are observed when light is coupled to ISB transitions with a metal grating [195].

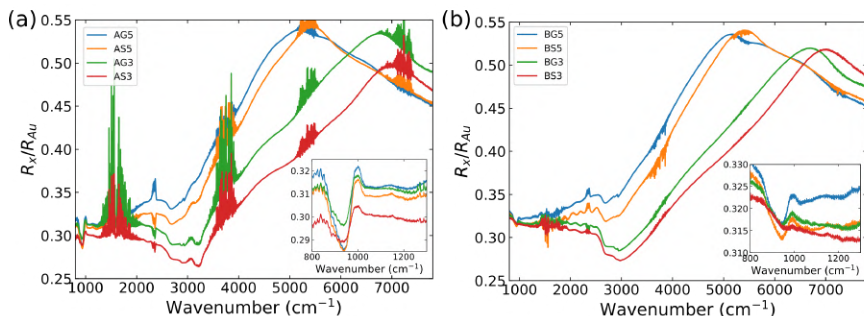

Figure 4.15 – Reflection measured on different arrays on DA (a) and on DB (b), normalized to the reflection of a gold patch. In the insets, a zoom of the measured reflection in the region of interest for the strong coupling.

The transition is visible on all the four types of lattices. AG5 and AS5 show a dip contrast of $\sim 3\%$, while the dip measured for AG3 and AS3 is less pronounced, with a contrast of $\sim 1\%$. We attribute this difference to the fact that gratings with larger pitch have a larger interdistance between the elements of the grating, thus allowing for an easier coupling of the light with the materials below. Another possible explanation is the sharper edges of the grating elements. Indeed, the edges of each element of the grating with pitch $p = 500$ nm have a low curvature radius, as shown in Fig. 4.12. When reducing the pitch, the resulting elements have less sharp edges, which yield a less intense near field, thus resulting in a lowered coupling with the ISB transition.
Finally, the presence of graphene leads to a larger coupling of light with the ISB transition. Indeed, the measured contrast on AG5 is 3.5%, while on AS5 we measured a contrast $\sim 2.5\%$. The same happens on AG3 and AS3, where we observed a contrast of 1.5% and 1%, respectively. In both cases, the contrast measured on graphene was increased by a factor of ~ 1.5 with respect to the contrast measured on AS. This difference can be attributed to the graphene conductivity, which locally enhances the overlap of the near field generated by the grating with the underlying QW, thus resulting in a increased absorption by the ISB transition.
The same measurements were performed on DB, and the resulting reflection spectra are shown in Fig. 4.15b. As in the case of DA, the SPP resonances are clearly visible on all the four types of lattices, and the resonance frequency is red-shifted when graphene is present in the structure. Interestingly, dips in reflection are visible around 950 cm^{-1} also in this structure, which does not have an ISB transition resonant in this region. We explain such dips with the presence of residues of PMMA accumulated in the structure during the fabrication. Indeed, PMMA shows different absorption peaks between 800 and 1300 cm^{-1} [191]. In particular, a peak associated to the rocking vibration of the (O)CH_3 group is centered at a wavenumber $\kappa \sim 967$ cm^{-1}. The impact of the absorption of PMMA is also visible in the region close to 2900 cm^{-1}, where the stretching vibrations of the same (O)CH_3 group yield two peaks at 2854 cm^{-1} and 2932 cm^{-1}.

As shown in both Fig. 4.15a and b, the PMMA residues are mostly visible in the spectra measured in the presence of graphene, especially in the high-frequency region around 2900 cm^{-1}. We tentatively explain this effect as a combination of different possible factors. First, graphene is more conductive than the InAlAs cap layer. The increased conductivity yields a less pronounced charging effect when performing the EBL on graphene with respect to the bare substrate, as the charge can be displaced more efficiently. Thus, the same dose can leave a different amount of residues in the two patterned structures. Such residues can be trapped below the metal during the thermal deposition, thus affecting the reflection spectra. Second, the electron beam can induce defects in graphene, as discussed in Sec. 2.3.2. Even if the delivered doses necessary to induce a consistent amount of defects are much higher than the doses employed for the patterning of the resist (tens of thousands of $\mu C/cm^2$ vs hundreds of $\mu C/cm^2$, see also Tab. A.1), the combination of the irradiation and the thermal deposition of metal can induce local modifications of the lattice of graphene. Such modifications might yield an increased adsorption of the carbonaceous residues, which would therefore be more difficult to remove with the cleaning procedures. Finally, as in the case of the ISB transitions, the presence of graphene can enhance the intensity of the local fields, resulting in an increased impact of the absorption of PMMA, even if the amount of residues coming from the fabrication processes is the same in the two systems.

To better study the effects of graphene, we isolated its contribution by normalizing the spectra of AG(BG) on the corresponding spectra of AS(BS). Two different regions of the obtained spectra are shown in Fig. 4.16a: the region of interest for the strong coupling (left) and the region around 2900 cm^{-1} where the PMMA shows two peaks (right). In the low-frequency region, the contrast of the dips on DA corresponds to the relative difference of ~ 1.5 described above. Interestingly, the dips are centered at $\kappa_d = 948$ cm^{-1}, more similar to the peak measured in the multipass geometry. On the other hand, the spectra collected on DB show wider dips with a lower contrast. Moreover, the frequency of the dips is shifted to ~ 920 cm^{-1}. The peaks around 1200

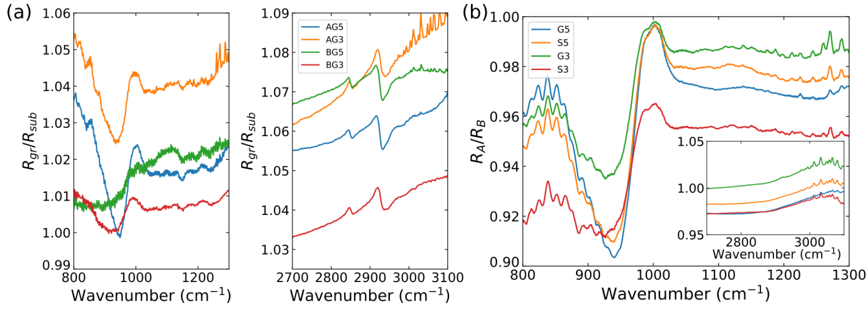

Figure 4.16 – (a) Reflection of the arrays on graphene, normalized to the corresponding reflection of the arrays on the substrate in two regions: the region of interest for the strong coupling (left) and the region around 3000 cm^{-1}, showing the impact of the absorbance of PMMA on the measured signal. (b) Reflection of the arrays on DA, normalized on the corresponding arrays on DB. In the inset, a zoom of the region close to the PMMA peaks. The peaks are not visible, showing that the chosen normalization eliminates the impact of PMMA on the spectra.

cm^{-1} are also signature of the PMMA, due to the vibration of the ester groups present in the polymer at 1150 cm^{-1}, 1194 cm^{-1}, 1248 cm^{-1} and 1270 cm^{-1}[191]. The presence of PMMA is highlighted also in the high-frequency region (right in Fig. 4.16a), where the two peaks at 2854 cm^{-1} and 2932 cm^{-1} are evident. As in the case of the maximum measured on the right shoulder of the absorption dip, the shape of the peaks in the high-frequency region is Fano-like because of the Wood's anomaly explained above.

As a last analysis, we normalized the reflection spectra collected on DA on the spectra collected on the corresponding systems on DB. The obtained spectra are shown in Fig. 4.16b. We chose this normalization to remove the PMMA absorption from the spectra, as demonstrated by the absence of the peak associated to the PMMA in the high-frequency region shown in the inset of Fig. 4.16b. The dips around 1000 cm^{-1} are visible even after removing the impact of PMMA from the measured spectra. This demonstrates that the reduced reflection is due to the absorption of the ISB transition. The center of the dips is $\kappa_d = 943$ cm^{-1}, while the contrast (not considering the Wood's anomaly) is 7% for the G5, 6.8% for S5, 5% for G3 and 4.6% for S3.

To gain information on the condition of graphene in our devices and

to have further confirmation of the presence of PMMA residues, we collected the Raman spectra of two flakes on DA: one on which a copy of AG5 was fabricated, and a second flake, never used for the experiment. The spectra collected near AG5 (blue line in Fig. 4.17a) and on the unused flake (orange line in Fig. 4.17a) are very similar, showing that the fabrication of the metal array does not degrade the graphene flake in the surroundings. A D peak is visible on both spectra, associated to a low density of defects present in the flakes even before the lithography process. Such defects can be induced in the lattice during the growth or the transfer process (see Sec. 3.1.5), and affect equally each transferred flake. Moreover, the measured G peak is not Lorentzian and shows a larger base. This is a signature of the presence of amorphous carbon on graphene [196], and points towards the presence of carbonaceous residues coming from PMMA. In addition, a peak is observed for a shift 1740 cm^{-1} (black arrow in Fig. 4.17a). The peak is not associated to the phonons of graphene, but rather to the stretching vibration of the C=0 group present in PMMA [191]. We also collected a spectrum on the bare substrate of DA (green line in Fig. 4.17a), which shows the same peak centered at 1740 cm^{-1}, less pronounced with respect to one measured on graphene (see inset in Fig. 4.17a). The Raman spectra therefore suggest that PMMA residues are present on the whole surface of DA. Consequently, we can conclude that the absorption of PMMA impacts more on the spectra collected on graphene mostly because of the enhanced intensity of the interacting fields.

Since PMMA residues are present on the whole structure, we can conclude that the electron beam irradiation is not the cause of the presence of the residues. More likely, the residues can come from the heating of the PMMA films either during the transfer of the CVD graphene or during the preparation of the sample for the lithography. In particular, the spin coated PMMA resist for the EBL is baked at 160°C for 3 minutes (see Appendix A). Such temperature is very close to the glass transition of the used PMMA [197], and can thus lead to the formation of amorphous structures. These are difficult to remove without an etching step (e.g., oxygen plasma), which can damage graphene and cannot be added in the fabrication process of our samples.

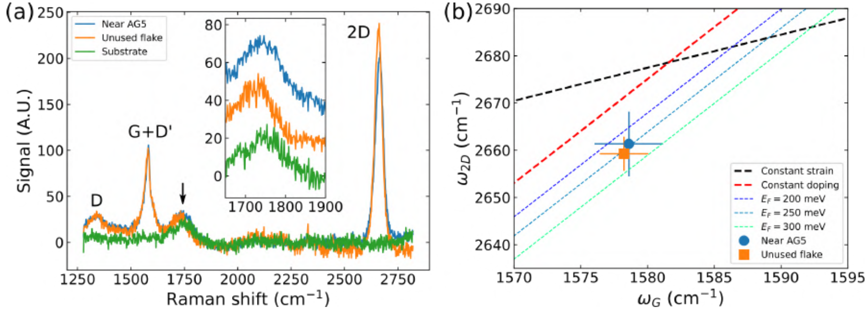

Figure 4.17 – (a) Raman spectra collected on graphene near AG5 (blue line), on an unused flake (orange line) and on the bare substrate (green line). The spectra on graphene show the presence of defects, possibly coming from the transfer. The peak pointed with the black arrow is associated with the presence of PMMA in the structure. In the inset: comparison of the peak at 1740 cm^{-1} . Each spectrum is shifted of 20 A.U. for clarity.(b) Correlation plot of the position of the G and $2D$ peaks extracted from Raman spectra collected on graphene on DA. The shown points are the average of different spectra taken on a flake where AG5 was fabricated (blue dot) and on a flake not used for the experiment (orange star). The error bars are the standard deviation from the average of the measurements. Lines of constant doping and constant strain are reported [60].

So far, we demonstrated that the grating can excite the ISB transitions in the QW and observed that graphene enhances the resonant absorption, but no signature of strong coupling could be isolated in the system. However, an important parameter in the system is the Fermi energy of graphene. Indeed, as shown in the simulations (see Sec. 4.1.2), the best condition to observe the strong coupling is to have a Fermi energy close to 0.5 eV. To gain information on the doping and strain of our flakes, we can correlate the position of the $2D$ and G peaks of the Raman spectra [60]. Such correlation plot is shown in Fig. 4.17b for both measured flakes. Different points were collected on each flake to have a statistical population with more significance than a single point measurement. The different measurements were averaged and the standard deviation used as error. In the graph, lines of equal doping are reported (red thick dashed line and dashed lines parallel to the latter), along with the line of zero strain (black dashed thick line). The points

collected near AG5 (blue dots in Fig. 4.17) show a larger dispersion with respect to the ones collected on the unused flakes. However, for both flakes, the average doping is around 250 meV, not enough for observing clear signature of the strong coupling (see Fig. 4.3a).
As discussed in Sec. 2.1.2, it is possible to take advantage of the ambipolar field effect to modify the Fermi energy inside graphene. To do so, it is necessary to build a geometry to apply a potential between graphene and a gate electrode. In the presented case, it is not possible to employ the substrate as a dielectric to back gate the sample. First, the semiconductor structure is not insulating and the application of a voltage between the InAs substrate and an electrode fabricated on top of the structure would result in the conduction of carriers, which hinders the build up of the potential. Even if the potential difference could be established, the charge carrier density in the QW would change as an effect of the back gate [198], thus modifying the optical properties of the ISB. Furthermore, the change in the QW carrier density would screen the applied potential, effectively hindering the gating of graphene.
To solve this issue, we employ ionic liquid gating. For our experiment, we needed an IL which is also transparent in the region of interest in the spectrum. Since no commercial solution was available, we designed and studied two different bromide-based IL embedded in PMMA in collaboration with the Ionic Liquid Group, led by Christian Silvio Pomelli at the Department of Pharmacy of the University of Pisa [199]. The full study of the optical and transport properties of such ionic liquids is reported in Appendix B. We chose to embed the ionic liquid in PMMA to enable the possibility of spin coating the liquid into a thin film, which offers both a controllable thickness and a flat interface between the liquid and air. In fact, the IL are usually drop casted on the sample. However, the shape and lateral dimensions of the obtained droplets are hardly controllable. Moreover, the droplet offers a round interface to the incoming light and can cause unpredictable lensing effects, which are undesired in optics experiments. Fig. 4.18a shows the transmission spectra of a Si/SiO_2 chip spin coated with a film of the studied ionic liquids (PES1 and PES2) compared to the spectrum collected through the bare substrate. The presence of PMMA is visible

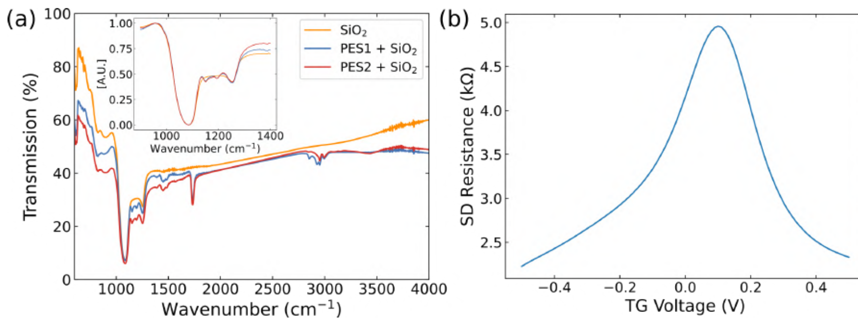

Figure 4.18 – (a) Transmission spectrum of a Si/SiO_2 chip (orange line), compared to the transmission of the same substrate with two different PMMA-embedded ionic liquids (PES1 and PES2). In the inset, a zoom of the signals in the region around the SiO_2 phonons [192]. The minima were shifted to 0 and the signal normalized on their maxima to compare the shape. Taken from [199]. (b) Modulation of the resistance of a gFET by top gating with one of the studied electrolytes (ES1).

in different regions of the spectrum. Nevertheless, the absorption of the SiO_2 phonons around 1200 cm^{-1} [192] is not hidden by the film, as shown in the inset of Fig. 4.18a. We tested the gating efficiency of the IL by performing 2W electrical measurements on a gFET built on Si/SiO_2 in a vacuum chamber. By using PES2, we achieved a strong modulation of the resistance of the graphene channel in a span of 1 V of gating potential, as shown in Fig. 4.18b.

To avoid damages at the metal contacts due to the acidification of the IL, as explained in Appendix B, we measured the sample in a homemade vacuum chamber equipped with a ZnSe window, as shown in Fig. 3.14c. This chamber is thin enough to be put below the microscope objective, thus allowing optical measurements while the sample is kept in vacuum. For these measurements, we fabricated new AG5 and AS5 devices on DA by repeating the single array 2 times in width and 3 times in height, as shown in Fig. 4.19a. We distanced each array of 5 μm, to enable the successful fabrication of large-area arrays without hindering the lift-off procedure (see Sec. 4.2.2). We fabricated a sample with a large measurable area to increase the S/N ratio. Indeed, the ZnSe window and the IL thin film add new interfaces in the optical path, which reduce the signal recollected at the detector. Source and drain contacts

were also fabricated on the graphene flake, and are visible in Fig. 4.19a. After the deposition of the metal elements, we spin coated DA with a 290 nm thick film of PES2 using the spin coating procedure (see Appendix A) and soft-baking the sample at 100°C instead of 160°C not to modify the properties of the IL. The IL electrode was deposited on top of the IL film to avoid any possible electrical contact with graphene through the surface of the chip. The schematics of the final device is shown in the inset of Fig. 4.19a. The chip was then mounted on the copper chip carrier (see Fig. 3.11b) and bonded to the ceramic pads. The electrode on top of the film was hand bonded by Alessandro Profeti at Istituto Nazionale di Fisica Nucleare (INFN) in Pisa to avoid any possible damage to the soft polymer caused by the ultrasound tip of the wedge bonder.
We performed measurements on the large area AG5 as a function of the applied gate voltage V_{TG}. To highlight the effect of the increased voltage, we normalized the measurements on the curve collected when the sample was grounded. Fig. 4.19b shows the resulting spectra. The

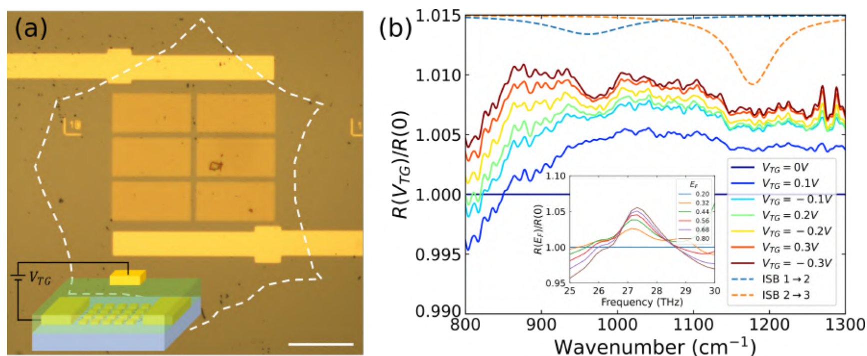

Figure 4.19 – (a) Optical image of a large area AG5 used for experiments with the IL. The source and drain contacts are visible. The graphene flake is highlighted with a white dashed line. In the inset, a schematics of the final device. (b) Reflection spectra of large area AG5 in the spectral region of interest, as a function of the applied top gate voltage V_{TG}. The spectra are normalized on the spectrum collected with no applied voltage. The dashed lines are two Lorentzians with the parameters extracted from the fit of the multipass measurement and reported in Tab. 4.2. In the inset, reflection spectra in the high-frequency region where PMMA was observed.

spectra show a baseline which increases with the applied voltage. This can be explained by considering that the doped graphene has an increased reflection. Moreover, a dip appears when increasing the voltage, centered at $\kappa \sim 960$ cm^{-1}and with a width of ~ 60 cm^{-1} for $V_{TG} = \pm 0.3$ V. The maximum contrast of the dip is $\sim 0.3\%$. The change in contrast of the dip can be a signature of the weak coupling between the graphene plasmons and the ISB transition in the QW. Indeed, by increasing the Fermi energy inside graphene, the local fields have longer penetration depths, and the field exciting the ISB transition has a higher intensity. This effect is also predicted by the simulations: the inset of Fig. 4.19b shows lines extracted from Fig. 4.3a and normalized on the simulated reflection spectra for $E_F = 0.2$ eV. An increase of the contrast is visible, with a maximum of $\sim 5\%$ for $E_F = 0.8$ eV.

4.3 Partial Conclusions

In this chapter, we presented the theoretical study of two different systems where graphene PPs are coupled with ISB transitions in a single SQW. We proved the possibility of reaching the ultra strong coupling regime between the two excitations by using an array of metallic ridges. In the GP geometry, we predicted a coupling strength of $g = 0.18$ with a number of involved electrons $N \approx 10^2$. We also exploited the recently achieved ultra-confinement of AGP modes to design a system (AGP geometry) where a coupling strength of $g = 0.11$ can be achieved with a remarkably low number of involved of electrons $N \approx 10$. By putting a metallic substrate below both geometries, we demonstrated an increase of the absorption of the cavity, eventually reaching critical coupling conditions in the GP geometry.
We presented the experimental campaign we carried out on a SQW structure analogous to the simulated GP geometry. First, we demonstrated the ISB absorption of the QW with multipass measurements, where we observed both $1 \rightarrow 2$ and $2 \rightarrow 3$ IBS transitions in accordance to the theoretical predictions.
We optimized the fabrication of metallic arrays of squares on the SQW

surface, showing the successful realization of arrays with pitches of 500 nm and 370 nm, with areas large enough to be measured with the μFTIR.
We observed the ISB transitions excited with the fabricated metal arrays. The detrimental contribution of PMMA residues left on the device from the fabrication was ruled out by a proper normalization, showing the clear absorption of the QW with a maximum contrast of $\sim 7\%$ of the signal. Moreover, the impact of graphene was isolated as an enhancement of the ISB absorption of $\sim 1.5\%$ of the measured signal.
Finally, we exploited a PMMA-embedded ionic liquid that we developed to modify the carrier concentration in the graphene sheet. The obtained results show signature of the weak coupling between the QW and the graphene PPs as an enhancement of the resonant absorption, also predicted by our simulations.
Further studies must be carried out to confirm our findings, for example by building the metal-insulator-metal cavity we proposed. Another possibility is to employ arrays of nanoridges milled by focused ion beam (FIB) and transferred on the sample. This would both eliminate the detrimental effects of the fabrication via EBL (PMMA residues and possible damage to the graphene lattice), and also offer a better metal-graphene interface than the one generated with the thermal deposition of metals. Indeed, during the thermal deposition, some metal atoms can substitute the carbon atoms in the lattice, thus creating a rough interface with no precise distinction between the two materials, which can impact also on the surrounding areas of the crystal.

Chapter 5

Coherent properties of a pattern of defects

In Sec. 2.3.3, we described how a line of defects could be considered as a potential barrier for charges moving in graphene. We introduced the effects of the periodic repetition of potential barriers as conductance oscillations due to a combination of Klein tunneling and Fabry Pérot resonances. In this chapter, we discuss the realization and transport measurements of FET devices on Si/SiO_2. The peculiarity of such FETs is that the channel is a graphene flake on which we engineered a regular array of defects via electron beam irradiation (EBI) at 20 keV. First, we investigate the time stability and defect population of the created defective sites with Raman spectroscopy and molecular dynamics (MD) simulations. Then, by combining Raman spectroscopy with AFM measurements, we show that it is possible to pattern regular arrays of defects with a lateral resolution of tens of nanometres via low-energy EBI. Finally, we present the transport measurements results obtained on defected-graphene FETS (d-gFETs) at low temperature.

5.1 Engineering a defective pattern

Tailoring graphene properties via defective patterns requires features which are both stable in time and tailored with nanometric lateral resolution. To verify that defects induced with low-energy EBI show

such properties, we employ Raman spectroscopy, AFM measurements, and MD simulations. We start by studying the population and time stability of the created defects. The results of such experiment were published in [200].

5.1.1 Time stability of the defects

The formation energy of the defects in graphene depends on the nature of the defect, but is in general larger than a few eVs [99]. Such high formation energy ideally yields a high stability of the defects at room temperature. However, the energy barriers for the migration or modification of defects already present in the lattice are lower, and a non-trivial time evolution of the defected site can be expected also at room temperature. For example, the vacancies in the lattice can be filled by the successive interaction of the dangling bonds with CO, which saturates the bonds with the carbon atom, and NO, which removes the oxygen by becoming NO_2 [201]. Partial healing was observed on CVD-grown graphene in which defects where engineered by e-beam chemistry in a SEM [202]. Moreover, residual carbon atoms displaced from the lattice but adsorbed to the undamaged lattice can cluster and create structures that can diffuse to the defected site and induce healing [203]. Such process was observed in defect-engineered suspended graphene when close-by hydrocarbon contaminants acted as a source of carbon [204].

The evolution of defected graphene when left exposed to air can therefore be a complex process, which induces deep modifications in the defect population. To study the time stability of the defects we engineered via EBI, we employed a graphene flake obtained with the mechanical exfoliation method (see Sec. 3.1.4), shown in Fig. 5.1a. We irradiated the flake with recipe 5 in Tab. A.1 (Appendix A) on a 6 μm long area as wide as the flake (black dashed rectangle in Fig. 5.1a). The sample was left in air atmosphere and was studied by repeating Raman spectroscopy measurements over a period of 250 day ($\sim 6 \times 10^3$ h). Fig. 5.1b shows the comparison of the obtained Raman spectra collected on the as-exfoliated (blue line) and the irradiated (orange line) parts of the flake right after the irradiation ($t_0 = 0$ h). The spectrum

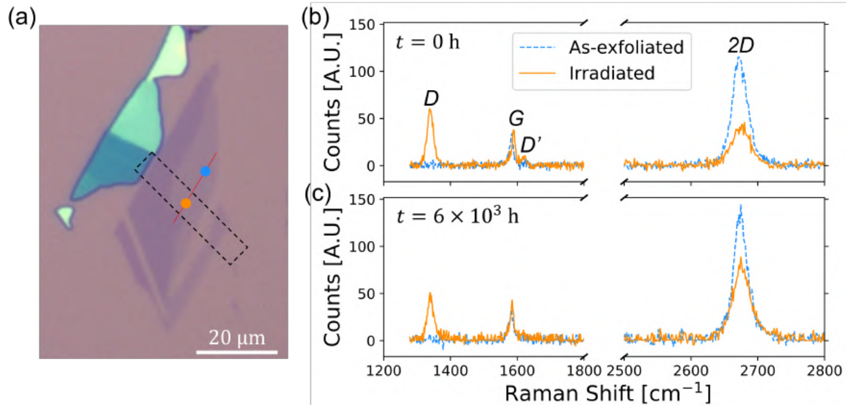

Figure 5.1 – (a) Optical image of the graphene flake used in the experiment. Defects were induced by EBI at 20 keV in the area enclosed in the black dashed rectangle. The orange and blue dot are the position at which the spectra shown in (b) and (c) were measured. Linescan measurements were taken along the red solid line to study the temporal evolution of the induced defects. (b) Comparison of the Raman spectra collected on as-exfoliated graphene (blue line) and on irradiated graphene (orange line) right after the irradiation ($t_0 = 0$ h). (c) Comparison of the Raman spectra collected as in (b) after the flake aged in air atmosphere for $t_f = 6 \times 10^3$ h.

collected on the as-exfoliated graphene is similar to the spectrum of pristine graphene, with Lorentzian $2D$ and G peaks (see Sec. 2.1.3). Such form of the spectrum shows that the unexposed area is not affected by the irradiation process. Conversely, the spectrum measured on the irradiated part of the flake shows strong modifications which suggest the presence of disorder in graphene. To study the induced disorder, we fitted the spectra with Lorentzian peaks. The results are reported in Tab. 5.1. First, the $2D$ peak shows a lower intensity and a larger $FWHM$ in the irradiated part with respect to the non-irradiated flake, and a D peak higher than the G peak is visible. In addition, the G peak is blue shifted with respect to as-exfoliated graphene, and a D' peak is visible. These features are a signature of the presence of defects in the lattice of graphene [129, 205], and confirm the local creation of defects with the EBI. Moreover, the shape of the spectrum does not show the presence of amorphous carbon, i.e. graphene is still in

$t = t_0$	Irradiated				As-exfoliated	
	D	G	D'	$2D$	G	$2D$
I	56	30	8.4	39	27	115
ω_r	1340	1589	1620	2675	1583	2673
$FWHM$	19	14	13	29	12	23
$t = t_f$	Irradiated				As-exfoliated	
	D	G	D'	$2D$	G	$2D$
I	47	43	–	93	32	148
ω_r	1341	1585	–	2676	1582	2674
$FWHM$	16	13	–	25	17	22

Table 5.1 – Fit results for the spectra taken on irradiated and as-exfoliated graphene for $t = t_0$ (Fig. 5.1b) and for $t = t_f$ (Fig. 5.1c). I is the amplitude of the peak in A.U., ω_r is the position of the peak in cm^{-1}, $FWHM$ is the full width at half maximum of the peak in cm^{-1}. For the as-exfoliated area, we did not consider the D and D' peaks.

stage 1 (see Sec. 2.1.3). Thus, we use Eq. 2.6 introduced in Sec. 2.1.3 to quantify the defects induced in the lattice. The equation correlates the ratio $I(D)/I(G)$ of the intensities of the G and D peaks to the density of defects in the lattice. From the data in Tab. 5.1, we extract a $I(D)/I(G)|_{t_0} = 1.86$, which corresponds to a density of defects induced by the irradiation of $n_D(t = t_0) \sim 4 \times 10^{11}$ cm^{-2}.
Fig. 5.1c shows the comparison of spectra collected on the same areas of the flake after a time $t_f = 6 \times 10^3$ h from the initial EBI. The signal collected on the as-exfoliated graphene is similar to the one collected at t_0. This demonstrates that pristine graphene does not deteriorate over time and interacts very little with the environment. Instead, the spectrum of irradiated graphene shows an evolution with respect to the one collected at t_0. First, the D peak is reduced in both intensity and $FWHM$, and the D' becomes so low that it cannot be clearly distinguished. The G peak is shifted closer to the as-exfoliated conditions and the $2D$ peak shows both a higher intensity and a diminished $FWHM$, indicating a partial restoration of the lattice. Indeed, the intensity ratio $I(D)/I(G)|t_f = 1.1$, which results in a density of defects at the last measurement $n_D(t = t_f) \sim 2.3 \times 10^{11}$ cm^{-2}. The difference observed between the two spectra indicates that some modifications happened

in the defective lattice of irradiated graphene because of the aging. To study the evolution over time of the induced defects, we performed different Raman measurements over time, consisting of line scans along the red line shown in Fig. 5.1a. The laser was scanned with steps of 500 nm, so that several points were collected both on the irradiated and on the as-exfoliated part of the flake. The extracted points were averaged for each measurement, and the standard deviation was taken as the error. Fig. 5.2a shows the $I(D)/I(G)|_t$ ratios measured as a function of t. The corresponding values of n_D computed with Eq. 2.6 are reported on the right vertical axis. The evolution of the defect density can be divided into two phases: the first phase goes from 10^{-2} h to 10 h and shows a constant density of defects, while the second phase goes from 10 h to 10^4 h and is the phase where all the reduction of the ratio occurs, suggesting a room-temperature self-healing of the defects. To

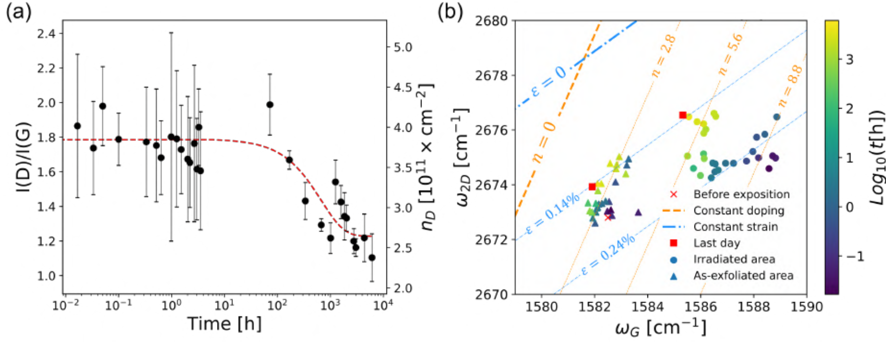

Figure 5.2 – (a) Evolution over time of the $I(D)/I(G)$ ratio extracted from the spectra collected on the irradiated area of the flake. The error bars are the standard deviation computed over multiple measurements on the same line. The data were fitted with an exponential decay (red dashed line), from which a decay time $\tau_D = 670$ h was extracted. The right vertical axis reports the density of defects corresponding to the measured intensity ratio by Eq. 2.6. (b) Correlation plot of ω_{2D} versus ω_G extracted from spectra collected on as exfoliated (triangles) and irradiated (circles) graphene. A measurement performed on the flake before the exposition is indicated with a red cross. The colorbar represents the base 10 logarithm of time, measured in hours. Lines of equal strain ϵ (blue) and equal charge doping n (orange) are reported [60]. Doping values are given in units of 10^{12} cm^{-2}.

quantify the timescale of the reduction of $I(D)/I(G)|_t$, we performed a fit with an exponentially decaying function

$$f(t) = Ae^{-t/\tau_D} + B \tag{5.1}$$

where τ_D is the decay timescale, A is the fraction of defects healed in the evolution over time and B is the residual density of defects at the end of the evolution. Even if the timescale of the evolution can be divided into two phases, we employed a single decaying function to fit the data because the timescale of the first phase ($\sim$ 10 h) is negligible with respect to the second one ($> 10^2$ h). Indeed, the extracted time constant is $\tau_D \sim 670$ h (see Tab. 5.2). In this model, the starting density of defects can be computed as $f(0) = A + B \sim 3.9 \times 10^{11}$ cm^{-1}, whereas the percentage of residual density of defects at the end of the evolution with respect to the starting density is $\rho_{rD} = 100 \cdot B/(A + B) \sim 69\%$.

	A	B	τ (h)
$I(D)/I(G)$	0.56	1.23	670
n_D (10^{11}cm^{-2})	1.21	2.64	670

Table 5.2 – Fit results for the temporal decay of the measured density of defects. Values for n_D are computed with Eq. 2.6 reported in Sec. 2.1.3.

Since graphene is Stage 1 (see Sec. 2.1.3), the position ω_G and ω_{2D} of the G and $2D$ peaks can be correlated to gain information on the doping and strain of the examined structure [60]. Such correlation plot is shown in Fig. 5.2b. At time t_0, the irradiated part shows a higher doping with respect to the as-exfoliated area. Also, the irradiated area shows a higher tensile strain than the as-exfoliated area. The increased strain is a signature of the presence of defects in the lattice [206, 207]. On the other hand, the data collected on the as-exfoliated area are comparable to the values obtained on the crystal before the irradiation (red cross in Fig. 5.2b). After the initial irradiation, the two areas evolve differently over time. In the irradiated area, two temporal phases can be isolated as in Fig. 5.2a. During the first 10 hours, the doping decreases from a value $n \sim 8.8 \times 10^{12}$ cm^{-2} to $n \sim 5.6 \times 10^{12}$ cm^{-2}. Such effect is due to the accumulation of charge impurities in the substrate during

the exposition [208]. Indeed, charge impurities in SiO_2 show decay time reported in the literature of ≤ 10 h after the irradiation [209]. After that the doping is decreased, the lattice relaxes its tensile strain from a value $\varepsilon = 0.20\%$ to $\varepsilon = 0.12\%$ in a timescale of $10^2 - 10^3$ hours. During this process, the change in doping is negligible. Conversely, the as-exfoliated area evolves following a different path. First, the evolution happens in one homogeneous phase, differently from the two phases identified in the case of the irradiated area. Second, the doping of the crystal is constant at $n \sim 2.8 \times 10^{12}$ cm^{-1} during the whole evolution, while the strain decreases. Eventually, the two areas reach a stable condition where both share the same strain value $\varepsilon = 0.12\%$. These observations suggest that, while the crystal is strained locally on the irradiated area by the defects induced with the EBI, during the evolution such strain relaxes, impacting also on the as-exfoliated area. Eventually, a stable condition which involves the whole flake is reached.
To understand more in depth the mechanism driving the observed evolution, we studied the nature of the defects by examining the intensities of the D and D' peaks (see Sec. 2.1.3). Fig. 5.3a shows the observed intensities of the two peaks, normalized on the relative G peak intensity. The two parameters show a linear correlation with a coefficient $\alpha = I(D)/I(D')$. As explained in Sec. 2.1.3, this ratio gives information on the statistical composition of the defect population [68]. The two phases of the evolution are distinguishable also in the time evolution of this parameter. Therefore, we fitted the two phases and extracted two different coefficients $\alpha_{1,2}$, respectively. The first phase is characterized by a coefficient $\alpha_1 \sim 7$, while for the second phase $\alpha \sim 11$.
Following [68], the value of α_1 indicates that after the exposition, the defect population is mainly composed by vacancy-like sites, such as borders and holes in the lattice. Indeed, as explained in Sec. 2.3.2, irradiation at such low energy does not transfer enough energy for a collision to displace a carbon atom in a defect-free graphene lattice. Nevertheless, the interaction of the electrons with the substrate and the presence of native defects in the lattice can yield strong modifications in the morphology of the crystal, thus explaining the presence of vacancies,

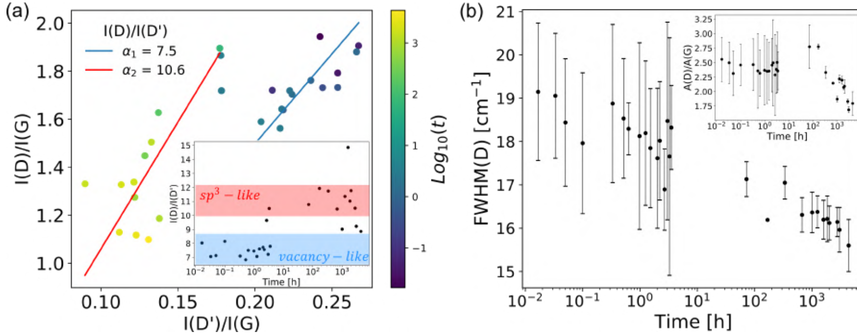

Figure 5.3 – (a) Plot correlating the intensities of D and D' peaks collected on the irradiated area of the flake, normalized to the intensity of the G peak. The color bar represents the base-10 logarithm of the elapsed time, measured in hours. Linear fits of the two temporal phases characterizing the evolution are shown (solid lines). In the inset, the ratio $I(D)/I(D')$ is plotted as a function of time for a better overview of the time evolution. (b) Plot of the time evolution of the full width at half maximum $FWHM(D)$ of the D peak extracted from the spectra measured on the irradiated part of the flake. In the inset: plot of the time evolution of the ratio $A(D)/A(G)$ of the areas of the D and G peak, respectively. The error bars are associated to statistical error over multiple consecutive measurements on the same line.

suggested by the extracted coefficient.
After the creation of the defects, vacancy-rich defects remain in the first 10-h phase (blue shaded area in the inset of Fig. 5.3a). Then, the coefficient increases to α_2, suggesting a change of the population towards a majority of sp_3-like defects (red shaded area in the inset of Fig. 5.3a). We attribute this behaviour to the partial healing of the defects, also influenced by the air contaminants. These can bond to the dangling bonds present in the defected area, thus changing the hybridization of the involved carbon atoms. By combining this process with the behaviour of the ratio $I(D)/I(G)$ shown in Fig. 5.2a, one might conclude that the defect density does not decrease and the healing process is in fact absent. Indeed, if many contaminants bonded to the carbon dangling bonds, the measured intensity of the D peak would diminish because of the presence of such molecules [67] and not because of the reduced density of defects. However, another indication of the presence of external molecules is given by the full width at half

maximum $FWHM(D)$ of the D peak. Adventitious molecules bonded to the dangling bonds yield a broadening of the D peak because of the larger energy spectrum of the bonds between carbon and different type of molecules [67]. As shown in Fig. 5.3b, the width of the measured D peak in our sample decreases from a value of 19 cm^{-1} to a final value of 16 cm^{-1}. This decrease implies that the area of the measured D peak also diminishes over time, as shown in the inset of Fig. 5.3b, and that the density of defects in the crystal undoubtedly lowers, confirming the presence of a healing process.

To explain the observed behaviour on the atomic scale, we compared our experimental results with molecular dynamics (MD) simulations performed by Dr. Luca Bellucci from CNR-NANO. The simulated system, shown in Fig. 5.4, consists in a triclinic cell with $a = b = 7.6$ nm, $c = 8$ nm, $\alpha = \beta = 90°$, $\gamma = 120°$. Two graphene layers are placed at the surfaces of a slab of amorphous silica (aSiO_2, Fig. 5.4a). We chose to use 2 graphene sheets for each system to double the statistical population of the simulation campaign without increasing the number of simulated systems. The interaction between the rigid SiO_2 slab and the other chemical species of the system weas treated by using Lennard-Jones potentials with parameters selected from literature.

The effect of the EBI was mimicked by exploiting the primary knock-out atoms (PKAs) method [122, 210–213]. The graphene on top of

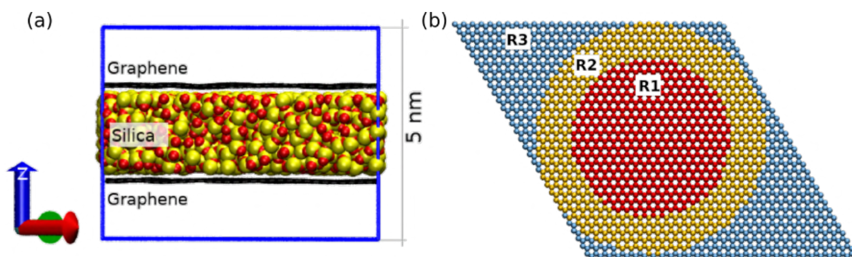

Figure 5.4 – Cell of the MD simulation, composed of two graphene layers supported by amorphous SiO_2. (a) Lateral view of the cell. (b) Top view of the cell, without the aSiO_2. The box is 5 nm tall and the two main axes are $a = b = 7.6$ nm long. The angle between the axes is $\alpha = 120°$. The three regions of the simulation are shown with different colors.

$aSiO_2$ was divided in 3 different regions, as shown in Fig. 5.4b. Atoms in the first region (R1) were randomly selected each 14 ps, and a velocity $v_c \sim 0.08$ Å/fs was added to the z-component of the velocity of the selected atoms. Such a velocity corresponds to the transferred energy from an incoming electron of energy $E = 20$ keV, which is $E_{max} \sim 3.7$ eV, according to Eq. 2.17. The second region (R2) was used to decouple R1 from the bulk region (R3). During the simulation, the temperature of R1 gradually increases, mimicking the flux of incident electrons, and part of the energy is transferred through R2 to R3, which acts as bulk graphene absorbing the excess energy in the thermostat. The amount of defects was controlled by checking the mean square displacement (MSD) of the R1 atoms with respect to the initial positions. The described irradiation process terminated when the measured MSD reached a fixed threshold. A total of 38 equivalent systems were subjected to electron irradiation, thus generating 76 different defective graphene lattices. A relaxation procedure in vacuum was carried out to mimic the time evolution. Further information on the MD simulation can be found in [200].

Fig. 5.5a and b show an example of the simulated defected sites right after the irradiation process and after relaxation, respectively. As-created defects (Fig. 5.5a) appear like a cluster of defects composed of vacancies, carbon polygons and carbon chains. During the irradiation, the planar graphene structure is partially converted into a corrugated lattice with sp, sp_3 and unsaturated C atoms. During the relaxation, the dangling bonds tend to be saturated by other C atoms. Therefore, the defected site reduces in lateral size and the crystal is partially reconstructed (see. Fig. 5.5b).

The defected systems were sorted according to the initial percentage of defected atoms in each system $N_{D,0}/N_A$, where N_A is the total number of carbon atoms in the cell. Fig 5.5c shows the percentage of defected atoms $N_{D,x}/N_A$ before ($x = 0$) and after the relaxation in vacuum ($x = f$) as a function of the initial percentage. The blue line referring to the as-created conditions can be used as a reference. Interestingly, $N_{D,f}/N_A$ shows a linear behaviour (orange curve in Fig. 5.5c). We fitted the data with a line and extracted a coefficient $\rho = 0.7$. This suggests

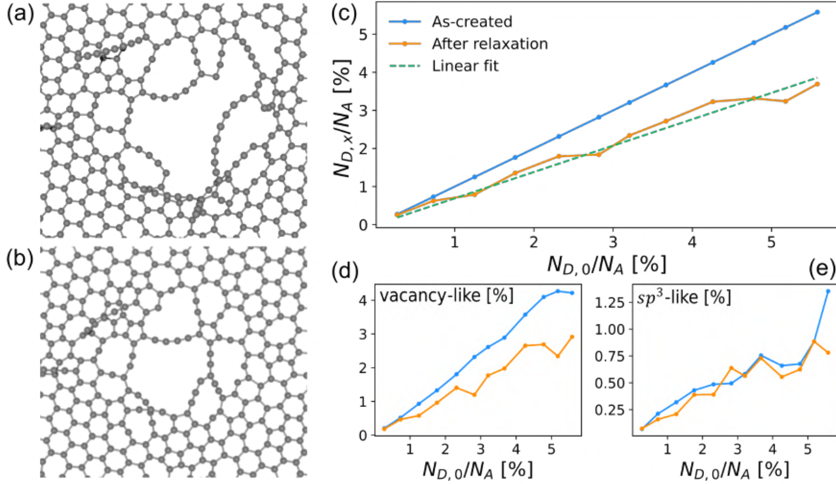

Figure 5.5 – (a) Example of a simulated defected site. (b) The same site as in (a) after the relaxation process in vacuum. (c) Percentage of defected atoms in the system before (blue line, $x = 0$) and after (orange line, $x = f$) the relaxation process in vacuum as a function of the percentage of defected atoms before the relaxation. The green dashed line is a linear fit. The extracted coefficient is $\rho \sim 0.7$. (d, e) Percentage of vacancy-like (d) and sp^3-like (e) defects before (blue line) and after (orange line) the relaxation process in vacuum.)

that the healing process depends on the size of the defected area but, on average, the fraction of healed defects is at least about 30% of the starting distorted atoms, in good agreement with the experimental observations (see Fig. 5.2a).

As seen in the experimental results, vacancy-like defects can be distinguished from sp_3-like defects by the different Raman activity. However, the simulations can give an atomistic insight, with which it is possible to give a more detailed definition of such categories. In fact, the two types of defects are composed by different kinds of C atoms. The simulations allow the identification of such kinds of atoms: the first group (vacancy-like) includes atoms at the border of large holes or linked to linear chains, while the second (sp_3-like) includes sp_3-hybridized atoms and quantifies the deviation from the planarity of the C atoms in the lattice. The results of the simulated evolution of these two groups allow to better understand the experimentally observed change from vacancy-rich

to sp_3-rich population shown in Fig. 5.3a. The number of vacancy-like defects decreases during the relaxation as the hole partially refills with hexagonal rings (Fig. 5.5d, while the sp_3-like population remains on average constant (Fig. 5.5e). We explain this behaviour considering that, on the one hand, the sp_2 atoms with dangling bonds at the edge of the hole and the linear chains (i.e., vacancy-like atoms) are prone to react towards saturation because of the presence of dangling bonds. The simultaneous availability of dangling bonds and the movable linear C chains enable this saturation process, which is at the base of the observed reconstruction of graphene. On the other hand, even if some sp_3-like atoms can relax towards a more planar disposition, other atoms in the surroundings can rearrange during the evolution as an effect of the reconstruction (see Fig. 5.6a and b). Therefore, the overall sp_3-like population does not change in average during the evolution. Since one type diminishes while the other does not, such findings explain the shift in the population observed experimentally.

Even if performed in vacuum, the simulations well reproduce the healing trends that are experimentally observed in ambient air. This similarity can be explained by considering that the lattice reconstruction involves defects with different nature, each following a different evolution path over time. When exposed to ambient air, defective sites may react chemically with contaminants in the atmosphere due to the enhanced chemical reactivity [25, 214]. We observed a larger charge doping in the irradiated areas compared to the pristine graphene, which can be attributed to adsorbed molecules on the structure. However, the probability of chemical bonding between defects and airborne contaminants is modest at standard temperature and pressure [215], as also proven by the D peak narrowing during the evolution observed in our samples (see Fig. 5.3b). Therefore, the interaction of the defects with external molecules is not immediate, but rather the evolution is characterized by a saturation process of the electron-induced dangling bonds, allowing the vacancy-like defects to be reconstructed during time even without the interaction with the environment.

To further study the role of the chemical reactive sites in the healing process, we carried out additional MD simulations, subjecting the

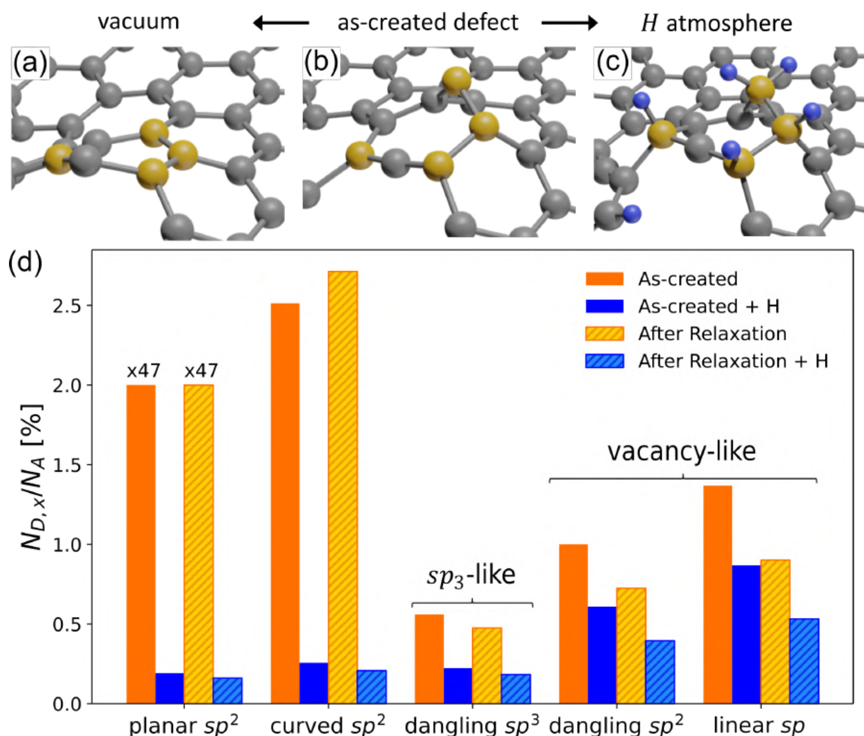

Figure 5.6 – (a, b, c) Example of two possible evolution outcomes that a distorted sp^2 atom can undergo. The yellow spheres are the C atoms in the lattice interested by such evolution, the blue spheres are H atoms introduced as contaminants. (d) Histogram of the percentage of atoms categorized by hybridization and averaged over all the systems for the as-created systems (solid bars) and relaxed systems (textured bars). The orange bars show the average percentages of atoms before the hydrogenation, while the blue bars show the percentage of the atoms of the corresponding starting hybridization that bonded with hydrogen atoms.

systems to tempering cycles in the presence of atomic hydrogen. We employed atomic hydrogen because it is an active species, suitable to test the reactivity of the defected sites. While pristine graphene is chemically inert in the chosen condition (see Supplementary Information of [200]), the defected sites interacted with H with different outcomes. First, vacancy-like atoms saturated by an H atom stabilize the sp_2 hybridization and that defect stops the healing mechanism. Conversely, if sp_3-like atoms are saturated by H atoms, the lattice out-of-plane

distortions convert into stable tertiary C atoms, as shown in Fig. 5.6b and c.
In general, the simulations with H show that the reactivity of planar sp_2 carbon atoms is not zero as in the case of pristine graphene (see solid bars in Fig. 5.6d). Thus, defects in the lattice affect the reactivity of the system also at a relatively large distance from the irradiated site. The highest reactivity is shown by atoms with dangling bonds (dangling sp_2 and linear sp in Fig. 5.6d), but also curved sp_2 and sp_3-like atoms have improved reactivity. As a final remark, we point out that even when the systems were subjected to a strong chemical attack, the saturation occurred gradually and some dangling bonds are left unsaturated even after few aging cycles. These results support the similarities between the experimentally observed healing and the simulated systems in vacuum. Indeed, even in the worst case scenario (i.e., the presence of high reactive species), the evolution of defected graphene is a concurrency of the reconstruction process happening in vacuum and the creation of distorted sites that can interact with the surrounding environment and are partially responsible for the shift in nature of the defects observed in the experiment.
In summary, we demonstrated that the defects created with EBI undergo a complex evolution at room temperature in air condition. Such evolution takes place with a timescale of ~ 670 hours, after which the system stabilizes in a less defected state. This stable state is reached after a partial reconstruction of $\sim 30\%$ of the initial defects, accompanied by a local tensile strain relaxation. The observations, supported by the MD simulation, point out that graphene can rebuild its lattice without any specific healing treatment. In addition, the simulations showed that the induced defects are composite clusters of vacancies and complex amorphous C structures and not well defined nanoholes. In such systems, the vacancy-like population decreases over time due to the reconstruction and saturation of the dangling bonds, while the sp_3-like population is on average constant due to rearrangements in the lattice. Finally, the experiment, combined with simulations, highlighted that, when evolving during time, the modifications of the defected sites are a combination of self-reconstruction of the lattice and creation of reactive

sites that promote the chemical interactions in case of defects-airborne contaminant collisions. Such a process occurs on a long timescale because defects must overcome an energy barrier to recombine in the crystal [99] and the probability of collision with airborne contaminants is modest [215].

5.1.2 Patterning regular array of defected lines

To highlight how the defects can actively influence coherent transport phenomena in graphene, we chose to fabricate arrays of defected lines across the channel of graphene gFETs. Indeed, effects on transport of ballistic electrons are expected in systems where long-range order is established. However, coherent phenomena require a phase coherence length of the carriers larger than the interdistance between the lines. Consequently, the patterns must be well defined, and the defect-rich and defect-free areas must be clearly distinguished.
To this end, we investigated line gratings induced via EBI on graphene flakes as a fundamental step towards the fabrication of periodic patterns employable in transport experiments. The results of our study are reported in [216]. For this experiment, we employed exfoliated graphene supported by the standard Si/SiO_2 substrate. Before the graphene deposition, the substrate chips were cleaned with oxygen plasma (see Appendix A) to remove organic residues on the surface, as they affect the defect patterning definition [135], lowering the achievable lateral resolution.

To create an array of lines, defects were induced by EBI at 20 keV following Recipe 6 in Tab. A.1. The irradiation created arrays of lines with different geometries, as depicted in Fig. 5.7. The pattern pitch p varied from 20 nm to 100 nm. The step-size along the lines was set at 7.8 nm. We fabricated and studied two devices, named 'Set 1' and 'Set 2', fabricated using the same step to test the reproducibility of the experiment. To study the morphology of the defected pattern and its impact on the crystal properties, we employed a combination of AFM measurements and micro-Raman spectroscopy. As in the previous case, we did not measure a single point for each pattern, but rather

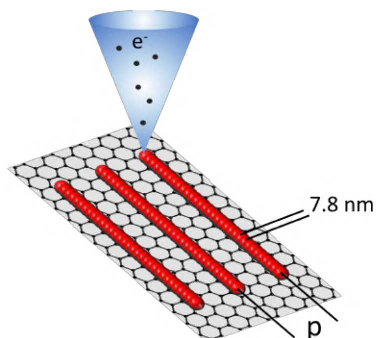

Figure 5.7 – Sketch of the electron irradiation: red spots indicate the landing points of the primary e-beam. All lines are exposed with a step size of 7.8 nm (distance between the landing points) and are separated by a distance p.

we collected mapping of the flakes to use the statistical average as experimental point and the standard deviation as the error on the measurement.

First, we studied the AFM scans on the flakes. In the maps, the patterned arrays resulted in a local increase of the measured topographic height, as shown in Fig. 5.8a. The height variation induced by the defective lines is clearly distinguishable, and shows the presence of a regular pattern of lines with pitch p = 50 nm (from Set 1). The increase in the topographic height may be attributed to the presence of contaminants adsorbed by part of the defected sites due to the exposure to ambient air [202, 217].

We extracted single profiles by averaging multiple lines of the AFM map of each pattern to quantitatively study the induced height variations. Fig. 5.8b shows clear periodic oscillations discernible for pitch p as low as 50 nm. Contrarily, the extracted line for 35 nm shows an overall height increase with respect to the non-irradiated graphene, but no regular pattern can be easily recognized. To better identify the periodicity of the observed oscillations, we performed a fast Fourier transform (FFT) on the height profiles measured on each pattern, reported in Fig. 5.8c as a function of $\Delta x = k^{-1}$ for a better comparison of the results with the pitch values. The Fourier signals for p varying from 50 nm to 100 nm exhibit a clear first harmonic peak at $\Delta x = p$ (indicated

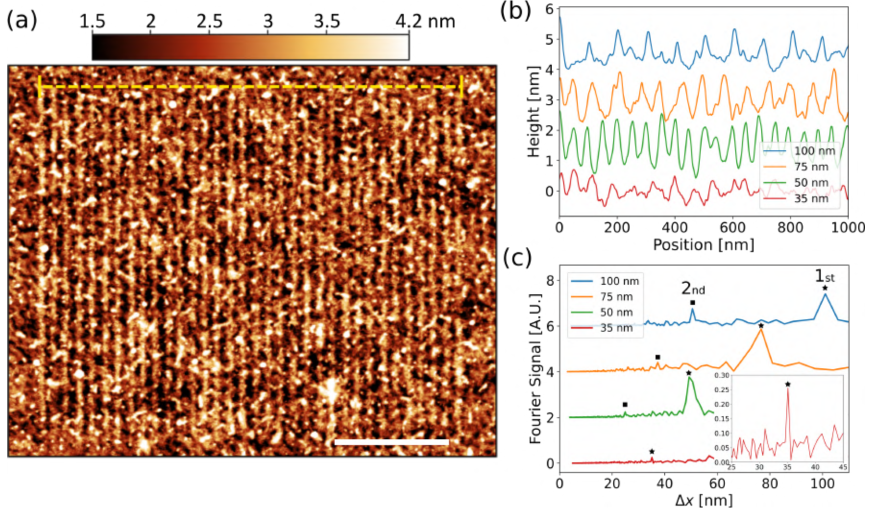

Figure 5.8 – (a) Example of topographic height map of Set 1, irradiated with a 50 nm pattern. The patterned area is highlighted by the yellow dashed line. The scale bar is 500 nm. (b) Comparison of lines extracted from AFM scans of patterns with different pitches, reported in the legend. Each line average is shifted of 1.5 nm. (c) Fast Fourier transform of the lines reported in (b). The x axis reports the inverse of the momentum $\Delta x = k^{-1}$ for a better comparison with the pitch values. First harmonic peaks are indicated as '1st' and by stars, second harmonic peaks as '2nd' and by squares. In the inset, a zoom of the FFT of the height profile for $p = 35$ nm.

with stars) and also a second harmonic peak at $\Delta x = p/2$ (indicated with squares). Notably, the FFT of the pattern with $p = 35$ nm shows a distinct first harmonic peak at $\Delta x = 35$ nm, as visible in the inset of Fig. 5.8c. These results indicate that a regular defective pattern is created on the lattice, even if the AFM profiles do not show discernible order. To explain this, we need to consider that the focused e-beam has a finite radius r_B when impinging on the target. The e-beam we employed for our studies has a radius $r_B \sim 25$ nm. When the pitch approaches the dimension of the radius ($p \sim r_B$), the profile of each line starts to overlap with the ones of the surroundings, thus diminishing the lateral resolution of the patterns.

However, the finite size of r_B also impacts patterns with pitches longer than 35 nm. Indeed, by fitting the profiles with arrays of Lorentzian

peaks to extract height and FWHM of the oscillations, we reconstructed the pitch dependency shown in Fig. 5.9. The obtained average height (i.e, the average intensity of the Lorentzians) decreases as p increases, as shown in Fig. 5.9a. This suggests that the induced defect density varies with the pitch p, resulting in an unexpected dependency of the surface chemical reactivity on p. Instead, the FWHM of the patterned lines is constant within the error at a value comparable with r_B of the employed e-beam (Fig. 5.9b). The constant width demonstrates that, even if the density of defects in the single line changes, the lateral resolution is not detrimentally affected by the patterned irradiation.
To explain the observed dependency on p of the density of defects, we must consider the interaction of electrons back-scattered by the substrate (BSEs) with adjacent lines previously irradiated. Indeed, BSEs retain most of the energy of the primary electrons and can be spread in an area of radius $r_{BSE} > r_B$, up to a few micrometers around the irradiated spot [135]. Therefore, the defects along the lines are generated mostly by the interplay of both primary and back-scattered electrons. Instead, in the areas between the lines, only BSEs can induce modifications in the lattice. BSEs are less numerous compared to primary electrons and their kinetic energy varies with the radial distance from the primary beam landing position, and therefore yield a much lower density of defects in the lattice [135]. Indeed, we observed an increase in the height within the lines, linked to the presence of surface adsorbates, but the constant width excludes the inter-diffusion

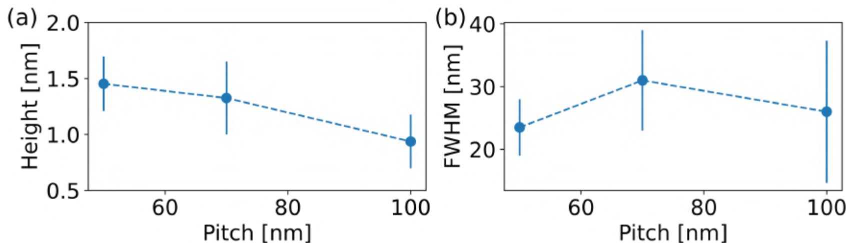

Figure 5.9 – (a) Average height (amplitude of the Lorentzian) of the peaks measured via AFM as a function of the pitch p. (b) Average FWHM of the peaks measured via AFM as a function of the pitch p. Standard deviations are used as error bars.

of adsorbates between adjacent lines. These facts combined indicate that the surface reactivity is enhanced primarily in the pattern lines, where the defect density is the highest [103]
After the AFM study, we extracted quantitative information on the induced defects by studying their impact on the crystal lattice via Raman spectroscopy. Figure 5.10 shows the averaged Raman spectra collected on each pattern and on pristine graphene. As expected, D and D' peaks appear in the spectra of irradiated graphene, as a signature of the presence of defects in the lattice (see Sec. 2.1.3). Moreover, the $2D$ peak is quenched on irradiated graphene with respect to the one measured on pristine graphene. To quantify the density of defects in the crystal, we employ the usual ratio of the intensities of the D and G peaks. $I(D)/I(G)$ increases in both Set 1 and Set 2 when the pitch of the pattern is decreased, as shown in Fig. 5.10b. By means of the Tuinstra-Koenig relation of Eq. 2.6, we computed the corresponding density of defects, shown on the right axis of Fig. 5.10b. The extracted density varies from $\sim 2 \times 10^{11}$ cm^{-2} measured for $p = 100$ nm to 5.26×10^{11} cm^{-2} for $p = 20$ nm.
An increase in the density of defects when reducing p is also confirmed

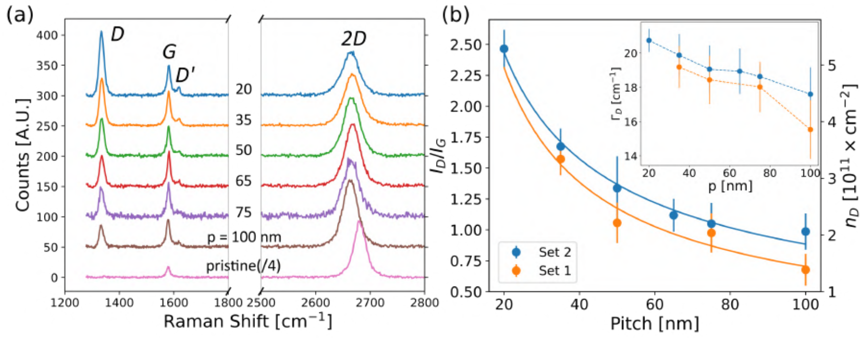

Figure 5.10 – (a) Averaged Raman spectra taken on graphene patterned with different pitches p. Each spectrum is shifted of 50 A.U. and the spectrum collected on the pristine graphene is divided by 4. (b) Plot of the ratio I_D/I_G of the intensities of the D and G peaks as a function of the pitch p of the pattern. Solid lines are the the fitting curves based on Eq. 5.2. In the inset, the width Γ_D of the D peak is plotted as a function of the pitch p. Standard deviations are used as error bars.

by the analysis of the width $\Gamma(D)$ of the D peak. Typically, the simultaneous increase of $I(D)$ and $\Gamma(D)$ is associated with an increase in the density of defects [218, 219]. Indeed, we observe a monotonic broadening of the D peak when reducing p in both Set 1 and Set 2, as shown in the inset of Fig. 5.10b. This further demonstrates that the density of defects is indeed higher for shorter pitches.

To interpret the observed p dependency of the induced defects, we consider that the EBI induces single lines of defects, which can be described by a constant linear density ρ_{sl}. However, in our Raman measurements, we address a spot much larger than the single line, and the density of defects extracted from the Tuinstra-Koenig relation is the average surface density in the measured area. Therefore, a model that links the observed surface density to ρ_{SL} is necessary to interpret our observations. To this end, we consider that in each pattern, the density of lines (i.e., lines per unit length) is the inverse of the pitch $n_L = 1/p$. Thus, the density of defects induced in the graphene sheet can be expressed as $n_D = \rho_{sl} \cdot n_L = \rho_{sl}/p$. The linear density ρ_{sl} is expected to be identical in all lines and patterns, as the same irradiation parameters are used. However, the amount of defects induced along a single line is influenced by BSEs and is not independent on the pattern pitch, as also suggested by the AFM results. Thus, we fit the experimental ratio $I(D)/I(G)$ with the function

$$\frac{I(D)}{I(G)}(p) = \frac{A}{p} \cdot \left(\frac{p}{r_{BSE}}\right)^B \tag{5.2}$$

where $r_{BSE} = 1.5$ μm is the radius of BSE for 20 keV irradiation [135] and A has the same unit of p. The values of the parameters extracted from the fit are listed in Tab. 5.3.

Set	A (nm)	B	α (10^{11} cm$^{-2} \cdot$ nm)
1	241	0.37	520
2	141	0.26	307

Table 5.3 – Fit results for the data reported in Fig. 5.10b. α is the value of A transposed in density of defects by Eq. 2.6.

In the model, we assumed $\rho_{sl} \propto p^B$ with $0 < B < 1$ to take into account the different impact of BSEs when varying the pitch. Defining α as the value of A transposed into an induced density of defect by Eq. 2.6, we obtain a term $\alpha(p/r_{BSE})^B$ that can be interpreted as the effective induced linear density of defects ρ_{sl}^{eff}. This value takes into account the effect of all electrons interacting with graphene, which can come both from the primary beam and from back-scattering events.
Lastly, we investigate how the pattern pitch influences the doping and strain of the defective graphene flakes by studying the positions of the G and $2D$ peaks. Fig. 5.11a shows the plot of the shift of the G and $2D$ peak positions with respect to their values in pristine graphene $\Delta\omega_{G,2D} = \omega_{G,2D}^{def} - \omega_{G,2D}^{0}$ for the different pitches in both Set 1 (orange dots) and Set 2 (blue dots). First, the electronic irradiation blue shifts the G peaks, indicating a moderate change in the doping [60] from $\sim 3 \times 10^{12}$ cm^{-2} in pristine graphene to $\sim 5.6 \times 10^{12}$ cm^{-2} in irradiated graphene. In addition, we observe a weak dependence on p of the doping, which went from $\sim 4.5 \times 10^{12}$ cm^{-2} for $p = 100$ nm to $\sim 6.5 \times 10^{12}$ cm^{-2} for $p = 20$ nm. Such behaviour is confirmed by the change in the difference $\Delta\Gamma_G = \Gamma_G^{def} - \Gamma_G^0$ of the width of the G peak before and

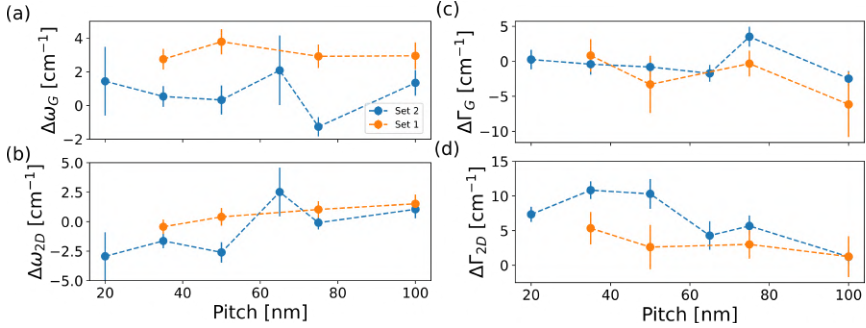

Figure 5.11 – (a-b) Change in the G and $2D$ peak positions with respect to the pristine flake as a function of the pitch p. Here, $\Delta\omega_{G,2D} = \omega_{G,2D}^{def} - \omega_{G,2D}^{0}$, where $\omega_{G,2D}^{0}$ and $\omega_{G,2D}^{def}$ are the positions of the G and $2D$ peaks before and after the irradiation, respectively. (c-d) Change in the G and $2D$ peak width with respect to the pristine flake as a function of the pitch p. Here, $\Delta\Gamma_{G,2D} = \Gamma_{G,2D}^{def} - \Gamma_{G,2D}^{0}$, where $\Gamma_{G,2D}^{0}$ and $\Gamma_{G,2D}^{def}$ are the widths of the G and $2D$ peaks before and after the irradiation, respectively. Standard deviations are used as error bars.

after the irradiation [219] reported in Fig. 5.10c. The width of the G peak in electron-irradiated graphene is determined by the competitive action of the carrier concentration, which narrows the G peak, and of the induced defects, which tend to broaden the peak. However, electron-defect scattering mainly dominates when $I(D)/I(G) \geq 3$ [218], while in our observations such ratio is always well below this threshold. In general, the local irradiation-induced increase in the charge carrier density can be attributed to the surface activation (i.e., to the presence of adsorbates) and to the interaction with the substrate [209]. Indeed, part of the observed doping can be due to the same irradiation-induced charge puddles in SiO_2 that impacted the doping in the first 10 hours of the time evolution of the EBI-induced defects (see Sec. 5.1.1, [208]). On the other hand, ω_{2D} is red-shifted and $\Delta\Gamma_{2D}$ decreases as the pitch increases (see Fig. 5.11b and d). The $2D$ peak behaviour is an indication of an increase in the tensile strain when reducing the pitch [220]. Indeed, ω_{2D} is almost independent of defect density as long as $I(D)/I(G) \leq 3$ [67, 218], whereas Γ_{2D} broadens when increasing defect density and tensile strain [63, 205]. As a result, we observed a variation of the strain with p. Indeed, in Set 1 the strain varied from $\varepsilon_1 = +0.31\%$ for $p = 100$ nm to $+0.38\%$ for $p = 20$ nm, while in Set 2 it varied from $\varepsilon_2 = +0.2\%$ for $p = 100$ nm to $+0.3\%$ at $p = 35$ nm.

In conclusion, we proved that it is possible to generate well-defined periodic arrays of defected lines with a pitch p as small as 50 nm. For lower resolutions, the impact of EBI is still visible, but the characteristic length approached the radius of the beam r_B, with detrimental effects on the long-range order of the array. When the defected line is well defined (i.e., for $p \geq 50$ nm), we found that the average width of the defective lines is comparable to the e-beam spot size. We also demonstrated an influence of the BSEs on the observed density of defects that goes beyond the simple $1/p$ dependency expected from the increasing number of lines per unit area. We provided a model which allows to extract the linear density of defects ρ_{sl}^{eff} effectively induced by the irradiation, which can help to fine tune the parameters to lower the impact of the BSEs on the achievable resolution.

So far, we demonstrated that it is possible to employ EBI at 20 keV to

generate regular defective patterns with nanometric lateral resolution which lasts for a timescale of hundreds of hours.

5.2 Transport across a periodic array of defected lines

We now discuss the results obtained by transport measurements across the same defective patterns studied in the previous section. First, we fabricated a gFET on the Si/SiO_2 substrate, referred to as FET1. We isolated graphene flakes with the exfoliation method and shaped with RIE a rectangular channel of width $w = 10$ μm and length $L_1 = 15$ μm, as shown in Fig. 5.12a. We then deposited the source S and drain D metal contacts, along with the probes used for 4W measurements (see Sec. 3.3.2). We then patterned the defective lines using Recipe 6 in Tab. A.1. As shown in Fig. 5.12b, each line goes across the whole channel, and the lines are repeated along the whole length of the channel with a pitch $p = 75$ nm. Considering that the width of the single line is $s \sim 25$ nm (see Fig. 5.9b), the interdistance between the lines is $d_1 \sim 50$ nm.

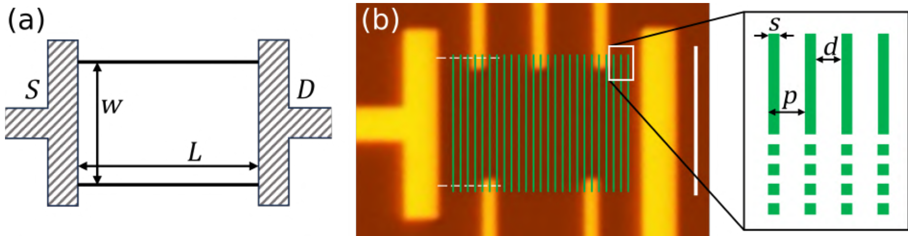

Figure 5.12 – (a) Schematics of the gFET, showing the source S and drain D electrodes. The channel is a regular rectangle of width $w = 10$ μm and length L, which varies depending on the device. (b) Optical image of FET1, in which the S and D electrodes are visible, along with the probes used for 4W measurements. The graphene channel is highlighted by the two horizontal white dashed lines. On the channel, defected lines are patterned as shown by the schematics in green. The array has a pitch $p = 75$ nm, while each line has a thickness $s = 25$ nm and is distanced $d = p - s = 50$ nm from the adjacent ones. The scalebar is 10 μm.

Therefore, the resulting device has a graphene channel with 200 lines of defects regularly repeated every p nm.
After the fabrication, we left the sample in air for 72 hours to eliminate possible influences of the charge trapped in the SiO_2 substrate (see Sec. 5.1.1). We also noticed that the observed effects arise only after the sample is left to age, pointing towards an impact on the measured systems of the interaction with contaminants and of the reconstruction process described in the above sections. Both phenomena influence the doping only on the irradiated part, thus generating more pronounced features in the channel.
The sample was then measured in the cryostat described in Sec. 3.3.2, at a base temperature of ~ 2.5 K. First, we performed 4W measurements (see Sec. 3.3.2) across the whole channel of FET1. We injected in the system a current $I_{SD} = 20$ nA between S and D. We measured the voltage drop V_{SD} between the most external probes on the channel (see Fig. 5.12b) as a function of the applied back gate potential V_{BG}. The obtained resistance R_{SD} (see Fig. 5.13a) shows the ambipolar effect typical of the gFETs. The maximum of the resistance is $R_{SD} \sim 7$ kΩ and the value of V_{BG} for which the maximum is observed is $V_D = 5.3$ V. As discussed in Sec. 2.1.2, when $V_{BG} = V_D$, the Fermi energy of graphene lies at the Dirac point, where the DoS is vanishing. Thus, for values of $V_{BG} < V_D$ (green shaded area in Fig. 5.13a), graphene is populated by holes (i.e., p-doped). Conversely, for values of $V_{BG} > V_D$ (blue shaded area in Fig. 5.13a), graphene is populated by electrons (i.e., n-doped).
The first difference with the ideal $R - V_{BG}$ curve of gFETs (transfer curve, see Fig. 2.2) is the asymmetry observed for the two regions. In general, such asymmetry can be linked to difference in the contact resistances modulated by the gate voltage [221], and a difference in the mobility of electrons and holes in the channel [222]. Although these effects are observed also in non-irradiated graphene [223], the presence of disorder in the channel enhances the asymmetry, eventually causing the suppression of the ambipolar behaviour for very high defect density [116]. The curve shown in Fig. 5.13a is measured with 4W measurements, which limit the impact of the contact resistance on the

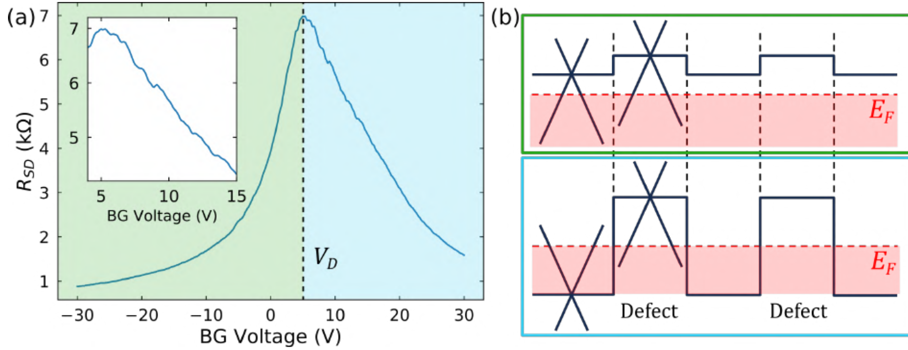

Figure 5.13 – (a) Resistance of the channel R_{SD} measured on FET1 for $I_{SD} = 20$ nA as a function of the backgate voltage V_{BG}. The vertical dashed line indicates the gate voltage for which graphene Fermi energy lies at the Dirac point V_D. The green (blue) shading indicates areas where graphene is overall p-doped (n-doped). In the inset, the detail of the curve around the Dirac point, showing the oscillating behaviour. (b) Schematics of the spatial profile of the potential experienced by the charge carriers inside the d-gFET in a p-doped channel (green square) and in a n-doped channel (blue square). The alignments of the Dirac cones are shown, and Fermi energy is indicated by E_F.

channel. Therefore, such asymmetry can be considered an effect of the e-beam irradiation of the channel.
Another deviation from the transfer curve of gFETs is the presence of remarkably regular oscillations of the resistance in the area around V_D, as shown in the inset of Fig. 5.13a. We attribute the observed oscillations to the coherent interference of electrons travelling through the periodically defected channel. Such oscillations have larger contrast when graphene is n-doped. We can explain this behaviour by considering that the irradiated areas act as diffusive barriers with a fixed p-doping (see Sec. 2.3.3 and [224]). Conversely, in the surrounding non-irradiated graphene, the transport is ballistic and the doping is influenced by the back gate. When the channel is p-doped, the junction between non-irradiated and defected graphene are $p - p^+$ junctions, as depicted in the green square of Fig. 5.13b. In this condition, the barriers are low and most of the charge carriers can travel with little influence from them, thus yielding reduced oscillation amplitudes. Conversely, when the channel is n-doped, the interfaces between non-defected and

defected areas become $n-p$ junctions (blue square in Fig. 5.13b). In this condition, oscillations are expected because of the coherent interference of the electrons moving in the ballistic cavities between the defected lines, as explained in Sec. 2.3.3.

To better study the observed oscillations, we computed the derivative of R_{SD} with respect to the back gate voltage V_{BG}, called *transresistance*. The obtained curve, shown in Fig. 5.14a, follows the trend expected from the derivative of Eq. 2.4, with a maximum below V_D and a minimum above V_D. Around this trend, clear oscillations are visible both in the p-doped region and in the n-doped region. From this graph, we can estimate the height of the p barriers created by the defected lines by the voltage V_{thr} for which the oscillations vanish in the p-doped region. Indeed, by considering the defected lines as p barriers of fixed doping, the oscillations are expected to disappear when the doping induced by the gate matches the doping of the defected lines (i.e., when the potential spatial profile is flat, see Fig. 5.13b). Following this method, we obtained a value $V_{thr} = -6.7$ V, indicated in Fig. 5.14a, which results in a distance from the Dirac point voltage $|V_{thr} - V_D| = 12$ V.

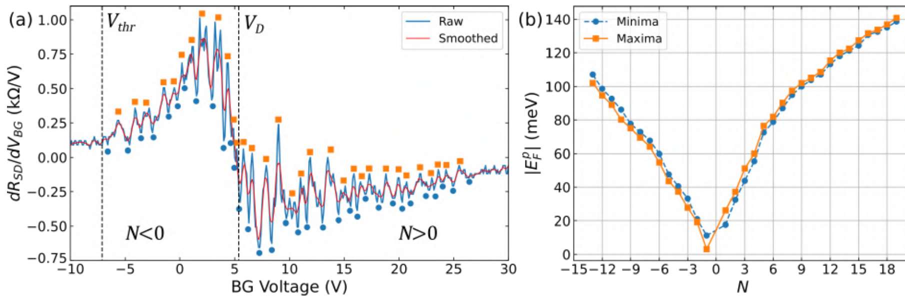

Figure 5.14 – (a) Derivative of R_{SD} with respect to V_{BG}. V_D is the voltage of the Dirac point computed from the curve in Fig. 5.13a. V_{thr} is the voltage value at which the oscillations are not visible in the p-doped region. The orange squares indicate the position of the maxima, while the blue circles indicate the position of the minima of the oscillations. Each oscillation is classified by an integer index N, chosen to be negative (positive) for oscillations in the p-doped (n-doped) region. (b) Position of each minimum (blue dots) and maximum (orange square) in Fermi energy computed with respect to the Dirac point E_F^p, plotted against the index of the oscillation.

By means of Eq. 2.2 and 2.3, we computed the energy height of the barriers as $U_{bar} \sim 100$ meV. Further studies are necessary to confirm this finding, for example Kelvin probe force microscopy.
Then, we classified the oscillation maxima and minima with an integer index N, which starts from the Dirac point and is negative (positive) for oscillations in the p-doped (n-doped) region, as shown in Fig. 5.14a. We computed the position of each oscillation in Fermi energy E_F^p by means of the same equation as the barrier heights, and plotted it as a function of the index number, as shown in Fig. 5.14b. Interestingly, the oscillations behave differently in the two regions. For $N < 0$ (p-doped region), the energy grows slower than for $N > 0$ (n-doped region). Moreover, more oscillations are visible for $N > 0$, as in this regime there is no condition in which the potential is flat, contrarily to $N < 0$. Nevertheless, for energies higher than $\sim$ 140 meV, the oscillations disappear also in the n-doped region. This is possibly explained by considering that the phase coherence length of electrons in graphene depends on the Fermi energy in the crystal. Indeed, the phase coherence is influenced by many factors, one of them being the electron-electron scattering. When increasing the Fermi energy, the DoS of charge carriers also enlarges (see Sec. 2.1). This yields a larger number of available states for the carrier-carrier scattering to happen, thus reducing the phase coherence length in the crystal without the interaction with the defects. If the phase coherence length is much shorter than the typical lengths of the system, the transport across the channel is mostly diffusive, and the contrast of the oscillations in the resistance is quenched.

5.2.1 Dependence on length

Next, we study the dependence of the observed coherent effects on the number of periods of the array. To this end, we injected a current of $I_{SD} = 20$ nA in the channel, and measured the voltage drop between electrodes at different distances. As shown in Fig. 5.15a, we tested 3 different lengths: F1, F2 and F3 (the longest one, used for the above discussions). Tab. 5.4 summarizes the lengths of the measured channels, along with the number of defective lines between the two probe electrodes N_x, $x \in \{\mathrm{F1}, \mathrm{F2}, \mathrm{F3}\}$.

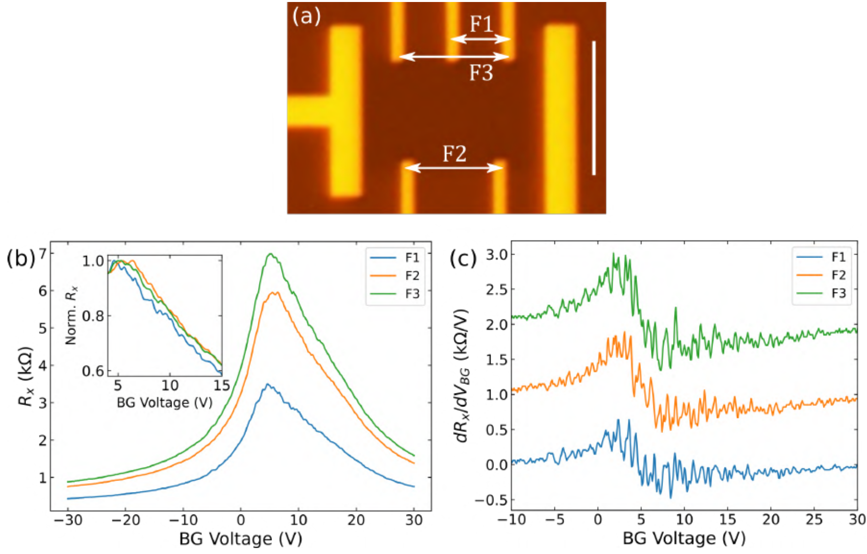

Figure 5.15 – (a) Optical image of FET1. Three different lengths were probed with 4W measurements: F1, F2 and F3. The scalebar is 10 μm. (b) Transfer curves measured for an input current $I_{SD} = 20$ nA on the three different lengths shown in (a). No shift is applied. In the inset, overlap of the resistances normalized on their relative maximum for a better comparison. (c) Transresistance curves obtained from the curves in (b). Each line is shifted vertically of 1 kΩ/V for a better comparison.

The obtained transfer curves are shown in Fig. 5.15b. The maximum resistance measured for each curve is: $R_{F1}^{max} = 3.4$ kΩ for F1, $R_{F2}^{max} = 6$ kΩ for F2, and $R_{F3}^{max} = 7$ kΩ for F3. The increase in resistance is in accordance with the expectations because of the longer channels and the increasing number of defected lines.
We compared the observed oscillation by normalizing each curve with its maximum, as shown in the inset of Fig. 5.15b. The curve measured

Channel	L_x (μm)	N_x
F1	5	67
F2	8	107
F3	10	135

Table 5.4 – Lengths L_x of the channels, along with the number of defected lines between the probes N_x.

on F1 shows oscillations with a smaller period than the other curves (see for example the interval between 7 V and 11 V). This can be an effect of the small variations in the geometrical features of the single line. Indeed, when measuring long channels, such variations average out on more periods, thus smearing the smaller oscillations into larger peaks. When analyzing the transresistances (Fig. 5.15b), we observe that the three curves show similar oscillations (e.g., repeated features are visible at $V_G = 6$ V, 12 V, 14 V), thus demonstrating that the coherent behaviour arises already for N_{F1} periods and is preserved for the whole length of the channel.
The oscillations measured on F2 show some differences with respect to the other curves, and a slightly lower contrast. This effect can be ascribed to variations of the induced defect density along a single line. F1 and F3 probe the same side of the channel, while F2 is at the other side. Since the induced lines are complex composites of different defects, also influenced by the substrate and by contaminants, it is possible that the defective pattern shows slightly non-uniform features along its width, thus yielding differences in the observed resistance oscillations. This would also result in a non-trivial transverse resistance. Therefore, magneto-transport measurements on such system could be an interesting perspective to evaluate these effects.
By looking at Fig. 5.15b, the oscillations in the p-doped region vanish for $V_{BG} = -5.7$ V in all the curves, confirming that the estimate of the height of the barriers is consistent for all lengths. Conversely, the oscillations in the n-doped region vanishes for values of the voltage which increase with the lengtt of the probed channel: $V_{max}^{F1} \sim 17.5$ V for F1, $V_{max}^{F2} \sim 21$ V for F1, and $V_{max}^{F1} = 26$ V for F1. We explain this dependency with the increased number of periods, which is expected to increase the contrast of the oscillations [152].

5.2.2 Dependence on the current bias

We now focus on the dependence on the current bias of the observed curves. We measured F3 for values of the injected current I_{SD} ranging from 20 nA to 200 nA in steps of 36 nA, as shown in Fig. 5.16a. We did not explore higher values of the bias current to preserve the channel

from possible modifications in the defect population induced by the heat generated by the current (current annealing [225]). Within this bias interval, no major difference is visible in the curves, as also shown in the inset of Fig. 5.16a. This demonstrates that the observed behaviour is robust even for a high flux of incoming electrons, and it depends very little on the current bias in the interval of observation.

5.2.3 Dependence on temperature

After the study on the bias dependence, we investigate the effects of the temperature on the system. We injected a current $I_{SD} = 20$ nA, and varied the temperature between 5 K and 30 K in steps of 2.5 K. Between each measurement, we waited 15 minutes for the complete thermalization of the device. Fig. 5.16b shows the transresistance measured along F3 for the different values of the temperature. In the inset, the transfer curves in the region of the oscillations are reported. When increasing the temperature, we observe a reduction of the oscillation contrast. We attribute this effect to the temperature dependence of the phase coherence length of electrons in graphene [226], which is lowered because of the increasing electron-electron and electron-phonon

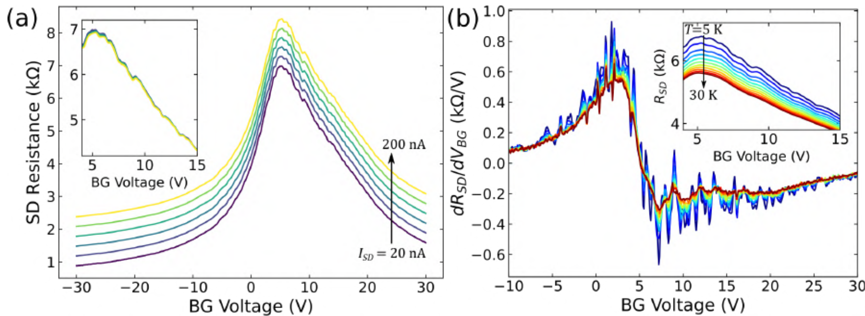

Figure 5.16 – (a) Transfer curves measured along F3 for different values of the injected current I_{SD}. The curves are shifted of 0.3 kΩ for visibility. In the inset, the same transfer curves in the region of the oscillations. The shift was removed for a better comparison of the shape. (b) Transresistance curves along F3 for different temperatures of the system T. In the inset, the corresponding transfer curve in the region of the oscillations.

interactions at high temperature. Moreover, the maximum value at which the oscillations are observed diminishes with the temperature, thus confirming the importance of the modified phase coherence length on the observed oscillations. Some residual, wide oscillations are visible even at 30 K. Finally, we repeated the thermal cycle different times and measured very little variations in the observed curves.

5.2.4 Dependence on pitch

To test the dependence of the oscillations on the pitch of the system, we fabricated a second device, referred to as FET2, with the same width $w = 10\ \mu$m but a different length $L_2 = 10\ \mu$m. We patterned on FET2 an array of lines with pitch $p = 50$ nm, resulting in an interdistance $d_2 \sim 25$ nm between adjacent lines (see Fig. 5.12b). We chose a different channel length to keep the total number of lines constant without introducing possible contribution of non-irradiated parts of the channel. We injected a current $I_{SD} = 5$ nA and measured the voltage drop along the channel. The obtained transresistance is shown in Fig. 5.17a. The position of the Dirac point is $V_{D,2} = 1.8$ V, showing that the ungated channel of FET2 is closer to the charge neutrality point with respect to FET1, for which $V_{D,1} = 5.3$ V. This can be linked to the variations obtained in the doping of different flakes obtained with the mechanical

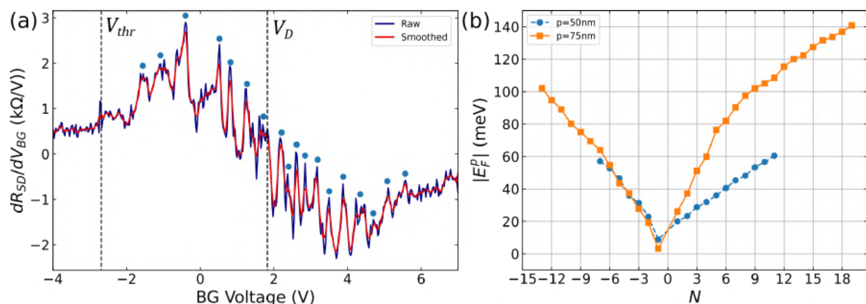

Figure 5.17 – (a) Transresistance measured along the channel of FET2 as a function of the back gate voltage V_{BG}. V_D is the position of the Dirac point and V_{thr} is the voltage at which the oscillations vanish. The blue dots indicate the maxima of the oscillations. (b) Comparison of the position E_F^p of the maxima of the peaks for FET1 ($p = 75$ nm) and FET2 ($p = 50$ nm).

exfoliation, or an effect of the different irradiated geometries, which can cause a different shift of the charge neutrality point [113].
As in FET1, the transresistance of FET2 shows clear oscillations when varying the gate voltage (Fig. 5.17a). By following the same approach adopted in FET1, we compute the height of the barriers as $U_{bar} \sim 65$ meV, which is in agreement with the value computed for FET1.
We extracted the positions of the maxima of the oscillations in the transresistance also for FET2 with the same method used for FET1. The comparison of the obtained curves is shown in Fig. 5.17b, where a dependence on the pitch is observed: the curve computed for FET1 (orange squares) is steeper than the one of FET2 (blue dots). Interestingly, the ratio of the two curves is close to 2, which is also the ratio between the interdistances d in the two samples (50 nm for FET1, 25 nm for FET2), which demonstrates that the difference in the observed oscillations can be linked to the variation of the pitch. Another explanation of the observed ratio can be the measured height of the barriers, which also influences the energy of the oscillations. Indeed, the ratio between U_{bar} computed for FET1 and FET2 is ~ 2.
Conversely, the curves are very similar for $N < 0$ (p-doped region of graphene). This can be attributed to the reduction in height of the barrier, or to complex mechanisms governing the behaviour of our system, yet to be understood.

5.2.5 Reproducibility

As a final study, we report measurements taken to test the reproducibility of the experiment. The measurements were performed on two gFETs fabricated for the Master thesis project of Simone Cassandra, from University of Pisa. The gFETs, referred to as FET3 and FET4, have width $w = 3$ μm and length $L = 5$ μm, and were irradiated with Recipe 6 in Tab. A.1 with a pitch $p = 50$ nm. Both samples where measured with 2W measurements, with an applied voltage of $V_{SD} = 200$ mV and $V_{SD} = 140$ mV for FET3 and FET4 respectively. The resulting transfer curves are shown in Fig. 5.18. No horizontal shift is applied. Both samples show very high resistance. This arises from the combination of both the small dimensions of the channel and possibly a very high

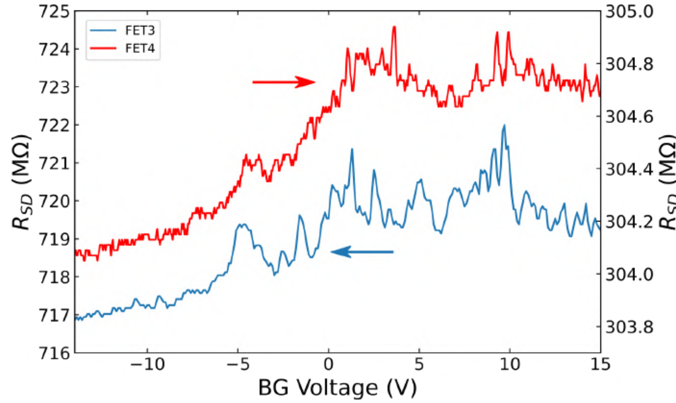

Figure 5.18 – Transfer curve taken on two different gFETs where an array of pitch $p = 50$ nm was induced via EBI. The two curves have very different baseline resistances, but the observed oscillations show nevertheless equivalent features.

contact resistance, which influences 2W measurements, as discussed in Sec. 3.3.2.

Nonetheless, oscillations in the resistance are visible in both samples. Moreover, the two curves are remarkably similar, with oscillations which can be overlapped even if the two samples were fabricated on different substrates and in different sessions of EBI. This rules out the possibility that the observed oscillations are effects of the low dimensionality of the channels or due to the low temperature of the measurements, such as universal conductance fluctuations (UCFs) [227]. Indeed, UCFs happen at random voltages for low temperature measurements, and are different from sample to sample and even from thermal cycle to thermal cycle [228]. However, even when we performed different thermal cycles on our samples or measured samples with nominal equivalent geometries, the resistance reproduced similar oscillations, as also demonstrated by Fig. 5.18. This is a further confirmation that the observed effects are due to the specific defect engineering of the channel and show reproducible trends.

5.3 Partial Conclusions

In this chapter, we focused on the properties of graphene with defective areas engineered via EBI at 20 keV.
First, we studied the time evolution of the induced defects both with Raman spectroscopy and MD simulations. We demonstrated that the defective areas are formed by a complex composite of defects of different nature, caused by the simultaneous action of the incoming electrons and the substrate supporting the graphene. Moreover, we measured a partial healing of the sample of $\sim$ 30% of the defects in a timescale of $\tau \sim 670$ h, and a consequent relaxation of the strain in the lattice. We therefore proved that the time evolution is non-trivial even when the sample is left to age in air atmosphere, and no specific procedure is performed to promote the healing. The MD simulations supported the experimental findings, showing a partial reconstruction of the defective sites of at least 30% of the distorted atoms, without the interaction with any external contaminant. Moreover, the experiments showed that, during the evolution, the defect population changes its main component, from a majority of vacancy-like defects right after the irradiation, to a majority of sp_3-like defects at the end of the evolution. The MD simulations provided an interpretation of this phenomenon as the combination of a vacancy-like population which diminishes over time as the holes are reconstructed, and a sp_3 population which is in average constant during the evolution.
Then, we studied the quality of arrays of defective lines induced by EBI on a graphene flake via AFM measurements and Raman spectroscopy. In particular, we demonstrated that our method can produce well-defined arrays with pitches p as low as 50 nm. Moreover, the average width of the line is comparable with the e-beam spot size. We also showed that for lower pitches, the finite size of the e-beam has detrimental effects on the spatial resolution of the array.
We demonstrated that the 2D density of defects induced in the crystal increased when decreasing the distances between the lines. We demonstrated that such change is not the simple $1/p$ dependence expected for the increasing density of lines, but it is rather influenced by the

electrons back-scattered by the substrate, with effects on the achievable resolution. We also provided a model that takes into account the effects of the BSEs to extract the induced effective linear density of defects ρ_{sl}^{eff}.
After demonstrating the feasibility of well-defined patterns with nanometric precision with our method, we fabricated several gFETs where the channel is a graphene flake patterned with regular arrays of defective lines. By performing transport measurements, we observed oscillations of the resistance as a function of the applied back gate voltage. By considering the defected lines as p-doped diffusive barriers with ballistic cavities in between, we linked such oscillations to coherent interference of electrons. We estimated the height of such barriers as ~ 100 meV, and showed that the oscillation positions has a non-trivial dependence on the oscillation number N. We observed an asymmetry in the positions of the oscillations for p-doped and n-doped graphene, which can also be explained by considering the defective lines as p-doped barriers. By studying the transresistance measured across different distances in the same channel, we demonstrated that the oscillations vanish at the same voltage value in the p-doped region, confirming the estimated value of the barrier height. Contrarily, in the n-doped region, the oscillations vanish for increasing voltage values when increasing the number of defected lines, showing an impact of the long-range order induced by the array.
We measured very little dependence of the oscillations on the applied SD bias in the chosen range of observation. On the other hand, the temperature smears out the oscillations by lowering the phase coherence length of the electrons. However, the oscillating behaviour is robust, and wide oscillations are visible in the transresistance even at 30 K.
Then, we showed that the observed oscillations in the n-doped regions depend on the pitch of the patterned array. The ratio of the Fermi energy position of such oscillations is compatible with the ratio of the cavities between the lines in the measured samples, confirming that the observed behaviour is linked to coherent effects induced by the arrays. The fabricated devices are complex systems, in which long-range order arises from the repetition of locally disordered features. The full

understanding of such a system would require further studies, such as magneto-transport measurements to evaluate the impact of the array on the transverse resistance, or Kelvin probe measurements to test the local change in the electronic potential profile.

Chapter 6

Conclusions and Perspectives

In this work, we presented the simulative and experimental study of different laterally structured graphene-based systems to confine both electrons and light.
Regarding light-matter interaction, we presented two systems to couple graphene PPs with ISB transitions in a single QW: the GP geometry and the AGP geometry. In the GP geometry, we proved the possibility of coherently exciting PPs in graphene with an array of metallic ridges. We studied the dependency of such modes on the pitch of the array and on the Fermi energy of graphene, confirming the theoretical predictions. Moreover, in such system we predicted a coupling strength of $g = 0.18$ with a number of involved electrons $N \approx 10^2$. We confirmed the mixed PP/ISB transition nature of the excitations by investigating the intensity of the electric fields at different frequencies. We then added a metallic substrate below the structure, and demonstrated an increase of the absorption of the cavity, eventually reaching critical coupling conditions. We then exploited the recently achieved ultra-confinement of AGP modes to design the AGP geometry, in which a coupling strength of $g = 0.11$ can be achieved with a remarkably low number of involved electrons $N \approx 10$. As in the case of GPs, adding a metallic substrate increases the absorption of the cavity. By means of our simulations, we demonstrated that both GP and AGP structures are suitable platforms to study light-matter interaction at the breakdown of the Hopfield model.

Then, we presented the experimental campaign we carried out on a SQW structure analogous to the simulated GP geometry. First, we demonstrated the ISB absorption of the QW with multipass measurements at room temperature, where we observed both $1 \rightarrow 2$ and $2 \rightarrow 3$ IBS transitions, as expected from theoretical predictions. Moreover, we performed nitrogen-temperature measurements, showing the reduction of the intensity of the $2 \rightarrow 3$ transitions and a narrowing of the $1 \rightarrow 2$ line. Both results are in accordance with the lowered thermal population of the second subband.
Afterwards, we optimized the fabrication of metallic array of squares on the SQW surface, showing the successful realization of regular arrays of squares with pitches of 500 nm and 370 nm, with areas large enough to be measured with the μFTIR.
Then, we were able to detect the ISB transition by measuring at the μFTIR the fabricated GP geometry. By combining FTIR measurements and Raman spectroscopy, we determined the presence of PMMA residues on the surface of our sample, left from the fabrication. The detrimental contribution of such residues was ruled out by a proper normalization, showing the clear absorption of the QW with a maximum contrast of $\sim 7\%$ of the baseline signal. Moreover, the impact of graphene was isolated as an enhancement of the ISB absorption of $\sim 1.5\%$ of the measured signal.
Finally, we exploited a thin film of a PMMA-embedded ionic liquid that we developed to modify the carrier concentration in the graphene sheet in the fabricated system. We observed the reflectance as a function of the applied gate voltage, and measured a change in the contrast of the ISB transition of $\sim 0.3\%$, also predicted by our simulations. The obtained results is a signature of the weak coupling between the QW and the graphene PPs.
To further study such systems and confirm our findings, the metal-insulator-metal cavity we proposed can be used to enhance the contrast of the features under examination, thus reducing the impact of noise. Another possibility is to employ arrays of nanoridges milled by focused ion beam (FIB) and transferred on the sample. This would both eliminate the detrimental effects of the fabrication via EBL (PMMA residues

and possible damage to the graphene lattice, see discussion in Sec. 4.2.3), and also offer a better metal-graphene interface than the one generated with the thermal deposition of metals. We already started working towards this direction in collaboration with Dr. Andrea Ottomaniello from IIT, in the group of Dr. Virgilio Mattoli in Pontedera. To test the interaction of graphene with such metal lattices, we transferred milled patterns on top of a GaAs substrate with CVD graphene on top. We obtained promising preliminary results in the measured reflectance, which features a sharp resonance possibly linked to PPs in graphene and much less polimeric residues.
Moreover, even if strong coupling was not reached, the proposed platform could be employed for the exploration of the weak coupling regime between ISB transitions and PPs. Such regime would imply the breakdown of the dipole approximation, with non-trivial impact on light-matter interaction in the system (asymmetries in absorption/emission of light and excitation of transitions prohibited by the dipole selection rules, as reported in Sec. 2.2.3).
Finally, it would also be interesting to experimentally realize the proposed AGP structure, in which the extreme energy density granted by the ultra-confined acoustic graphene plasmon would help towards the observation of the strong coupling regime. Reaching control over such interesting platforms would allow advancements in our understanding of light interaction with only a few electrons. Moreover, the tunability of the PPs would grant the possibility of exploring different coupling regimes on a single device, thus unlocking a powerful knob for building versatile devices for photodetection or light emission.
In the second part of the work we studied the coherent effects on transport in arrays of defected lines induced in graphene channels with EBI at 20 keV.
First, we studied the time evolution of the induced defects both with Raman spectroscopy and MD simulations. We measured a partial healing of the sample of $\sim 30\%$ of the defects in a timescale of $\tau \sim 670$ h, and a consequent relaxation of the strain in the lattice that eventually involves both the irradiated and non-irradiated parts of the crystal. We therefore proved that the time evolution is non-trivial even when the

sample is left to age in air atmosphere, and no specific procedure is performed to promote the healing. The simulations supported the experimental findings, showing a partial reconstruction of the defective sites of at least 30% of the initially distorted atoms in vacuum, without the interaction with any external contaminant. Moreover, the experiments showed that, during the evolution, the defect population changes its main component, from a majority of vacancy-like defects right after the irradiation, to a majority of sp_3-like defects at the end of the evolution. The MD simulations provided an interpretation of this phenomenon as the combination of a vacancy-like population which diminishes over time as the holes are reconstructed, and a sp_3 population which is in average constant during the evolution.
Then, we studied the quality of arrays of defective lines induced by EBI on a graphene flake via AFM measurements and Raman spectroscopy. In particular, we demonstrated that our method can produce well-defined arrays with pitches p as low as 50 nm. Moreover, the average width of the line is comparable with the e-beam spot size, demonstrating the high spatial resolution of the patterned array. We also showed that for lower pitches, the finite size of the e-beam impacts on the definition of the array. Even if the spatial resolution is lower, we found by means of FFT analysis that signatures of induced long-range order are nonetheless present also for $p = 35$ nm.
Moreover, we demonstrated that the 2D density of defects induced in the crystal depends on the pitch. We demonstrated that such change is not a simple $1/p$ dependency, as expected because of the reduced distance between the lines, but rather, it is influenced by back-scattered electrons. This affects the achievable resolution, as the modifications of the effective delivered dose can be important. To solve this issue, we provided a model that takes into account the effects of the BSEs to extract the induced effective linear density of defects ρ_{sl}^{eff}.
We then performed electrical measurements across such defective patterns, and reported regular oscillations in the transfer curve of the gFETs. We explained such oscillations as a result of the coherent interference of electrons in ballistic cavities in between p-doped diffusive barriers (i.e., the defected lines). We estimated the height of such bar-

riers as $\sim$ 100 meV, corresponding to the vanishing voltage of the oscillations measured in p-doped graphene. Moreover, classified the oscillations with an integer number N starting from the Dirac point, and showed how the observed energy of the oscillation is proportional to $\sqrt{N}$. The position of the oscillations for p-doped and n-doped graphene showed different dependency on the pitch, which can also be explained by considering the defective lines as p-doped barriers.
Furthermore, by studying the transresistance curves measured across different distances in the same channel, we demonstrated that the oscillations vanish at the same voltage value in the p-doped region. This proves that the employed method for estimating the height of the barriers is valid. On the contrary, the oscillations in the n-doped region vanish for increasing voltage values when increasing the number of defected lines. We consider this as a signature of coherence across the long-range order induced by the array.
Then, we measured the oscillations as a function of the applied current bias. We did not observe any remarkable difference in the range chosen. On the other hand, we measured the system as a function of the temperature, and observed that when the temperature is increased, the oscillations are smeared out due to the lowered phase coherence length of the electrons, but are visible until at least 30 K.
Finally, we measured a second system in which we induced an array with a different pitch. On this second sample, we measured a height of the barrier of 65 meV, comparable to the one measured on the first sample, also considering possible random variations of the EBI and the influence of the pitch on the quality of the irradiation. By comparing the measurements on the two samples, we demonstrated that the oscillations position in the p-doped region does not depend on the pitch of the array. On the contrary, the oscillations in the n-doped region of the curve show a pitch dependency. Indeed, the ratio of the Fermi energy position of such oscillations is compatible with the ratio of the cavities between the lines in the measured samples. This result confirms that the observed behaviour is linked to coherent effects induced by long-range order of the arrays. All the observed phenomena point towards the creation of an array of defected lines that act as regularly repeated

potential barriers. For a complete rationalization of the system, our observations need the support of a theoretical model. To this end, we are currently collaborating with Prof. Massimo Macucci and Dr. Paolo Marconcini from Dipartimento di Ingegneria dell'Informazione of Università di Pisa, who are simulating the transport properties of systems analogous to the ones measured. The preliminary results obtained so far corroborates the proposed interpretation of the creation of potential barriers with gaussian profiles. If the simulations confirmed our findings, an interesting development could be to try and confine the electrons in two dimensions, possibly creating quantum dots in a deterministic fashion, with interesting applications in the study of the single electron regime.

The fabricated devices are complex systems, in which long-range order arises from the repetition of locally disordered features. The full understanding of such a system would require further studies, such as magneto-transport measurements to evaluate the impact of the array on the transverse resistance, or Kelvin probe measurements to test the local change in the electronic potential profile. Scanning Tunnel Microscopy would also be useful to directly test the morphological conformation of the defected sites at the atomic scale.

In conclusion, we studied two different systems in which coherent effects of the electron liquid in graphene can be exploited to enhance the properties of the system. The proposed systems are prototypical platforms to study the interaction between light and matter in a mixed 2D/bulk heterostructure, and the quantum properties of the electron liquid without the need of cumbersome fabrication. We believe that our studies on the light-matter interaction mediated by graphene are first promising steps towards the creation of an efficient platform to observe the strong coupling in the few electrons regime. Moreover, the remarkable observation of coherent effects in a structure where long-range order was created by nanometric defects in the lattice pave the way towards applications of defect engineering in the study of phenomena analogous to optics, such as electronic interferometry and other collective effects of the relativistic electron liquid in graphene.

Appendix A

Fabrication Recipes

In the following section, all the recipes used in the fabrication are listed along with the names used in the main text. For all the recipes, acetone will be referred to as ACE and isopropyl alcohol as IPA. Any variation of the following recipes is explicitly indicated in the corresponding discussion.

A.1 General procedures

Standard cleaning The standard cleaning procedure is used for all type of solid samples (e.g. wafer, glass slides). The steps are the following:

1. 2 minutes bath in ACE;
2. 2 minutes bath in IPA;
3. Blow with N_2 gun until dry.

Deep cleaning The deep cleaning procedure is used for all type of solid samples that have been in contact with polymeric resists (typically PMMA) and/or have organic residues. The steps are the following:

1. 15 minutes bath in AR 600-71;
2. 2 minutes bath in ACE;
3. 2 minutes bath in IPA;
4. Blow with N_2 gun until dry.

Step 1 can be prolonged if needed.

Spin coating for EBL This is the procedure used to spin coat polymeric resist for electron beam lithography. If not specified, the resist used is AR-P 679.04 from AllResist.

1. Standard cleaning procedure;
2. AR-P 679.04 drop casted on the sample;
3. Sample spinned in 2 steps:
   - 500 rpm for 5 seconds;
   - 4000 rpm for 60 seconds;
4. Baking on a hot plate at 160 °C for 3 minutes

Resist develop after EBL This is the recipe used to develop the exposed polymer resist after the lithography.

1. 2 minutes bath in AR 600-56;
2. 2 minutes bath in IPA to stop the develop;
3. Blow with N_2 gun until dry.

Lift-off This procedure is used to remove the polymeric mask after the sample has been covered with a metallic film via thermal evaporation

1. 2 hours bath in ACE to let the solvent seep in the fine details;
2. ACE spray with syringe to remove the lifted metallic film;
3. 5 minutes bath in IPA;
4. Blow with N_2 gun until dry.

Before further step of fabrication, the sample is usually cleaned with standard cleaning.

Oxygen plasma cleaning The oxygen plasma cleaning is used to remove organic residues from the surface of the substrates. The samples are cleaned for 5 minutes with plasma generated at 100 W.

Graphene etch Graphene is etched in the RIE chamber with the following parameters:

- Gas mixture: 5 sccm N_2, 80 sccm O_2
- Pressure: $\sim 10^{-1}$ mbar
- Bias voltage: 135 V
- RF power: 35 W
- Duration: 50 s

A.2 EBL recipes

In the table on the following page, the recipes employed for various expositions at the EBL are listed. Two kinds of expositions are used in our work: area exposition, in which the beam is scanned dot by dot to deliver a uniform dose on a selected area, and line exposition, in which the beam is scanned along one-dimensional lines.

N	Name	V (keV)	Ap (μm)	I_p (nA)	D (μC/cm^2)	WF (μm)	SS (nm)
Area exposition							
1	Markers	10	60	0.499	160	500	101.4
2	Fine detail	20	10	0.03	285	500	7.8
3	Coarse detail	20	120	3.36	330	500	101.4
4	Metal arrays	20	10	0.03	180	500	7.8
5	Area defects	20	20	0.1	$40 \times 10^3 \star$	500	7.8
Line exposition							
6	Line defects	20	20	0.1	$31.2 \times 10^3 \star$	500	7.8

Table A.1 – Recipes for EBL exposition. N is the number of the recipe, V is the accelerating voltage, Ap is the aperture, I_p is the measured beam current, D is the target dose (in unit of delivered charge per unit area/line), WF is the employed writefield and SS is the size of the scanning step. The values indicated with $\star$ can vary for different defect yield. Values different from the one listed are specified in the corresponding discussion.

Appendix B

Optical grade thin film electrolytes

B.1 Transparency and gating efficiency

As discussed in Sec. 4.2.3, back gating the heterostructure we used in our experiment presents different critical issues that strongly hinder its feasibility. To overcome such issues, we decided to employ ionic liquid gating. Indeed, as explained in Sec. 2.1.2, ionic liquids can be employed without any restriction of substrate and gating geometry, as they are conformable and intrinsically not conductive within specific voltage intervals, called electrochemical windows. In addition to these features, we also needed a ionic liquid which could be employed in optical experiments, i.e., with low absorption in the region of interest between 800 cm^{-1} and 4000 cm^{-1}. However, most commercially available compounds exhibit poor transparency in the IR region and high reactivity with the surrounding environment [229–231].
For these reasons, we developed and studied two PMMA-embedded liquid electrolytes based on bromide in collaboration with the Ionic Liquid Group, lead by Christian Silvio Pomelli at the Department of Pharmacy of the University of Pisa. The results of our study were published in [199]. We chose bromide-based electrolytes because of their electrochemical stability and polymer compatibility [232, 233]. The liquids were embedded in PMMA to enable the spin coating of thin

films, which offer a better optical interface with respect to the round droplet obtained by drop-casting of the pure liquid.
First, we studied the IR optical properties and transport properties of two pure bromide-based ionic liquids (ES1 and ES2). ES1 is commercially-available tetraoctylphosphonium bromide [$P(C8)_4Br$], while ES2 is 3,3'-(hexane-1,6-diyl)bis(1-methyl-1*H*-imidazolium)bromide [$C_6(MIM)_2/2Br$ 3C6 Br]. ES2 was synthesized using the standard ionic liquid synthesis procedure [234] adapted for dicationic ionic liquids [233].
To determine the IR optical properties of ES1 and ES2, two solid samples of the ILs were measured in a FTIR spectroscope with the ATR method (see Sec. 3.2.2). The measured absorbance spectrum of ES1 (blue solid line in Fig. B.1a) shows an absorbance generally lower than 0.1 μm^{-1} in the range from 600 cm^{-1} to 2500 cm^{-1}, except for one sharp feature of ~ 0.12 μm^{-1} at 1490 cm^{-1}. Higher absorbance

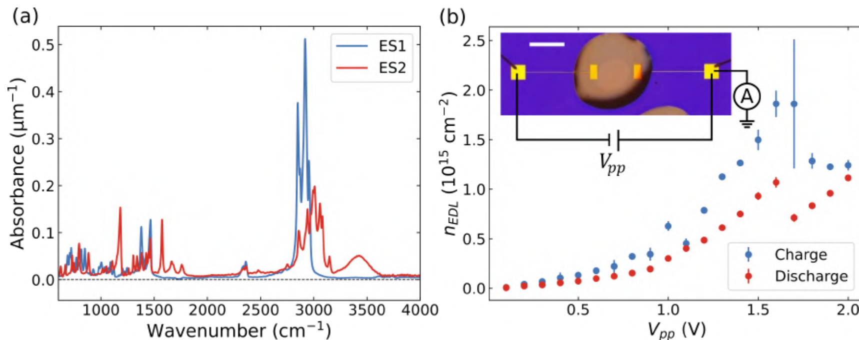

Figure B.1 – (a) Absorbance spectra of ES1 (blue solid line) and ES2 (red dashed line). (b) Charging (n^{ch}_{EDL}, blue dots) and discharging (n^{dch}_{EDL}, red dots) carrier density accumulated in the EDL in a drop of ES1 versus V_{pp}. Inset: optical image of the IL droplet on the metal pads employed for the transport measurements along with the experimental setup. The scalebar is 500 μm. (c) Optical image of a pristine Cr/Au electrode. Area 1 is covered with a PMMA film, Area 2 is exposed to air and will be in direct contact with ES1. The scalebar is 100 μm. (d) SEM image of the same electrode after the cycles of measurement in ambient conditions. The scalebar is 100 μm. (e) Detail of a region between Area 1 and Area 2 (blue dotted square in (d)). The scalebar is 1 μm. (f) Detail of Area 2 (red dashed square in (d)). The scalebar is 5 μm.

peaks close to 0.5 μm^{-1} are visible below 3000 cm^{-1}. These peaks are attributed to the stretching vibrations of the $C_{sp3} - H_{x=1,2,3}$ groups present in tetraoctylphosphonium bromide [235]. Conversely, the absorbance spectrum of ES2 (red dashed line in Fig. B.1a) shows more structured peaks up to 0.16 μm^{-1} in the region from 600 cm^{-1} to 2500 cm^{-1} and peaks around 3000 cm^{-1} lower with respect to ES1. These differences stem from the different cationic moiety of ES2, thus from the vibration modes of the imidazolium ring and from the stretching vabriation of the shorter aliphatic chain and of the $C_{sp2} - H$, respectively [236]. In both spectra, the peaks around 2350 cm^{-1} are due to the absorption of CO_2 in the atmosphere and are not related to the ILs.

We then focused on the ionic transport properties of ES1. To this scope, we fabricated metallic electrodes on the standard Si/SiO_2 substrate via EBL and thermal deposition of 7 nm of chromium and 50 nm of gold (see the inset of Fig. B.1b). The transport properties of pure ES1 were investigated by Double Step Chronocoulometry [237] (DSC, see Sec. B.2) in ambient conditions. The charge accumulated in the EDL (Q_{EDL}) was determined both during its charging (*ch*) and discharging (*dch*) during two consecutive cycles. The two sets were averaged, their semi-dispersion used as error. Then, the values of Q_{EDL} were divided by the electrode area and by the electronic charge to extract the charge carrier density accumulated in (removed from) the EDL, i.e. n_{EDL}^{ch} (n_{EDL}^{dch}). Figure B.1b reports n_{EDL}^{ch} and n_{EDL}^{dch} as a function of the applied potential (V_{pp}) for ES1 in air. The accumulated charge density grows with V_{pp} until reaching a value of $\sim 1.8 \times 10^{15}$ cm^{-2} for $V_{pp} = 1.6$ V. For larger V_{pp}, the accumulated charge decreases. Such behaviour is the result of the electrochemical activity of the system. To confirm this, we performed cyclic voltammetry (CV, see Sec. B.2) measurements to determine the electrochemical windows of ES1. The results for both measurements in vacuum and in air are shown in Fig. B.2. The observed difference between the two curves is mostly due to the presence of water in the atmosphere. The upper limit of the electrochemical window [238] of ES1 is ~ 1.25 V when measured in air and ~ 1.8 V when in vacuum. When the applied voltage exceeds

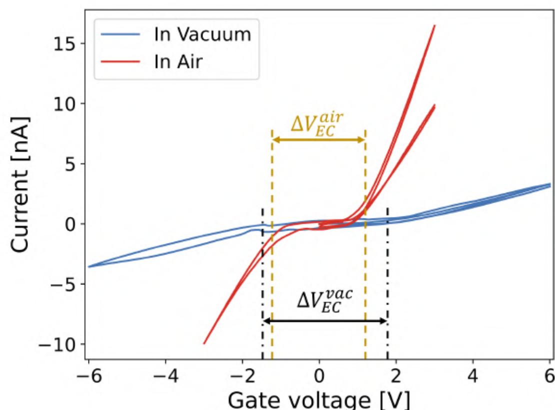

Figure B.2 – CV measurements on a ES1 drop on metallic pads in air (red curve) and in vacuum (blue curve). ΔV_{EC}^{x} is the electrochemical window of the liquid in air ($x = air$) and in vacuum ($x = vac$), respectively.

such value, reduction/oxidation reactions start to take place at the interface between the liquid and the electrodes [239, 240], thus changing the ionic current and effectively reducing the charge accumulated in the EDL. Moreover, water from the atmosphere can dissolve in ES1. When applying a voltage bias, the absorbed water reacts with the bromide in the IL forming an acid environment [241]. Consequently, part of the Br^- anions involved in these reactions do not participate to the charging of the EDL. The electrochemical activity of the liquid generates a difference between the charging and the discharging of the EDL (red dots in Fig. B.1b). In particular, $Q_{EDL}^{ch} \sim 1.7 Q_{EDL}^{dch}$ for all values of $V_{pp} < 1.6$ V. This asymmetry can be partially linked to the mobility of the ions in the IL [242]. Indeed, the ions must overcome a barrier before starting to drift in the liquid. The applied bias both gives energy for the ions to exit the potential well and lowers the barrier to overcome [243, 244]. When the potential is removed, the restored barrier yields lower charge removed in the same amount of time. The largest difference is observed for $V_{pp} = 1.7$ V, just above the electrochemical window limit. The anomalous error is attributed to a large difference between the two measurements for this bias value, indicating the onset of the electrochemical interactions. After this threshold, the asymmetry

lowers as the voltage is increased because the reactions are less likely to occur in the discharge phase. This behaviour suggests that, when the applied voltage is larger than the electrochemical barrier for the interaction, the change in the ionic mobility has in fact minor effects with respect to the chemical reactions.

To better understand the interaction between the liquid and the electrodes, the experiment was repeated on a device with electrodes partially covered by a PMMA with opening fabricated by EBL (see Fig. B.3a). After the transport measurements, ES1 and the PMMA mask were removed with acetone and the electrodes observed under a scanning electron microscope (SEM). The contrast between the two regions shows that the morphology of the metallic film that was in contact with ES1 is dramatically different from the one of the masked metal (see Fig. B.3b), thus confirming that the ionic liquid chemically interacted with the electrodes. In addition, a 10-μm-wide transitional region is visible, due to the IL diffusion below the PMMA mask (see Fig. B.3c). In the region exposed to ES1, the overall roughness is increased and holes are present in the metallic film (see Fig. B.3d). Such observation suggests that the electrochemically formed bromide-based acids attack the electrodes when applying a voltage. Indeed, the inter-

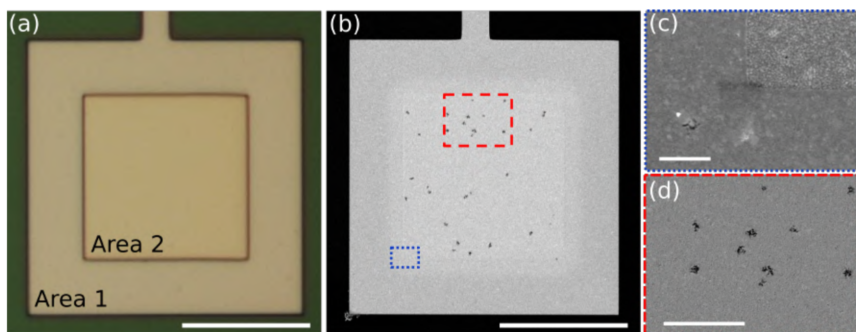

Figure B.3 – (a) Optical image of a pristine Cr/Au electrode. Area 1 is covered with a PMMA film, Area 2 is exposed to air and will be in direct contact with ES1. The scalebar is 100 μm. (b) SEM image of the same electrode after the cycles of measurement in ambient conditions. The scalebar is 100 μm. (c) Detail of a region between Area 1 and Area 2 (blue dotted square in (b)). The scalebar is 1 μm. (d) Detail of Area 2 (red dashed square in (b)). The scalebar is 5 μm.

action of bromide with water absorbed from the atmosphere can create hypobromous acid (HOBr) and hydrobromic acid (HBr) [245]. Both acids attack gold [246], thus degrading the electrodes and reducing the gating effectiveness of the liquid. As a consequence, when voltages are applied to the liquid in ambient atmosphere, electrochemical reactions happen also within the electrochemical window. However, when water is removed from the liquid, the electrochemical window widens and such reactions are avoided (see Fig. B.2).

Since PMMA can absorb only a small amount of water ($\sim 2\%$ w/w, [247]), we exploit it to embed the bromide-based ILs and prevent the creation of an acid environment destructive for the devices. Furthermore, a spin-coated electrolyte thin film improves the device optical properties thanks to its lower thickness and higher flatness. Therefore, we investigated both the optical and charge transport properties of the ILs when embedded in the PMMA matrix. To this scope we synthesised two polymer electrolytes (PES1 and PES2) starting from ES1 and ES2. PES1 is produced by dissolving 4.30 mg of ES1 in 430 mg of AR 679.04 950K (ethyl lactate solution of PMMA 950K at 4%, AllResist), while PES2 is realized by dissolving 6.10 mg of ES2 in 612 mg of AR 679.04 950K. Both solutions are therefore 25% mg IL/mg PMMA. To demonstrate the suitability of PESs in optical experiments, we measured the optical transmission of a structure composed by a PES film spin coated onto Si/SiO_2 substrates (spin coating procedure in Appendix A, soft baked at 100 °C for 2 minutes). The thickness of the obtained film is $\sim$ 290 nm for both materials.

In general, the $PES/SiO_2/Si$ transmission spectra show a reduction of the transmitted power of $\sim 5-10\%$ with respect to the bare substrate (see Fig. B.4). This reduction is due to the absorption in the film and to reflection effects caused by the air/PES and PES/SiO_2 interfaces. The baseline is also influenced by thin film effects [248], visible as a downward bending in the higher region of the spectra. Transmission dips related to PESs are present in the region 1200-1800 cm^{-1} . These lines are mainly attributed to the deformation vibrations of the $(O)CH_3$ and ester groups in the PMMA film [249] and are very similar for both PES1 and PES2. Instead, the two spectra differ in the region close to

3000 cm^{-1}, where the resonances are originated by the strain vibration of $CH_{x=1,2,3}$ groups [250]. Thus, the reduced transmission in the PESs film can be attributed to the different distribution of the $CH_{x=1,2,3}$ groups in the films due to the presence of the ESs. Nevertheless, the general features of the transmission spectrum of the bare substrate are preserved, such as the characteristic SiO_2 phonons at 1084 cm^{-1} and 1256 cm^{-1} [251] see inset of Fig. B.4).

Generally, the charge transport properties of the electrolytes are modified when they are embedded in a polymer matrix [252–256] especially when they are in form of a thin film [244]. Indeed, the ionic transport is mediated by large molecules that migrate through the polymeric matrix. For example, amorphous polymers offer larger inter-molecular cavities for ions migration with respect to ordered polymers [257]. The dimension of inter-molecular cavities is also influenced by ion size [258] and by the employed solvent [259]. To test the suitability of our polymer electrolytes as gating materials, we performed DSC experiments on both PES1 and PES2. In the form of a thin film, PES1 showed a poor ionic transport due to the dimension and 3D structure of its cation, thus we focused on PES2. Figure B.5a shows the charge density accumulated in the EDL formed by a PES2 film as a function of the applied voltage V_{pp} both in ambient and vacuum conditions. In ambient conditions, the

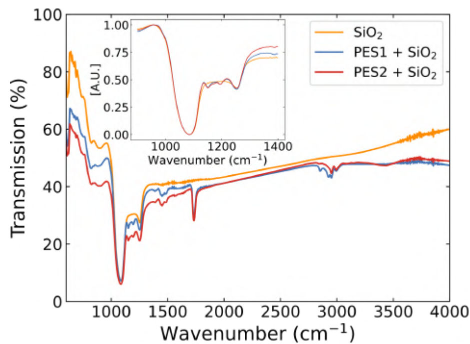

Figure B.4 – Transmission spectrum of a Si/SiO_2 chip (orange line) compared to the transmission of the same substrate with PES1 (blue line) and PES2 (red line) on top. Inset: zoom of the signals in the region around the SiO_2 phonons. The minima were shifted to 0 and the signals normalized on their maxima for a better comparison of the shape.

accumulated charge density reaches up to 2×10^{15} cm^{-2} for positive voltages and 4×10^{15} cm^{-2} for negative voltages (blue dots in Fig. B.5a). A nominally identical sample was investigated in vacuum at a pressure of $\sim 10^{-5}$ mbar (red dots in Fig. B.5a). The accumulated charge density is much higher in vacuum than in air pressure: $n^{vac}_{EDL}/n^{air}_{EDL} \sim 19.7$ for $V_{pp} = 0.5$ V and ~ 8.6 for $V_{pp} = -0.5$ V. The higher accumulated charge density in vacuum is attributed to the increased ion mobility as a consequence of two concurring factors. First, when PSEs are in vacuum, contaminant gaseous molecules such as water are expelled from the material. Second, the reduced pressure on the surface allows for the structure to relax, thus creating wider paths for ions to migrate. The asymmetry measured for positive and negative values of the applied potential in vacuum can be attributed to the different nature of the anion and the cation, both in terms of chemistry, for example, the distinct tendency to share or not electrons (thus lowering or not the potential barrier for their diffusion [243]), and in terms of dimensions; in

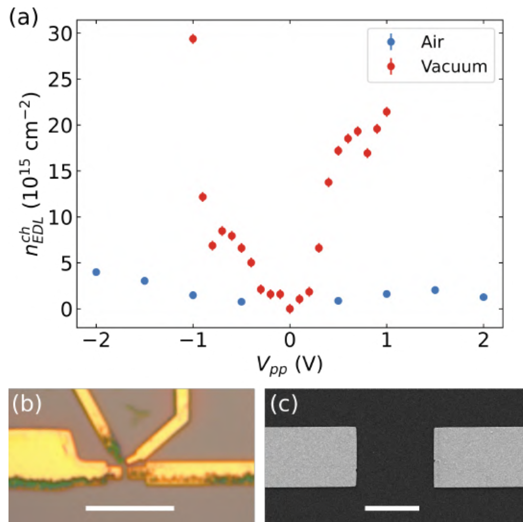

Figure B.5 – (a) Charge density accumulated in the EDLs in PES2 when in ambient conditions (blue) and vacuum (orange) versus V_{pp}. (b) Optical image of the metallic electrodes employed for the measurement in ambient conditions. The scalebar is 5 μm. (c) SEM image of the metallic electrodes employed for measurement in vacuum. The scalebar is 10 μm.

fact, the molecular mass and the volume influence the ion stability once a potential is applied (i.e. the selected anions are lighter and smaller than cations) and its ability to move across the polymer matrix [229]. Similarly to pure ES1 (see Fig. B.1b), the induced charge density grows following a monotonic trend until $|V_{pp}| \sim 0.9$ V. After that threshold, the ions in the electrolyte start interacting with the polymer matrix and the electrodes, thus modifying the EDL charging efficiency.
Despite the IL being embedded in PMMA, an acid environment is created when applying a DC bias to PES2 in ambient conditions, as measured for bare ES1 (see Fig. B.3c-f). This acid environment modifies the morphology of the device electrodes, as clearly observable in Fig. B.5b. Conversely, when PES2 is measured in vacuum, the electrodes are preserved from electrochemical damaging (Fig. B.5c). This indicates the small amount of water trapped by the PMMA film in ambient conditions is sufficient to create HOBr and/or HBr. Instead, in vacuum, the film expels most of the absorbed water, thus preventing the formation of the acid environment. After removing the water by keeping the device in vacuum, we test the stability of the PES structure by performing consecutive DSC cycles with a fixed $V_{pp} = 300$ mV in ambient conditions. As shown in Fig. B.6a, the accumulated charge density n^N_{EDL} is highly stable for the first 6 cycles. Here, n^N_{EDL} is the accumulated charge density at cycle N normalized by the carrier concentration accumulated during the first cycle. After these cycles, n^N_{EDL} increases of a factor ~ 1.3. This increase can be tentatively explained by considering that, when the polymer is brought back at air conditions, the reduction of polymer film volume caused by the air pressure leads to a decrease of the the paths for the ions migration. Consequently, during the first few cycles, the ions are pushed through the polymer matrix and open back accessible paths for the charge migration. As a result, the charge accumulated in the EDL increases after a few cycles, as similarly occurs for lithium intercalation in bilayer graphene [260, 261]. It is worth to notice that, differently from previous experiments, the applied potential does not damage the electrodes, as shown in Fig. B.6b. Interestingly, the macroscopic morphology of the PES2 film changes after the application of voltages in ambient conditions after

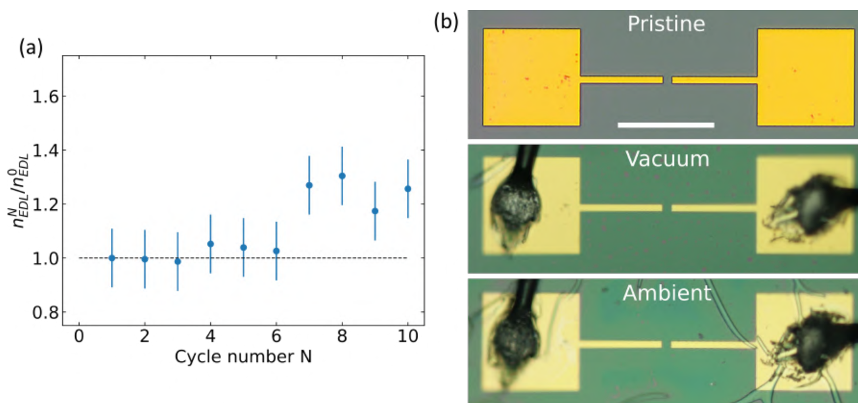

Figure B.6 – (a) Charge density accumulated in consecutive cycles performed on PES2 in ambient conditions at $V_{pp} = 300$ mV after the measurements in vacuum. (b) Optical images of the metallic pads used in the chronocoulometry measurements before PES2 is spinned (top), after the measurement in vacuum (middle) and after the measurement in air (bottom). The scalebar is 150 μm. The bonding wires used for electrical measurements are visible on the gold pads in the middle and bottom images.

the vacuum treatment. Indeed, bias-induced cracks appear over the surface of the polymer, mainly starting from points where the film was already damaged, such as near the bonding wires or metallic residues, (see Fig. B.6b). Indeed, the water molecules can efficiently penetrate into the PMMA film from these points. Within these cracks, Br- based acids can be electrochemically created and gradually diffuse through the polymer matrix. In full agreement with the DSC measurements, Fig. B.6b shows that even when the cracks are formed, the electrodes are not degraded, suggesting that negligible chemical interactions took place. Therefore, removing the water content from the polymer matrix before any voltage is applied enhances the robustness of polymer-embedded ionic liquids. Indeed, a simple treatment in vacuum preparation ensures a large stability of the accumulated charge density and prevents the formation of an acid environment in the proximity of the metallic electrodes even when employed for several cycles in air. In summary, we proposed and demonstrated the optical and transport properties of a class of polymer-embedded ionic liquids based on bromide. The EDLs

that form when the films are polarized can accumulate state-of-the-art charge densities up to $\sim 20 \times 10^{15}$ cm^{-2} in vacuum [262]. Furthermore, these electrolytes are transparent in the mid-infrared region of the spectrum and can be easily spin coated in the form of a thin film, thus providing remarkable advantages in optoelectronic devices. Although bromide based ILs react with water to form acids chemically attacking the electrodes, we demonstrated that it is possible to remove the absorbed water by a vacuum treatment before any voltage is applied, thus preventing the degradation of the metals. Furthermore, the polymer matrix of PMMA embedded ILs protects the electrodes for several cycles in ambient conditions after the vacuum curing. Therefore, devices exploiting our electrolytes can be fabricated with standard techniques in ambient conditions without the need of the inert atmosphere of a glove box, as usually necessary for lithium based ILs [53, 54, 260, 261].
Finally, we tested the gating efficiency of ESs on graphene. An example of device we used is shown in Fig. B.7a. We fabricated a gFET on top of the standard Si/SiO_2 substrate. We also fabricated a 50x50 μm^2 metal pad (G in Fig. B.7a), which will be used as electrode for the ionic liquid. As demonstrated above, the ESs interact with the metals of the electrodes. Thus, we covered the structure with a uniform film of PMMA to protect the source (S), drain (D) and gate (G) electrodes from the liquid. We opened holes in the film with EBL, in correspondence to the graphene channel (indicated by the white arrow in Fig. B.7a) and on top of the gate electrode G. We mounted the sample on a DIL and drop casted ES1 on the finished device.
To test the gating efficiency of ES1, we fixed the voltage between S and D to $V_{SD} = 1$ mV and applied a voltage (V_{TG}) between G and S. We varied V_{TG} between values well within the electrochemical window of ES1, not to damage the system. We computed the resistance following the methods described in Sec. 3.3.2 (2W measurements). As shown in Fig. B.7b, the resistance changes as a function of the applied potential, as expected. This demonstrates the applicability of the chosen ILs as gates for graphene.

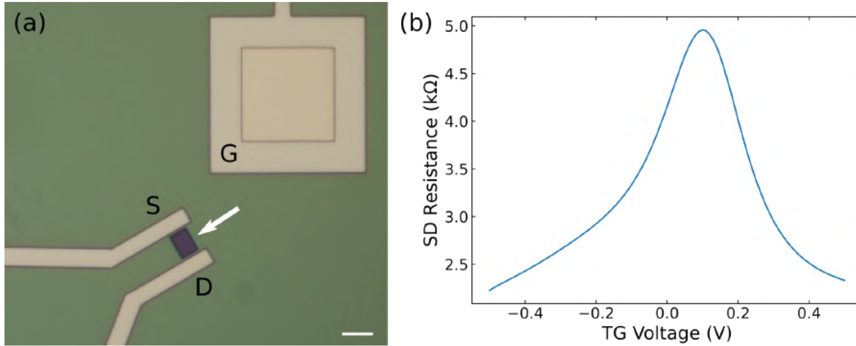

Figure B.7 – (a) Optical image of the gFET partially covered with PMMA (green shading). Source, drain, and gate electrodes are indicated by the letter S, D, and G respectively. Holes were opened with EBL in the PMMA film, in correspondence of the graphene channel (white arrow) and at the center of G. The scalebar is 10 μm. (b) Resistance of the graphene channel as a function of the voltage applied between G and S, for $V_{SD} = 1$ mV.

B.2 Experimental methods

Double Step Chronocoulometry (DSC) Chronocoulometry is a method to compute the charge accumulated in the EDLs [237]. A voltage V_{pp} is applied between two electrodes in contact with the liquid (see inset of Fig. B.1b) at a time $t = t_0$ and is turned off at $t = t_0 + t_{ch}$. The resulting current is measured (Fig. B.8a), then numerically integrated to obtain the amount of charge moved as a function of time (Fig. B.8b). As long as the charge is accumulating in the EDLs, the curve follows the exponential behaviour typical of the charge phase of a parallel plate capacitor. When the EDLs are charged, a residual current establish in the liquid. Such current follows a diffusive regime, and therefore is $\propto \sqrt{t}$. Then, by plotting the accumulated charge as a function of the square root of time (Fig. B.8c), we isolated the time t_D at which the curve enters the linear behaviour by fitting the curve with a line. The accumulated charge Q_{EDL} is then extracted as the difference between the charge measured at $t = t_D$ and the charge measured at $t = t_0$ (inset of Fig. B.8c). A similar procedure can be applied to the discharging phase.

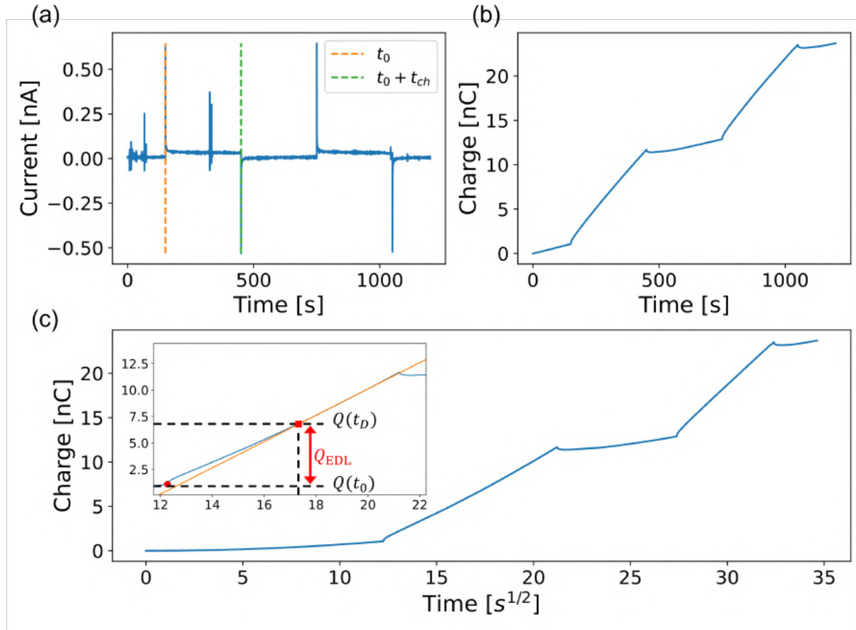

Figure B.8 – Steps of the chronocoulometry measurements. (a) Current over time measured for $V_{pp} = 300$ mV. The voltage is applied at $t = t_0$ (orange dashed line) and is turned off at $t = t_0 + t_{ch}$ (green dashed line). (b) Charge moved during the measurement as a function of time. (c) Charge moved during the measurement as a function of the square root of time. In the inset, the method for extracting the charge accumulated during the first charging is shown. The linear part of the curve is fitted (orange solid line) and t_D is determined as the time at which the curve enters the linear behaviour. The accumulated charge Q_{EDL} is then extracted as the difference between the charge $Q(t_D)$ at time t_D (red square in the picture) and the charge $Q(t_0)$ at time t_0 (red dot in the picture).

Cyclic Voltammetry (CV) We employed cyclic Voltammetry [238, 263] to determine the electrochemical windows of the employed ESs. A voltage V_G, (gate voltage in Fig. B.2) is applied between in the same geometry used for DSC (see inset in Fig. B.1b). V_G is varied cyclically in the selected interval. In our case, the intervals are $[-3, +3]$ for measurements in air and $[-6, +6]$ for measurements in vacuum. The current flowing between the electrodes is recorded as a function of the applied V_G. When inside the electrochemical window, the conductivity

of the system is low, as the charge can only rearrange and diffuse in the liquid. At the onset of the electrochemical reactions, the ionic current increases, as charge can be exchanged with the electrodes, and a different conductivity is observed in the system. Three regions can be distinguished in the curves in Fig. B.2: a high conductivity region for voltages lower then the electrochemical windows, a low conductivity region when V_G is in the electrochemical window, and another high conductivity region for voltages higher than the window limit. We fitted the three different regimes (before, in, and after the electrochemical window) with lines. The line fitted in the central, low-conductivity region crosses the other two in two distinct points. We identify the upper (lower) limit of the electrochemical window as the voltage at which lies the upper (lower) crossing point.

Bibliography

(1) Giuliani, G.; Vignale, G., *Quantum theory of the electron liquid*; Cambridge university press: 2005.

(2) Ashcroft, N. W.; Mermin, N. D., *Solid state physics*; Saunders College Publishing: 1976.

(3) Grosso, G.; Pastori Parravicini, G., *Solid state physics*; Academic press: 2013.

(4) Qi, X.-L.; Zhang, S.-C. *Reviews of Modern Physics* **2011**, *83*, 1057.

(5) Castro Neto, A. H.; Guinea, F.; Peres, N. M. R.; Novoselov, K. S.; Geim, A. K. *Rev. Mod. Phys.* **2009**, *81*, 109–162.

(6) Katsnelson, M. I. *Materials Today* **2007**, *10*, 20–27.

(7) Zhang, Y.; Tan, Y.-W.; Stormer, H. L.; Kim, P. *nature* **2005**, *438*, 201–204.

(8) Bolotin, K. I.; Ghahari, F.; Shulman, M. D.; Stormer, H. L.; Kim, P. *Nature* **2009**, *462*, 196–199.

(9) Katsnelson, M.; Novoselov, K.; Geim, A. *Nature physics* **2006**, *2*, 620–625.

(10) Shytov, A. V.; Rudner, M. S.; Levitov, L. S. *Phys. Rev. Lett.* **2008**, *101*, 156804.

(11) Pereira, J. M.; Peeters, F.; Chaves, A.; Farias, G. *Semiconductor science and technology* **2010**, *25*, 033002.

(12) Mayorov, A. S.; Gorbachev, R. V.; Morozov, S. V.; Britnell, L.; Jalil, R.; Ponomarenko, L. A.; Blake, P.; Novoselov, K. S.; Watanabe, K.; Taniguchi, T., et al. *Nano letters* **2011**, *11*, 2396–2399.

(13) Banszerus, L.; Schmitz, M.; Engels, S.; Goldsche, M.; Watanabe, K.; Taniguchi, T.; Beschoten, B.; Stampfer, C. *Nano letters* **2016**, *16*, 1387–1391.

(14) Areshkin, D. A.; Gunlycke, D.; White, C. T. *Nano letters* **2007**, *7*, 204–210.

(15) Gehring, P.; Sadeghi, H.; Sangtarash, S.; Lau, C. S.; Liu, J.; Ardavan, A.; Warner, J. H.; Lambert, C. J.; Briggs, G. A. D.; Mol, J. A. *Nano letters* **2016**, *16*, 4210–4216.

(16) Koppens, F. H.; Chang, D. E.; Garcia de Abajo, F. J. *Nano letters* **2011**, *11*, 3370–3377.

(17) Gonçalves, P. A. D.; Peres, N. M., *An introduction to graphene plasmonics*; World Scientific: 2016.

(18) Frisk Kockum, A.; Miranowicz, A.; De Liberato, S.; Savasta, S.; Nori, F. *Nature Reviews Physics* **2019**, *1*, 19–40.

(19) Walther, H.; Varcoe, B. T.; Englert, B.-G.; Becker, T. *Reports on Progress in Physics* **2006**, *69*, 1325.

(20) Schubert, E. F., *Light-emitting diodes*; Cambridge university press: 2006.

(21) Weber, E. R.; Willardson, R. K.; Liu, H.; Capasso, F., *Intersubband transitions in quantum wells: physics and device applications*; Academic press: 1999.

(22) Faist, J., *Quantum Cascade Lasers*; Oxford University Press: 2013.

(23) Capasso, F.; Gmachl, C.; Paiella, R.; Tredicucci, A.; Hutchinson, A. L.; Sivco, D. L.; Baillargeon, J. N.; Cho, A. Y.; Liu, H. *IEEE Journal of selected topics in quantum electronics* **2000**, *6*, 931–947.

(24) Levine, B. *Journal of applied physics* **1993**, *74*, R1–R81.

(25) Liu, L.; Qing, M.; Wang, Y.; Chen, S. *Journal of Materials Science & Technology* **2015**, *31*, 599–606.

(26) Jiang, J.; Xu, T.; Lu, J.; Sun, L.; Ni, Z. *Research* **2019**, *2019*.

(27) Lee, G.; Yang, G.; Cho, A.; Han, J.; Kim, J. *Phys. Chem. Chem. Phys.* **2016**, *18*, 14198–14204.

(28) Sunnardianto, G. K.; Bokas, G.; Hussein, A.; Walters, C.; Moultos, O. A.; Dey, P. *International Journal of Hydrogen Energy* **2021**, *46*, 5485–5494.

(29) Bhattacharya, A.; Bhattacharya, S.; Majumder, C.; Das, G. P. *The Journal of Physical Chemistry C* **2010**, *114*, 10297–10301.

(30) Akilan, R.; Malarkodi, M.; Vijayakumar, S.; Gopalakrishnan, S.; Shankar, R. *Applied Surface Science* **2019**, *463*, 596–609.

(31) Han, Q.; Gao, T.; Zhang, R.; Chen, Y.; Liu, G.; Zhang, Y.; Liu, Z.; Wu, X.; Yu, D. *Scientific Reports* **2013**, DOI: `10.1038/srep03533`.

(32) Luo, W.; Cai, W.; Wu, W.; Xiang, Y.; Ren, M.; Zhang, X.; Xu, J. *2D Materials* **2016**, *3*, 045001.

(33) Li, Y.; Dietrich, S.; Forsythe, C.; Taniguchi, T.; Watanabe, K.; Moon, P.; Dean, C. R. *Nature Nanotechnology* **2021**, *16*, 525–530.

(34) Huber, R.; Liu, M.-H.; Chen, S.-C.; Drienovsky, M.; Sandner, A.; Watanabe, K.; Taniguchi, T.; Richter, K.; Weiss, D.; Eroms, J. *Nano letters* **2020**, *20*, 8046–8052.

(35) Huber, R.; Steffen, M.-N.; Drienovsky, M.; Sandner, A.; Watanabe, K.; Taniguchi, T.; Pfannkuche, D.; Weiss, D.; Eroms, J. *Nature Communications* **2022**, *13*, 2856.

(36) Epstein, I.; Alcaraz, D.; Huang, Z.; Pusapati, V.-V.; Hugonin, J.-P.; Kumar, A.; Deputy, X. M.; Khodkov, T.; Rappoport, T. G.; Hong, J.-Y., et al. *Science* **2020**, *368*, 1219–1223.

(37) Todorov, Y.; Sirtori, C. *Phys. Rev. X* **2014**, *4*, 041031.

(38) Liu, Y.-l.; Wang, C.; Zhang, J.; Liu, Y.-x. *Chinese Physics B* **2018**, *27*, 024204.

(39) Wang, D. *Journal of Physics B: Atomic, Molecular and Optical Physics* **2021**, *54*, 133001.

(40) Wallace, P. R. *Phys. Rev.* **1947**, *71*, 622–634.

(41) Katsnelson, M. I., *Graphene: Carbon in Two Dimensions*; Cambridge University Press: 2012.

(42) Novoselov, K. S.; Geim, A. K.; Morozov, S. V.; Jiang, D.-e.; Zhang, Y.; Dubonos, S. V.; Grigorieva, I. V.; Firsov, A. A. *science* **2004**, *306*, 666–669.

(43) Geim, A.; Novoselov, K. *Nature Materials* **2007**, 181–191.

(44) Mackin, C.; Hess, L. H.; Hsu, A.; Song, Y.; Kong, J.; Garrido, J. A.; Palacios, T. *IEEE Transactions on Electron Devices* **2014**, *61*, 3971–3977.

(45) Wang, H.; Hsu, A.; Kong, J.; Antoniadis, D. A.; Palacios, T. *IEEE Transactions on Electron Devices* **2011**, *58*, 1523–1533.

(46) Lu, N.; Wang, L.; Li, L.; Liu, M. *Chinese Physics B* **2017**, *26*, 036804.

(47) Lemme, M. C.; Echtermeyer, T. J.; Baus, M.; Kurz, H. *IEEE Electron Device Letters* **2007**, *28*, 282–284.

(48) Zhang, Y.; Tang, T.-T.; Girit, C.; Hao, Z.; Martin, M. C.; Zettl, A.; Crommie, M. F.; Shen, R.; Wang, F. *Nature* **2009**, *459*, 820–823.

(49) Wang, H.; Taychatanapat, T.; Hsu, A.; Watanabe, K.; Taniguchi, T.; Jarillo-Herrero, P.; Palacios, T. *IEEE Electron Device Letters* **2011**, *32*, 1209–1211.

(50) Kim, S.; Nah, J.; Jo, I.; Shahrjerdi, D.; Colombo, L.; Yao, Z.; Tutuc, E.; Banerjee, S. K. *Applied Physics Letters* **2009**, *94*, 062107.

(51) Sunku, S. S.; Halbertal, D.; Engelke, R.; Yoo, H.; Finney, N. R.; Curreli, N.; Ni, G.; Tan, C.; McLeod, A. S.; Lo, C. F. B., et al. *Nano letters* **2021**, *21*, 1688–1693.

(52) Fujimoto, T.; Awaga, K. *Phys. Chem. Chem. Phys.* **2013**, *15*, 8983–9006.

(53) Daghero, D.; Paolucci, F.; Sola, A.; Tortello, M.; Ummarino, G. A.; Agosto, M.; Gonnelli, R. S.; Nair, J. R.; Gerbaldi, C. *Physical Review Letters* **2012**, *108*, 066807.

(54) Gonnelli, R. S.; Piatti, E.; Sola, A.; Tortello, M.; Dolcini, F.; Galasso, S.; Nair, J. R.; Gerbaldi, C.; Cappelluti, E.; Bruna, M.; Ferrari, A. C. *2D Materials* **2017**, *4*, 035006.

(55) Zhang, H.; Berthod, C.; Berger, H.; Giamarchi, T.; Morpurgo, A. F. *Nano Letters* **2019**, *19*, 8836–8845.

(56) Ferrari, A. C.; Meyer, J. C.; Scardaci, V.; Casiraghi, C.; Lazzeri, M.; Mauri, F.; Piscanec, S.; Jiang, D.; Novoselov, K. S.; Roth, S.; Geim, A. K. *Phys. Rev. Lett.* **2006**, *97*.

(57) Ferrari, A. C. *Solid State Communications* **2007**, *143*, Exploring graphene, 47–57.

(58) Nanda, S. S.; Kim, M. J.; Yeom, K. S.; An, S. S. A.; Ju, H.; Yi, D. K. *TrAC Trends in Analytical Chemistry* **2016**, *80*, 125–131.

(59) Beams, R.; Cançado, L. G.; Novotny, L. *Journal of Physics: Condensed Matter* **2015**, *27*, 083002.

(60) Lee, J. E.; Ahn, G.; Shim, J.; Lee, Y. S.; Ryu, S. *Nat. Comm.* **2012**, *8*, 7432–7441.

(61) Bruna, M.; Ott, A. K.; Ijäs, M.; Yoon, D.; Sassi, U.; Ferrari, A. C. *ACS Nano* **2014**, *8*, 7432–7441.

(62) Milošević, I.; Kepčija, N.; Dobardžić, E.; Damnjanović, M.; Mohr, M.; Maultzsch, J.; Thomsen, C. *Materials Science and Engineering: B* **2011**, *176*, 510–511.

(63) Neumann, C.; Reichardt, S.; Venezuela, P.; Drögeler, M.; Banszerus, L.; Schmitz, M.; Watanabe, K.; Taniguchi, T.; Mauri, F.; Beschoten, B.; Rotkin, S. V.; Stampfer, C. *Nature Communication* **2015**, *6*.

(64) Huang, M.; Yan, H.; Heinz, T. F.; Hone, J. *Nano Letters* **2010**, *10*, 4074–4079.

(65) Tuinstra, F.; Koenig, J. L. *The Journal of chemical physics* **1970**, *53*, 1126–1130.

(66) Avouris, P.; Heinz, T. F.; Low, T., *2D Materials: Properties and Devices*; Cambridge University Press: 2017.

(67) Eckmann, A.; Felten, A.; Verzhbitskiy, I.; Davey, R.; Casiraghi, C. *Phys. Rev. B* **2013**, *88*, 035426.

(68) Eckmann, A.; Felten, A.; Mishchenko, A.; Britnell, L.; Krupke, R.; Novoselov, K. S.; Casiraghi, C. *Nano Letters* **2012**, *12*, PMID: 22764888, 3925–3930.

(69) Maier, S. A. et al., *Plasmonics: fundamentals and applications*; Springer: 2007; Vol. 1.

(70) Barnes, W.; Dereux, A.; Ebbesen, T. *Nature* **2003**, 824–830.

(71) Jablan, M.; Buljan, H.; Soljačić, M. *Physical review B* **2009**, *80*, 245435.

(72) Xiao, S.; Zhu, X.; Li, B.-H.; Mortensen, N. A. *Frontiers of Physics* **2016**, *11*, 1–13.

(73) Woessner, A.; Lundeberg, M. B.; Gao, Y.; Principi, A.; Alonso-González, P.; Carrega, M.; Watanabe, K.; Taniguchi, T.; Vignale, G.; Polini, M., et al. *Nature materials* **2015**, *14*, 421–425.

(74) Lundeberg, M. B.; Gao, Y.; Asgari, R.; Tan, C.; Van Duppen, B.; Autore, M.; Alonso-González, P.; Woessner, A.; Watanabe, K.; Taniguchi, T., et al. *Science* **2017**, *357*, 187–191.

(75) Dean, C. R.; Young, A. F.; Meric, I.; Lee, C.; Wang, L.; Sorgenfrei, S.; Watanabe, K.; Taniguchi, T.; Kim, P.; Shepard, K. L., et al. *Nature nanotechnology* **2010**, *5*, 722–726.

(76) Ni, G.; McLeod, d. A.; Sun, Z.; Wang, L.; Xiong, L.; Post, K.; Sunku, S.; Jiang, B.-Y.; Hone, J.; Dean, C. R., et al. *Nature* **2018**, *557*, 530–533.

(77) Basov, D. N.; Fogler, M. M.; de Abajo, F. J. G. *Science* **2016**, *354*, aag1992.

(78) Ju, L.; Geng, B.; Horng, J.; Girit, C.; Martin, M.; Hao, Z.; Bechtel, H. A.; Liang, X.; Zettl, A.; Shen, Y. R., et al. *Nature nanotechnology* **2011**, *6*, 630–634.

(79) Yan, H.; Low, T.; Zhu, W.; Wu, Y.; Freitag, M.; Li, X.; Guinea, F.; Avouris, P.; Xia, F. *Nature Photonics* **2013**, *7*, 394–399.

(80) Strait, J. H.; Nene, P.; Chan, W.-M.; Manolatou, C.; Tiwari, S.; Rana, F.; Kevek, J. W.; McEuen, P. L. *Physical Review B* **2013**, *87*, 241410.

(81) Peres, N. M. R.; Bludov, Y. V.; Ferreira, A.; Vasilevskiy, M. I. *Journal of Physics: Condensed Matter* **2013**, *25*, 125303.

(82) Fei, Z.; Rodin, A.; Andreev, G. O.; Bao, W.; McLeod, A.; Wagner, M.; Zhang, L.; Zhao, Z.; Thiemens, M.; Dominguez, G., et al. *Nature* **2012**, *487*, 82–85.

(83) Chen, J.; Badioli, M.; Alonso-González, P.; Thongrattanasiri, S.; Huth, F.; Osmond, J.; Spasenović, M.; Centeno, A.; Pesquera, A.; Godignon, P., et al. *Nature* **2012**, *487*, 77–81.

(84) Ihn, T., *Semiconductor Nanostructures: Quantum states and electronic transport*; OUP Oxford: 2009.

(85) Dingle, R.; Wiegmann, W.; Henry, C. H. *Phys. Rev. Lett.* **1974**, *33*, 827–830.

(86) Yariv, A.; Yeh, P., *Photonics: optical electronics in modern communications*; Oxford university press: 2007.

(87) Kurman, Y.; Rivera, N.; Christensen, T.; Tsesses, S.; Orenstein, M.; Soljačić, M.; Joannopoulos, J. D.; Kaminer, I. *Nature Photonics* **2018**, *12*, 423–429.

(88) Raimond, J. M.; Brune, M.; Haroche, S. *Rev. Mod. Phys.* **2001**, *73*, 565–582.

(89) Rempe, G.; Walther, H.; Klein, N. *Physical review letters* **1987**, *58*, 353.

(90) Dini, D.; Köhler, R.; Tredicucci, A.; Biasiol, G.; Sorba, L. *Physical review letters* **2003**, *90*, 116401.

(91) Hopfield, J. J. *Phys. Rev.* **1958**, *112*, 1555–1567.

(92) Ciuti, C.; Bastard, G.; Carusotto, I. *Physical Review B* **2005**, *72*, 115303.

(93) Fox, M., *Quantum optics: an introduction*; Oxford university press: 2006; Vol. 15.

(94) Todorov, Y.; Sirtori, C. *Phys. Rev. B* **2012**, *85*, 045304.

(95) Ando, T.; Fowler, A. B.; Stern, F. *Reviews of Modern Physics* **1982**, *54*, 437.

(96) Jeannin, M.; Mariotti Nesurini, G.; Suffit, S.; Gacemi, D.; Vasanelli, A.; Li, L.; Davies, A. G.; Linfield, E.; Sirtori, C.; Todorov, Y. *ACS photonics* **2019**, *6*, 1207–1215.

(97) Pisani, F.; Zanotto, S.; Tredicucci, A. *JOSA B* **2020**, *37*, 19–23.

(98) Keller, J.; Scalari, G.; Cibella, S.; Maissen, C.; Appugliese, F.; Giovine, E.; Leoni, R.; Beck, M.; Faist, J. *Nano letters* **2017**, *17*, 7410–7415.

(99) Banhart, F.; Kotakoski, J.; Krasheninnikov, A. *ACS Nano* **2011**, *5*, 26–41.

(100) Yang, G.; Li, L.; Lee, W. B.; Ng, M. C. *Science and Technology of Advanced Materials* **2018**, *19*, 613–648.

(101) Boukhvalov, D. W.; Katsnelson, M. I. *Nano Letters* **2008**, *8*, 4373–4379.

(102) Hernández, S. C.; Bezares, F. J.; Robinson, J. T.; Caldwell, J. D.; Walton, S. G. *Carbon* **2013**, *60*, 84–93.

(103) Ye, X.-L.; Cai, J.; Yang, X.-D.; Tang, X.-Y.; Zhou, Z.-Y.; Tan, Y.-Z.; Xie, S.-Y.; Zheng, L.-S. *J. Mater. Chem. A* **2017**, *5*, 24257–24262.

(104) Cantele, G.; Lee, Y.-S.; Ninno, D.; Marzari, N. *Nano letters* **2009**, *9*, 3425–3429.

(105) Peng, X.; Ahuja, R. *Nano letters* **2008**, *8*, 4464–4468.

(106) Basta, L.; Bianco, F.; Moscardini, A.; Fabbri, F.; Bellucci, L.; Tozzini, V.; Heun, S.; Veronesi, S. *Journal of Materials Chemistry C* **2023**.

(107) Liang, Z.; Fan, X.; Zheng, W.; Singh, D. J. *ACS Applied Materials & Interfaces* **2017**, *9*, PMID: 28474877, 17076–17084.

(108) Malekpour, H.; Ramnani, P.; Srinivasan, S.; Balasubramanian, G.; Nika, D. L.; Mulchandani, A.; Lake, R. K.; Balandin, A. A. *Nanoscale* **2016**, *8*, 14608–14616.

(109) Anno, Y.; Imakita, Y.; Takei, K.; Akita, S.; Arie, T. *2D Materials* **2017**, *4*, 025019.

(110) Zeng, M.; Feng, Y.; Liang, G. *Nano letters* **2011**, *11*, 1369–1373.

(111) Tapasztó, L.; Dobrik, G.; Nemes-Incze, P.; Vertesy, G.; Lambin, P.; Biró, L. P. *Phys. Rev. B* **2008**, *78*, 233407.

(112) Lherbier, A.; Dubois, S. M.-M.; Declerck, X.; Niquet, Y.-M.; Roche, S.; Charlier, J.-C. *Physical Review B* **2012**, *86*, 075402.

(113) Childres, I.; Jauregui, L. A.; Foxe, M.; Tian, J.; Jalilian, R.; Jovanovic, I.; Chen, Y. P. *Applied Physics Letters* **2010**, *97*.

(114) Chen, J.-H.; Cullen, W. G.; Jang, C.; Fuhrer, M.; Williams, E. D. *Physical review letters* **2009**, *102*, 236805.

(115) Liu, G.; Teweldebrhan, D.; Balandin, A. A. *IEEE Transactions on Nanotechnology* **2011**, *10*, 865–870.

(116) Moktadir, Z.; Hang, S.; Mizuta, H. *Carbon* **2015**, *93*, 325–334.

(117) Tachikawa, H.; Kawabata, H. *The Journal of Physical Chemistry C* **2009**, *113*, 7603–7609.

(118) Garcia-Pomar, J. L.; Nikitin, A. Y.; Martin-Moreno, L. *ACS nano* **2013**, *7*, 4988–4994.

(119) Botello-Méndez, A. R.; Lherbier, A.; Charlier, J.-C. *Solid state communications* **2013**, *175*, 90–100.

(120) Lee, G.; Kim, J.; Kim, K.; Han, J. W. *Journal of Vacuum Science & Technology A: Vacuum, Surfaces, and Films* **2015**, *33*, 060602.

(121) Krasheninnikov, A.; Banhart, F. *Nature materials* **2007**, *6*, 723–733.

(122) Krasheninnikov, A.; Nordlund, K. *Journal of applied physics* **2010**, *107*, 3.

(123) Compagnini, G.; Giannazzo, F.; Sonde, S.; Raineri, V.; Rimini, E. *Carbon* **2009**, *47*, 3201–3207.

(124) Banhart, F. *Reports on progress in physics* **1999**, *62*, 1181.

(125) Ugeda, M. M.; Brihuega, I.; Guinea, F.; Gómez-Rodríguez, J. M. *Physical Review Letters* **2010**, *104*, 096804.

(126) Meyer, J. C.; Eder, F.; Kurasch, S.; Skakalova, V.; Kotakoski, J.; Park, H. J.; Roth, S.; Chuvilin, A.; Eyhusen, S.; Benner, G.; Krasheninnikov, A. V.; Kaiser, U. *Phys. Rev. Lett.* **2012**, *108*, 196102.

(127) Osváth, Z.; Vértesy, G.; Tapasztó, L.; Wéber, F.; Horváth, Z.; Gyulai, J.; Biró, L. *Physical Review B* **2005**, *72*, 045429.

(128) Kotakoski, J.; Krasheninnikov, A. V., *Computational Nanoscience*; Bichoutskaia, E., Ed.; The Royal Society of Chemistry: 2011, pp 334–376.

(129) Wu, J.-B.; Lin, M.-L.; Cong, X.; Liu, H.-N.; Tan, P.-H. *Chem. Soc. Rev.* **2018**, *47*, 1822–1873.

(130) Wu, X., *Influence of Particle Beam Irradiation on the Structure and Properties of Graphene*; Springer, Ed.; Springer Theses; Springer Singapore.

(131) Guseinov, N.; Ilyin, A. *Journal of Materials Science and Engineering A 4* **2014**, *1*, 39–44.

(132) Guseinov, N. R.; Ilyin, A. M. *New Approaches in Engineering Research Vol. 10* **2021**, 32–40.

(133) Stevens-Kalceff, M. A. *Phys. Rev. Lett.* **2000**, *84*, 3137–3140.

(134) Jones, J.; Mahajan, K.; Williams, W.; Ecton, P.; Mo, Y.; Perez, J. *Carbon* **2010**, *48*, 2335–2340.

(135) Basta, L.; Moscardini, A.; Veronesi, S.; Bianco, F. *Surfaces and Interfaces* **2022**, *28*, 101694.

(136) Liu, Y.; Song, J.; Li, Y.; Liu, Y.; Sun, Q.-f. *Phys. Rev. B* **2013**, *87*, 195445.

(137) Lü, X.; Jiang, L.; Zheng, Y. *Physics Letters A* **2013**, *377*, 2687–2691.

(138) Calogeracos, A.; Dombey, N. *Contemporary physics* **1999**, *40*, 313–321.

(139) Yan, B.; Han, Q.; Jia, Z.; Niu, J.; Cai, T.; Yu, D.; Wu, X. *Physical Review B* **2016**, *93*, 041407.

(140) Vandecasteele, N.; Barreiro, A.; Lazzeri, M.; Bachtold, A.; Mauri, F. *Physical Review B* **2010**, *82*, 045416.

(141) Popovici, C.; Oliveira, O.; de Paula, W.; Frederico, T. *Physical Review B* **2012**, *85*, 235424.

(142) Gorbachev, R. V.; Mayorov, A. S.; Savchenko, A. K.; Horsell, D. W.; Guinea, F. *Nano Letters* **2008**, *8*, 1995–1999.

(143) Cheianov, V. V.; Fal'ko, V. I. *Phys. Rev. B* **2006**, *74*, 041403.

(144) Zhang, L. M.; Fogler, M. *Physical review letters* **2008**, *100*, 116804.

(145) Stander, N.; Huard, B.; Goldhaber-Gordon, D. *Physical review letters* **2009**, *102*, 026807.

(146) Young, A. F.; Kim, P. *Nature Physics* **2009**, *5*, 222–226.

(147) Herbschleb, E. D.; Puddy, R. K.; Marconcini, P.; Griffiths, J. P.; Jones, G. A. C.; Macucci, M.; Smith, C. G.; Connolly, M. R. *Phys. Rev. B* **2015**, *92*, 125414.

(148) Allen, M. T.; Shtanko, O.; Fulga, I. C.; Wang, J. I.-J.; Nurgaliev, D.; Watanabe, K.; Taniguchi, T.; Akhmerov, A. R.; Jarillo-Herrero, P.; Levitov, L. S.; Yacoby, A. *Nano Letters* **2017**, *17*, 7380–7386.

(149) Rossi, E.; Bardarson, J.; Brouwer, P.; Sarma, S. D. *Physical Review B* **2010**, *81*, 121408.

(150) Wang, L.-G.; Zhu, S.-Y. *Phys. Rev. B* **2010**, *81*, 205444.

(151) Dakhlaoui, H.; Belhadj, W.; Wong, B. M. *Results in Physics* **2021**, *26*, 104403.

(152) Marconcini, P.; Macucci, M. *Journal of Applied Physics* **2019**, *125*, DOI: 10.1063/1.5092512.

(153) Novoselov, K.; Neto, A. C. *Physica Scripta* **2012**, *2012*, 014006.

(154) Gao, E.; Lin, S.-Z.; Qin, Z.; Buehler, M. J.; Feng, X.-Q.; Xu, Z. *Journal of the Mechanics and Physics of Solids* **2018**, *115*, 248–262.

(155) Bonaccorso, F.; Lombardo, A.; Hasan, T.; Sun, Z.; Colombo, L.; Ferrari, A. C. *Materials today* **2012**, *15*, 564–589.

(156) Novoselov, K. *Reviews of modern physics* **2011**, *83*, 837.

(157) Novoselov, K. S.; Jiang, D.; Schedin, F.; Booth, T.; Khotkevich, V.; Morozov, S.; Geim, A. K. *Proceedings of the National Academy of Sciences* **2005**, *102*, 10451–10453.

(158) Blake, P.; Hill, E.; Castro Neto, A.; Novoselov, K.; Jiang, D.; Yang, R.; Booth, T.; Geim, A. *Applied physics letters* **2007**, *91*, 063124.

(159) Roddaro, S.; Pingue, P.; Piazza, V.; Pellegrini, V.; Beltram, F. *Nano letters* **2007**, *7*, 2707–2710.

(160) Geim, A. K. *Science* **2009**, *324*, 1530–1534.

(161) Zhang, Y.; Zhang, L.; Zhou, C. *Accounts of chemical research* **2013**, *46*, 2329–2339.

(162) Lee, J.-Y.; Lee, J.-H.; Kim, M. J.; Dash, J. K.; Lee, C.-H.; Joshi, R.; Lee, S.; Hone, J.; Soon, A.; Lee, G.-H. *Carbon* **2017**, *115*, 147–153.

(163) Miseikis, V.; Bianco, F.; David, J.; Gemmi, M.; Pellegrini, V.; Romagnoli, M.; Coletti, C. *2D Materials* **2017**, *4*, 021004.

(164) Bischoff, D.; Simonet, P.; Varlet, A.; Overweg, H. C.; Eich, M.; Ihn, T.; Ensslin, K. *physica status solidi (RRL)–Rapid Research Letters* **2016**, *10*, 68–74.

(165) He, T.; Wang, Z.; Zhong, F.; Fang, H.; Wang, P.; Hu, W. *Advanced Materials Technologies* **2019**, *4*, 1900064.

(166) Zhang, H.; Huang, J.; Wang, Y.; Liu, R.; Huai, X.; Jiang, J.; Anfuso, C. *Optics Communications* **2018**, *406*, 3–17.

(167) Rousso, I.; Deshpande, A. *Viruses* **2022**, *14*, 648.

(168) Dutta, A. *Spectroscopic methods for nanomaterials characterization* **2017**, 73–93.

(169) Pavia, D. L.; Lampman, G. M.; Kriz, G. S.; Vyvyan, J. A., *Introduction to spectroscopy*; Cengage learning: 2014.

(170) Fahrenfort, J. *Spectrochimica Acta* **1961**, *17*, 698–709.

(171) Mendoza-Galván, A.; Méndez-Lara, J.; Mauricio-Sánchez, R.; Järrendahl, K.; Arwin, H. *Optics Letters* **2021**, *46*, 872–875.

(172) Harrick, N. J.; du Pré, F. K. *Appl. Opt.* **1966**, *5*, 1739–1743.

(173) Nong, J.; Tang, L.; Lan, G.; Luo, P.; Guo, C.; Yi, J.; Wei, W. *Nanophotonics* **2020**, *9*, 645–655.

(174) Long, Y.; Twiefel, J.; Wallaschek, J. *Journal of materials processing technology* **2017**, *245*, 241–258.

(175) Manceau, J.-M.; Zanotto, S.; Sagnes, I.; Beaudoin, G.; Colombelli, R. *Applied Physics Letters* **2013**, *103*, 091110.

(176) Lorimor, O.; Spitzer, W. *Journal of Applied Physics* **1965**, *36*, 1841–1844.

(177) Bouarissa, N.; Aourag, H. *Infrared physics & technology* **1999**, *40*, 343–349.

(178) Markelz, A.; Asmar, N.; Gwinn, E.; Brar, B. *Applied physics letters* **1998**, *72*, 2439–2441.

(179) Depine, R. A., *Graphene optics: electromagnetic solution of canonical problems*; Morgan & Claypool Publishers: 2017.

(180) Nayyeri, V.; Soleimani, M.; Ramahi, O. M. *IEEE transactions on antennas and propagation* **2013**, *61*, 4176–4182.

(181) Caldwell, J. D.; Kretinin, A. V.; Chen, Y.; Giannini, V.; Fogler, M. M.; Francescato, Y.; Ellis, C. T.; Tischler, J. G.; Woods, C. R.; Giles, A. J., et al. *Nature communications* **2014**, *5*, 5221.

(182) Ordal, M. A.; Bell, R. J.; Alexander, R. W.; Long, L. L.; Querry, M. R. *Appl. Opt.* **1985**, *24*, 4493–4499.

(183) Bellucci, S.; Vernyhor, O.; Bendziak, A.; Yaremchuk, I.; Fitio, V. M.; Bobitski, Y. *Materials* **2020**, *13*, DOI: `10.3390/ma13081882`.

(184) Tuttle, G.; Kroemer, H.; English, J. H. *Journal of applied physics* **1989**, *65*, 5239–5242.

(185) Strickland, W. M.; Hatefipour, M.; Langone, D.; Farzaneh, S.; Shabani, J. *Applied Physics Letters* **2022**, *121*, 092104.

(186) Haynes, W. M., *CRC handbook of chemistry and physics*, 103rd ed.; CRC press: 2022.

(187) Gulyamov, G.; Jamoldinovich, B. P., et al. *Journal of Modern Physics* **2016**, *7*, 1644–1650.

(188) Chang, T. *Journal of vacuum science and technology* **1975**, *12*, 1271–1275.

(189) Cummings, K.; Kiersh, M. *Journal of Vacuum Science & Technology B: Microelectronics Processing and Phenomena* **1989**, *7*, 1536–1539.

(190) Tseng, A. A.; Chen, K.; Chen, C. D.; Ma, K. J. *IEEE Transactions on electronics packaging manufacturing* **2003**, *26*, 141–149.

(191) Jitian, S.; Bratu, I. In *AIP Conference Proceedings*, 2012; Vol. 1425, pp 26–29.

(192) Gunde, M. K. *Physica B: Condensed Matter* **2000**, *292*, 286–295.

(193) Fang, Z.; Ma, K.; Jaw, D.; Cohen, R.; Stringfellow, G. *Journal of Applied Physics* **1990**, *67*, 7034–7039.

(194) Smith, D. G., *Field guide to physical optics*, 2013.

(195) Wendler, L.; Kraft, T.; Hartung, M.; Berger, A.; Wixforth, A.; Sundaram, M.; English, J.; Gossard, A. *Physical Review B* **1997**, *55*, 2303.

(196) Hong, J.; Park, M. K.; Lee, E. J.; Lee, D.; Hwang, D. S.; Ryu, S. *Scientific Reports* **2013**, *3*.

(197) Mohammadi, M.; Davoodi, J., et al. *European Polymer Journal* **2017**, *91*, 121–133.

(198) Grundler, D. *Physical review letters* **2000**, *84*, 6074.

(199) Melchioni, N.; Trupiano, G.; Tofani, G.; Bertini, R.; Mezzetta, A.; Bianco, F.; Guazzelli, L.; Beltram, F.; Pomelli, C. S.; Roddaro, S.; Tredicucci, A.; Paolucci, F. *Applied Physics Letters* **2023**, *122*, DOI: 10.1063/5.0153394.

(200) Melchioni, N.; Bellucci, L.; Tredicucci, A.; Bianco, F. *Surfaces and Interfaces* **2023**, 102662.

(201) Wang, B.; Pantelides, S. T. *Phys. Rev. B* **2011**, *83*, 245403.

(202) Islam, A. E.; Susner, M. A.; Carpena-Núñez, J.; Back, T. C.; Rao, R.; Jiang, J.; Pachter, R.; Tenney, S. A.; Boeckl, J. J.; Maruyama, B. *Carbon* **2020**, *166*, 446–455.

(203) Tsetseris, L.; Pantelides, S. *Carbon* **2009**, *47*, 901–908.

(204) Zan, R.; Ramasse, Q. M.; Bangert, U.; Novoselov, K. S. *Nano Letters* **2012**, *12*, 3936–3940.

(205) Krauss, B.; Lohmann, T.; Chae, D.-H.; Haluska, M.; von Klitzing, K.; Smet, J. H. *Phys. Rev. B* **2009**, *79*, 165428.

(206) Leyssale, J.-M.; Vignoles, G. L. *The Journal of Physical Chemistry C* **2014**, *118*, 8200–8216.

(207) Blanc, N.; Jean, F.; Krasheninnikov, A. V.; Renaud, G.; Coraux, J. *Phys. Rev. Lett.* **2013**, *111*, 085501.

(208) Park, H.; Qi, J.; Xu, Y.; Varga, K.; Weiss, S. M.; Rogers, B. R.; Lüpke, G.; Tolk, N. *Applied Physics Letters* **2009**, *95*, 062102.

(209) Burson, K. M.; Cullen, W. G.; Adam, S.; Dean, C. R.; Watanabe, K.; Taniguchi, T.; Kim, P.; Fuhrer, M. S. *Nano Letters* **2013**, *95*, 062102.

(210) Xia, J.; Liu, X.; Zhou, W.; Wang, F.; Wu, H. *Nanotechnology* **2016**, *27*, 274004.

(211) Jang, I.; Sinnott, S. B.; Danailov, D.; Keblinski, P. *Nano Letters* **2004**, *4*, 109–114.

(212) Asayama, Y.; Yasuda, M.; Tada, K.; Kawata, H.; Hirai, Y. *Journal of Vacuum Science & Technology B, Nanotechnology and Microelectronics: Materials, Processing, Measurement, and Phenomena* **2012**, *30*, 06FJ02.

(213) Kida, S.; Yamamoto, M.; Tada, K.; Kawata, H.; Hirai, Y.; Yasuda, M. *Journal of Vacuum Science & Technology A: Vacuum, Surfaces, and Films* **2015**, *33*, 05E127.

(214) Denis, P. A.; Iribarne, F. *The Journal of Physical Chemistry C* **2013**, *117*, 19048–19055.

(215) Li, Z.; Wang, Y.; Kozbial, A.; Shenoy, G.; Zhou, F.; McGinley, R.; Ireland, P.; Morganstein, B.; Kunkel, A.; Surwade, S. P.; Li, L.; Liu, H. *Nature Materials* **2013**, *12*, 925–931.

(216) Melchioni, N.; Fabbri, F.; Tredicucci, A.; Bianco, F. *Micromachines* **2022**, *13*, 1666.

(217) Tao, L.; Qiu, C.; Yu, F.; Yang, H.; Chen, M.; Wang, G.; Sun, L. *The Journal of Physical Chemistry C* **2013**, *117*, 10079–10085.

(218) Childres, I.; Jauregui, L. A.; Chen, Y. P. *Journal of Applied Physics* **2014**, *116*, 233101.

(219) Cançado, L. G.; Jorio, A.; Ferreira, E. H. M.; Stavale, F.; Achete, C. A.; Capaz, R. B.; Moutinho, M. V. O.; Lombardo, A.; Kulmala, T. S.; Ferrari, A. C. *Nano Letters* **2011**, *11*, 3190–3196.

(220) Yoon, D.; Son, Y.-W.; Cheong, H. *Phys. Rev. Lett.* **2011**, *106*, 155502.

(221) Di Bartolomeo, A.; Santandrea, S.; Giubileo, F.; Romeo, F.; Petrosino, M.; Citro, R.; Barbara, P.; Lupina, G.; Schröder, T.; Rubino, A. *Diamond and Related Materials* **2013**, *38*, 19–23.

(222) Xu, S.; Zhang, Q. In *2010 International Workshop on Junction Technology Extended Abstracts*, 2010, pp 1–3.

(223) Huard, B.; Stander, N.; Sulpizio, J.; Goldhaber-Gordon, D. *Physical Review B* **2008**, *78*, 121402.

(224) Kim, J.-H.; Hwang, J. H.; Suh, J.; Tongay, S.; Kwon, S.; Hwang, C.; Wu, J.; Young Park, J. *Applied Physics Letters* **2013**, *103*, 171604.

(225) Bolotin, K. I.; Sikes, K.; Jiang, Z.; Klima, M.; Fudenberg, G.; Hone, J.; Kim, P.; Stormer, H. L. *Solid state communications* **2008**, *146*, 351–355.

(226) Ki, D.-K.; Jeong, D.; Choi, J.-H.; Lee, H.-J.; Park, K.-S. *Physical Review B* **2008**, *78*, 125409.

(227) Kharitonov, M. Y.; Efetov, K. B. *Physical Review B* **2008**, *78*, 033404.

(228) Sarma, S. D.; Adam, S.; Hwang, E.; Rossi, E. *Reviews of modern physics* **2011**, *83*, 407.

(229) Piatti, E.; Guglielmero, L.; Tofani, G.; Mezzetta, A.; Guazzelli, L.; D'Andrea, F.; Roddaro, S.; Pomelli, C. S. *Journal of Molecular Liquids* **2022**, *364*, 120001.

(230) Palumbo, O.; Cimini, A.; Trequattrini, F.; Brubach, J.-B.; Roy, P.; Paolone, A. *Phys. Chem. Chem. Phys.* **2020**, *22*, 7497–7506.

(231) Moumene, T.; Belarbi, E. H.; Haddad, B.; Villemin, D.; Abbas, O.; Khelifa, B.; Bresson, S. *Journal of Molecular Structure* **2014**, *1065-1066*, 86–92.

(232) Vraneš, M.; Papović, S.; Rackov, S.; Alenezi, K.; Gadžurić, S.; Tot, A.; Pilić, B. *The Journal of Chemical Thermodynamics* **2019**, *139*, 105871.

(233) Ferdeghini, C.; Guazzelli, L.; Pomelli, C. S.; Ciccioli, A.; Brunetti, B.; Mezzetta, A.; Vecchio Ciprioti, S. *Journal of Molecular Liquids* **2021**, *332*, 115662.

(234) Chiappe, C.; Mezzetta, A.; Pomelli, C. S.; Puccini, M.; Seggiani, M. *Organic Process Research & Development* **2016**, *20*, 2080–2084.

(235) Silverstein, R. M.; Webster, F. X.; Kiemle, D. J.; Bryce, D. L., *Spectrometric Identification of Organic Compounds, 8th edition*; Wiley: 2014.

(236) Yamada, T.; Tominari, Y.; Tanaka, S.; Mizuno, M. *The Journal of Physical Chemistry B* **2017**, *121*, 3121–3129.

(237) Inzelt, G. In *Electroanalytical Methods: Guide to Experiments and Applications*, Scholz, F., Bond, A., Compton, R., Fiedler, D., Inzelt, G., Kahlert, H., Komorsky-Lovrić, Š., Lohse, H., Lovrić, M., Marken, F., Neudeck, A., Retter, U., Scholz, F., Stojek, Z., Eds.; Springer Berlin Heidelberg: Berlin, Heidelberg, 2010, pp 147–158.

(238) Hayyan, M.; Mjalli, F. S.; Hashim, M. A.; AlNashef, I. M.; Mei, T. X. *Journal of Industrial and Engineering Chemistry* **2013**, *19*, 106–112.

(239) Zhao, S.; Zhou, Z.; Peng, B.; Zhu, M.; Feng, M.; Yang, Q.; Yan, Y.; Ren, W.; Ye, Z.-G.; Liu, Y.; Liu, M. *Advanced Materials* **2017**, *29*, 1606478.

(240) Girault, H. H., *Analytical and Physical Electrochemistry*, 1st Edition; EPFL Press: 2004.

(241) Shkrob, I. A.; Marin, T. W.; Crowell, R. A.; Wishart, J. F. *The Journal of Physical Chemistry A* **2013**, *117*, 5742–5756.

(242) Clark, R.; von Domaros, M.; McIntosh, A. J. S.; Luzar, A.; Kirchner, B.; Welton, T. *The Journal of Chemical Physics* **2019**, *151*, 164503.

(243) Shi, R.; Wang, Y. *The Journal of Physical Chemistry B* **2013**, *117*, 5102–5112.

(244) Zhao, Q.; Bennington, P.; Nealey, P. F.; Patel, S. N.; Evans, C. M. *Macromolecules* **2021**, *54*, 10520–10528.

(245) Sivey, J. D.; Arey, J. S.; Tentscher, P. R.; Roberts, A. L. *Environmental Science & Technology* **2013**, *47*, 1330–1338.

(246) Walker, P.; Tarn, W. H., *CRC handbook of metal etchants*; CRC press: 1990.

(247) N'Diaye, M.; Pascaretti-Grizon, F.; Massin, P.; Baslé, M. F.; Chappard, D. *Langmuir* **2012**, *28*, 11609–11614.

(248) El-Menyawy, E.; El-Ghamaz, N.; Nawar, H. *Journal of Molecular Structure* **2013**, *1036*, 144–150.

(249) Jitian, S.; Bratu, I. *AIP Conference Proceedings* **2012**, *1425*, 26–29.

(250) Jeon, Y.; Sung, J.; Seo, C.; Lim, H.; Cheong, H.; Kang, M.; Moon, B.; Ouchi, Y.; Kim, D. *The Journal of Physical Chemistry B* **2008**, *112*, 4735–4740.

(251) Lehmann, A.; Schumann, L.; Hübner, K. *Physica Status Solidi B* **1983**, *117*, 689–698.

(252) Mogurampelly, S.; Ganesan, V. *The Journal of Chemical Physics* **2017**, *146*, 074902.

(253) Ganesan, V. *Mol. Syst. Des. Eng.* **2019**, *4*, 280–293.

(254) Vargas-Barbosa, N. M.; Roling, B. *ChemElectroChem* **2020**, *7*, 367–385.

(255) Xiao, W.; Yang, Q.; Zhu, S. *Sci. Rep.* **2020**, *10*, DOI: `10.1038/s41598-020-64689-8`.

(256) Fong, K. D.; Self, J.; McCloskey, B. D.; Persson, K. A. *Macromolecules* **2021**, *54*, 2575–2591.

(257) Ramesh, S.; Liew, C.-W.; Ramesh, K. *Journal of Non-Crystalline Solids* **2011**, *357*, 2132–2138.

(258) Shen, K.-H.; Hall, L. M. *Macromolecules* **2020**, *53*, 10086–10096.

(259) Sharick, S.; Koski, J.; Riggleman, R. A.; Winey, K. I. *Macromolecules* **2016**, *49*, 2245–2256.

(260) Kühne, M.; Paolucci, F.; Popovic, J.; Ostrovsky, P.; Maier, J.; Smet, J. *Nature Nanotechnology* **2017**, *12*, 895–900.

(261) Zielinski, P.; Kühne, M.; Kärcher, D.; Paolucci, F.; Wochner, P.; Fecher, S.; Drnec, J.; Felici, R.; Smet, J. H. *Nano Letters* **2019**, *19*, 3634–3640.

(262) Piatti, E. *Nano Express* **2021**, *2*, 024003.

(263) Elgrishi, N.; Rountree, K. J.; McCarthy, B. D.; Rountree, E. S.; Eisenhart, T. T.; Dempsey, J. L. *Journal of chemical education* **2018**, *95*, 197–206.